Sussex Research Online

Reionization and the cosmic dawn with the square kilometre array

Article (Published Version)

Mellema, Garrelt, Koopmans, Léon V E, Abdalla, Filipe A, Bernardi, Gianni, Ciardi, Benedetta, Daiboo, Soobash, de Bruyn, A G, Datta, Kanan K, Falcke, Heino, Ferrara, Andrea, Iliev, Ilian T, Iocco, Fabio, Jelić, Vibor, Jensen, Hannes, Joseph, Ronniy et al. (2013) Reionization and the cosmic dawn with the square kilometre array. Experimental Astronomy, 36 (1-2). pp. 235-318. ISSN 0922-6435

This version is available from Sussex Research Online: http://sro.sussex.ac.uk/id/eprint/45327/

This document is made available in accordance with publisher policies and may differ from the published version or from the version of record. If you wish to cite this item you are advised to consult the publisher’s version. Please see the URL above for details on accessing the published version.

Copyright and reuse:
Sussex Research Online is a digital repository of the research output of the University.

Copyright and all moral rights to the version of the paper presented here belong to the individual author(s) and/or other copyright owners. To the extent reasonable and practicable, the material made available in SRO has been checked for eligibility before being made available.

Copies of full text items generally can be reproduced, displayed or performed and given to third parties in any format or medium for personal research or study, educational, or not-for-profit purposes without prior permission or charge, provided that the authors, title and full bibliographic details are credited, a hyperlink and/or URL is given for the original metadata page and the content is not changed in any way.

http://sro.sussex.ac.uk

Experimental Astronomy manuscript No.
(will be inserted by the editor)

Reionization and the Cosmic Dawn with the Square Kilometre Array

Garrelt Mellema · Léon V. E. Koopmans · Filipe A. Abdalla · Gianni Bernardi · Benedetta Ciardi · Soobash Daiboo · A. G. de Bruyn · Kanan K. Datta · Heino Falcke · Andrea Ferrara · Ilian T. Iliev · Fabio Iocco · Vibor Jelić · Hannes Jensen · Ronniy Joseph · Panos Labroupoulos · Avery Meiksin · Andrei Mesinger · André R. Offringa · V. N. Pandey · Jonathan R. Pritchard · Mario G. Santos · Dominik J. Schwarz · Benoit Semelin · Harish Vedantham · Sarod Yatawatta · Saleem Zaroubi

Received: 6 February 2013 / Accepted: 26 February 2013

Abstract The Square Kilometre Array (SKA) will have a low frequency component (SKA-low) which has as one of its main science goals the study of the redshifted 21cm line from the earliest phases of star and galaxy formation in the Universe. This 21cm signal provides a new and unique window both on the time of the formation of the first stars and accreting black holes and the subsequent period of substantial ionization of the intergalactic medium. The signal will teach us fundamental new things about the earliest phases of structure formation, cosmology and even has the potential to lead to the discovery of new physical phenomena. Here we present a white paper with an

---

Garrelt Mellema · Kannan K. Datta · Hannes Jensen
Dept. of Astronomy & Oskar Klein Center, Stockholm University, Sweden

Leon V. E. Koopmans · Soobash Daiboo · Ger A. de Bruyn · Ronniy Joseph · André Offringa · Harish Vedantham · Saleem Zaroubi
Kapteyn Astronomical Institute, University of Groningen, the Netherlands

Filipe Abdalla
Dept. of Physics and Astronomy, University College London, UK

Gianni Bernardi
Center for Astrophysics, Harvard University, USA

Benedetta Ciardi
Max Plank Institute for Astrophysics, Garching, Germany

Ger A. de Bruyn · Vibor Jelic · Panos Labroupoulos · V. N. Pandey · Sarod Yatawatta
ASTRON, Dwingeloo, the Netherlands

Heino Falcke
Department of Astronomy, Radboud University, Nijmegen

Andrea Ferrara · Andrei Mesinger
Scuola Normale Superiore, Pisa, Italy

Ilian T. Iliev
Dept. of Physics and Astronomy, Sussex University, UK

Fabio Iocco
Dept. of Physics & Oskar Klein Center, Stockholm University, Sweden Avery Meiksin
Institute for Astronomy, University of Edinburgh, UK

Jonathan R. Pritchard
Dept. of Physics, Imperial College, London, UK

Mario G. Santos
CENTRA, Instituto Superior Tecnico, Technical University of Lisbon, Portugal

Dominik J. Schwarz
Faculty of Physics, Bielefeld University, Germany

Benoit Semelin
Observatoire de Paris, France

overview of the science questions that SKA-low can address, how we plan to tackle these questions and what this implies for the basic design of the telescope.

Keywords cosmology: observations – dark ages, reionization, first stars – diffuse radiation – intergalactic medium – radio lines: general – techniques: interferometric

PACS 95.55.Jz, 95.85.Bh, 98.62.Ra, 98.80.Es, 98.62.Ai9, 8.70.Vc

Executive Summary

The *Square Kilometre Array* (SKA) will have a low frequency component (AA–low/SKA–low[1]) which has as one of its main science goals the study of the redshifted 21cm line from the earliest phases of star and galaxy formation in the Universe (see SKA Memo 125). It is during this phase that the first building blocks of the galaxies that we see around us today, including our own Milky Way, were formed. It is a crucial period for understanding the history of the Universe and one for which we have currently very little observational data.

We divide the period into two different phases based on the physical processes which affect the Intergalactic Medium. The first period, which we call the Cosmic Dawn, saw the formation of the first stars and accreting black holes, which changed the quantum state of the still neutral Intergalactic Medium. The second period, known as the Epoch of Reionization, is the one during which large areas between the galaxies were photo-ionized by the radiation produced in galaxies and which ended when the Intergalactic Medium had become completely ionized.

Observations of the redshifted 21-cm line with SKA will provide a new and unique window on the entire period of Cosmic Dawn and Reionization. The signal is sensitive to the emergence of the first stellar populations, radiation from growing massive black holes and the formation of larger groups of galaxies and bright quasars. At the same time it maps the distribution of most of the baryonic matter in the Universe. The study of the redshifted 21cm line will teach us fundamental new things about the earliest phases of structure formation and cosmology. It even has the potential to lead to the discovery of new physical phenomena. Here we present an overview of the science questions that SKA–low can address, how we plan to tackle these questions and what this implies for the basic design of the telescope.

The redshifted 21cm signal will be analyzed with different techniques, which each come with their own requirements for the SKA: (i) Tomography, (ii) power-spectra and higher-order statistics, (iii) hydrogen absorption, (iv) global/total-intensity signal. Whereas all precursors/pathfinders aim to study the signal statistically through its power spectrum, SKA will be able to image the neutral hydrogen distribution directly and its focus will therefore be more on tomography. This introduces somewhat different requirements for the design of the radio interferometer than power-spectrum studies do. At the same time the SKA will have enough collecting area to explore lower frequencies and thus earlier epochs than any of its precursors/pathfinders. Through both of these improvements SKA will revolutionize the study of the Cosmic Dawn and Reionization.

We argue that for an optimal study of the 21-cm signal through the period of the Cosmic Dawn and the Epoch of Reionization, a basic reference design for SKA-low should have at least the following:

1. An absolute minimal frequency range 54–190 MHz; an optimal frequency range 54–215 MHz and a wide frequency range of 40–240 MHz.
2. A frequency resolution of ∼1 KHz.
3. A physical collecting area $A_{\rm coll} \gtrsim 1\,{\rm km}^2 \times (\nu_{\rm opt}/100{\rm MHz})^{-2}$ for $\nu_{\rm opt} < 100$ MHz and at least $1\,{\rm km}^2$ for $\nu_{\rm opt} \geq 100$ MHz.
4. An optimal frequency ($\nu_{\rm opt}$; corresponding to a $\lambda/2$ size of a receiver dipole) around 100 MHz.
5. A core area with a diameter of $\lesssim 5$ km with most collecting area (∼75%) inside the inner 2 km.
6. A set of longer baselines (∼ 10–20% of the core collecting area) up to ∼100 km for calibration, ionospheric modeling and for building a detailed sky model.
7. A station size of order ∼35 m which corresponds to a 2.5–10 degree field-of-view from 200 MHz down to 50 MHz.

The proposed basic SKA-low array design allows most Cosmic Dawn and Epoch of Reionization science goals described in this white paper to be reached within 1000 hrs of observing time, but the capabilities of this new and unprecedented radio telescope will undoubtedly also raise many new and exciting scientific questions.

---

[1] We will use both names throughout the White Paper, mostly indicating the very low frequency ($\lesssim$ 250 MHz) part of the SKA array interesting for HI studies at redshift $z \gtrsim 5$.

1 Introduction and motivation

This white paper[2] is meant to provide a background for the development of the Square Kilometer Array from the point of view of research on reionization and the Cosmic Dawn. Since the writing of the SKA Science book in 2004 there has been major progress in the field and we felt there was a need for an update. At the same time the road to the construction of the SKA is becoming more and more clear, with the official SKA Organization having been founded in November 2011, the results of the site selection process having been announced in May 2012 (with SKA-low being build in Australia) and with an SKA Director-General having been appointed in September 2012.

Given these developments, the European SKA Epoch-of-Reionization Science Working Group (SKA-EoR-SWG) felt it was timely to summarize what Cosmic-Dawn/EoR science can be done with the SKA, how it can be done and what this implies for the design of the telescope. The contents of the current version is mostly based on experience in Europe, but we envisage it to become a 'living document' and welcome contributions from the wider (global) community. The ultimate aim is to achieve the best possible design for an SKA-low, allowing it to accomplish the science as layed out in this White Paper and motivated by the goals of SKA memo 125.

We intend to update this White Paper on a regular basis to reflect progress in the field and developments within the SKA project.

2 Science

Studies of the earliest epochs of star formation in the Universe are one of the major frontiers of modern astronomy and cosmology. After decoupling from radiation the matter cooled and its density decreased as the Universe further expanded, starting a period called the Dark Ages, named so because of the absence of any light sources. The small density fluctuations left over from inflation grew under the force of gravity to eventually form the first nonlinear structures of dark and baryonic matter. In these first halos the gas collapsed to form the first stars. Merging and accretion gradually led to the formation of larger and larger structures, up to the scales of small galaxies. The formation of those first sources of radiation ultimately changed the Universe from the smallest to the largest scales, and represents its last global transition, from a cold and neutral state to mostly warm and ionized. This process is referred to as the *Epoch of Reionization* (EoR) and was likely quite extended in time. Presently we only have indirect observations of this process, apart from the detection of some rare sources (see Section 2.1) and much remains unclear about its timing and duration, as well as the nature of the main sources of ionizing photons. In this white paper we will follow the most recent theoretical models and indirect observables as a guidance.

The ΛCDM model of the Universe predicts that the very first luminous objects may have appeared around a redshift of 50, but it took until much later, $z \lesssim 15$, before substantial ionization of the Intergalactic Medium (IGM) occurred. This transitionary period after the formation of the first luminous sources and before substantial ionization of the IGM, we will call the *Cosmic Dawn*[3]. During this era ultra-violet radiation from the first generations of stars was capable of gradually changing the quantum state of the cold neutral hydrogen, making it observable in 21cm absorption. The first generations of X-ray sources formed from the first generations of stars and subsequently heated the IGM, changing the HI signal from absorption to emission. Around the same time, or slightly later, the individual, small regions of ionized hydrogen around galaxies started to percolate, both due to the strong clustering of the first sources (see Sect. 3.1) and the exponential growth of structures. This led to the formation of giant regions of ionized hydrogen, up to several tens of comoving Mpc (cMpc[4]) across (see Sect. 3.1) which ultimately overlapped to complete reionization around redshift $z \sim 6$.

The SKA will observe this era using the redshifted 21cm line of neutral hydrogen. The brightness of this line as produced in the intergalactic medium can be written as (Field 1959; Madau et al. 1997):

$$\delta T_{\mathrm{b}} = \frac{3 h_{\mathrm{p}} c^3 A_{21\mathrm{cm}}}{32 \pi k_{\mathrm{B}} \nu_{21\mathrm{cm}}^2} \frac{n_{\mathrm{HI}}}{(1+z) H(z)} \left(1 - \frac{T_{\mathrm{CMB}}(z)}{T_{\mathrm{s}}}\right) \left(1 + \frac{1}{H(z)} \frac{\mathrm{d}v_{\parallel}}{\mathrm{d}r_{\parallel}}\right)^{-1} \tag{1}$$

where h_{p} is Planck's constant, c the speed of light, k_{B} the Boltzmann constant; $A_{21\mathrm{cm}}$ and $\nu_{21\mathrm{cm}}$ are the Einstein A-coefficient and frequency of the 21cm transition, respectively. The cosmological parameters entering the equation are the redshift-dependent Hubble parameter, $H(z)$, the Cosmic Microwave Background (CMB) temperature,

---

[2] This first draft of this white paper was written during a three day workshop at the Oskar Klein Centre in Stockholm, January 18 – 20, 2012.

[3] Sometimes this period is called the *Late Dark Ages* but this is confusing as the Universe at those times did contain sources of radiation and therefore was no longer truly dark

[4] We will use cMpc for comoving Mpc and pMpc for proper Mpc; without any prefix Mpc means cMpc

$T_{\rm CMB}(z)$, and the redshift z of the signal. The gas properties are given by the HI number density, $n_{\rm HI}$, the proper gradient along the line of sight of the peculiar velocity, $\mathrm{d}v_{\|}/\mathrm{d}r_{\|}$, and the spin (or excitation) temperature of the 21cm transition, $T_{\rm s}$.

Using cosmological parameters to express the density in terms of the overdensity $\delta = \rho/\langle\rho\rangle - 1$ and scaling to canonical values we obtain

$$\delta T_{\rm b} \approx 27 x_{\rm HI}(1+\delta)\left(\frac{1+z}{10}\right)^{\frac{1}{2}}\left(1-\frac{T_{\rm CMB}(z)}{T_{\rm s}}\right)\left(\frac{\Omega_{\rm b}}{0.044}\frac{h}{0.7}\right)\left(\frac{\Omega_{\rm m}}{0.27}\right)^{\frac{1}{2}} \left(\frac{1-Y_{\rm p}}{1-0.248}\right)\left(1+\frac{1}{H(z)}\frac{\mathrm{d}v_{\|}}{\mathrm{d}r_{\|}}\right)^{-1} \quad \mathrm{mK}, \tag{2}$$

with $x_{\rm HI}$ the neutral hydrogen fraction, $\Omega_{\rm m}$ and $\Omega_{\rm b}$, the total matter and baryon density in terms of the critical density, and $Y_{\rm p}$, the primordial helium abundance by mass.

The 21cm radiation thus provides us with information on the ionization state of the IGM, its density, the line of sight (LOS) velocity gradient and the spin temperature. The latter couples strongly to kinetic gas temperature when a sufficiently high flux of UV photons is available (the Wouthuysen-Field effect, as explained in Section 3.1.3), or in regions of sufficiently high density. Furthermore, the observed frequency contains information about the emission redshift, which along with the sky position will allow three-dimensional tomography of the IGM (Madau et al. 1997). This will help us to answer important questions on early galaxy formation, the state of the intergalactic medium, cosmology and perhaps even lead to the discovery of new, unexpected physical phenomena.

2.1 First generations of galaxies

The measurements with SKA will provide a unique window into the properties of the first generations of galaxies. Optical/near-infrared observations have been successful in detecting galaxies from redshifts as high as 8, or perhaps even 12 (Bouwens et al. 2010, 2011; Ellis et al. 2013; Oesch et al. 2013). These observations suggest that by that time some fairly substantial galaxies had already developed and that star formation had been ongoing for at least 10^8 years before that epoch (Labbé et al. 2010). However, since these galaxies are faint, only the tip of the iceberg can be detected with current telescopes and the detected galaxies cannot by themselves have reionized the Universe. Extrapolating from the observed galaxies to fainter ones requires assumptions about the highly uncertain faint end slope of the luminosity function, leading to debates on whether star forming galaxies can have been responsible for the reionization of the Universe at all (see e.g. Lorenzoni et al. 2011; Bouwens et al. 2012).

The 21cm observations will approach the problem from a different angle as the removal of neutral hydrogen from the IGM will depend on the integrated extreme ultra-violet (EUV) flux of *all* sources. Under the assumption that star formation in galaxies was responsible for reionization, we will thus be able to measure the combined effect of all galaxies and map out the cosmic star formation rate during the epoch of reionization. The morphologies of the HII regions can help us characterize the dominant types of galaxies responsible, as galaxies of different masses have different clustering properties. Morphology may also help in establishing whether sources other than stars played an important role, such as rare bright quasi-stellar objects (QSOs). Furthermore, the distribution of ionized regions will provide a crude map of the cosmic web of structure at these early epochs as simulations show that even then the sources concentrated along filaments.

QSOs, powered by accretion onto a central supermassive black hole (SMBH) are the most extreme of the class of objects producing very hard (X-ray) radiation. Due to the frequency dependence of the hydrogen ionization cross-section, X-ray radiation is more efficient at heating the IGM than at ionizing it. Different heating histories then could be traced through the redshifted 21cm signal as the strength of the signal depends on the spin temperature, which in turn depends on the gas temperature (see Section 3.1 for further discussion). Mapping out the temperature evolution of the IGM before full ionization from initially cold to warm will thus provide another diagnostic on the evolution of galaxies and their constituents (e.g. Santos et al. 2010; Baek et al. 2010; Ciardi et al. 2012; Pritchard & Loeb 2012). Since the energy required to heat the IGM above the CMB temperature is less than 1 eV per baryon, the expectation is that this heating happened before substantial ionization. We will thus be able to extend our history of structure formation well beyond redshift 10, perhaps as far as 20.

Most likely before any substantial heating, ultra-violet radiation from the very first generations of stars was capable of decreasing the spin temperature of the cold neutral hydrogen from the CMB temperature to its kinetic temperature, thus making it observable in absorption. The fluctuations in the 21cm signal caused by the patchiness of this process carry information about the distribution of these first generations of stars. This signal originates most likely from even before redshift 20.

2.2 Evolution of the Intergalactic Medium

The SKA measurements of the 21cm signal will in the first place provide information on the intergalactic medium. The size and distribution of ionized regions will give us information about how patchy and extended the reionization process was, relevant for understanding the temperature structure of the IGM for a substantial period after reionization (Theuns et al. 2002; Hui & Haiman 2003). Images of the 21cm signal in neutral regions will show the level of density fluctuations in the IGM, essentially a masked version of the baryonic density distribution.

The signal before substantial ionization should give us an even clearer picture of the baryonic density power spectrum, as well as information about the temperature distribution. The 21cm signal is the only way to get information about the large scale IGM, the environment which forms the initial condition for galaxy formation and the CD/EoR is the last epoch when two dimensional maps of the IGM at different redshifts can be made.

It is important to stress that these measurements will provide us with unique information on the structure of the Universe. Even today, most of the baryonic matter is not locked up in galaxies but is distributed between them, and only tiny fractions of it are observable. During the Cosmic Dawn and the EoR the collapsed fraction was less than 1% and the 21cm observations can thus map out the three-dimensional distribution of matter in the Universe at that age. It will provide an important check on our current ideas about structure formation according to the ΛCDM model as the density fluctuations during these epochs were the result of the action of gravity on the density fluctuations observed in the CMB.

A very relevant example of this is the recent prediction of supersonic bulk flows in the neutral hydrogen on scales of a few cMpc with large scale variations on scales of $\sim$100 cMpc (Tseliakhovich & Hirata 2010). This effect is caused by a quadratic term in the evolutionary equations of large scale structure which previously (incorrectly) had been neglected. Although a small effect, its consequences for reionization and 21cm brightness temperature fluctuations are expected to be important. Firstly, the effect suppresses star formation in small mass haloes (e.g. Maio et al. 2011; Fialkov et al. 2012; McQuinn & O'Leary 2012), pushing reionization to somewhat lower redshifts because of the additional IGM velocity. Secondly, the relative velocity between dark matter and gas enhances large scale clustering and produces a prominent cosmic web on $\sim$100 cMpc scales in the 21cm brightness temperature distribution (Visbal et al. 2012). In particular the latter effect might make the detection of large scale intensity fluctuations much easier at redshifts as high as $\sim$20. With a low enough frequency capability, SKA-low should be able to study this effect.

2.3 Cosmology

The two sections above deal with astrophysics, but the 21cm signal can also be used for more fundamental cosmological measurements. This is because inhomogeneities in the HI gas density field, which contribute to the 21cm signal, should trace those of the underlying CDM, and thus, of the fundamental cosmological parameters that define the power spectrum of the linear density field (Tozzi et al. 2000; Zaldarriaga et al. 2004; Bowman et al. 2007; McQuinn et al. 2006).

Note that, contrary to the CMB, we will be observing the signal across several redshifts, thus having access to a large volume, which is an enormous advantage for a proper cosmological analysis. Considering, as an example, a full sky experiment with SKA resolution of an arcminute at $z \sim 20$ and with depth 10 MHz, the number of independent modes available for measurement would be $N_{21\mathrm{cm}} \sim 7 \times 10^{10}$, which is 10^3 more than what is available in the CMB (Loeb & Zaldarriaga 2004). A field of 36 deg^2 would have approximately as many modes as the full sky CMB.

Moreover, 21cm experiments will probe an epoch in the evolution of the Universe that is inaccessible to any other experiment, thus providing a handle on non-standard phenomena such as early dark-energy models. Unfortunately, the other "astrophysical" contributions to the 21cm signal will complicate the analysis and deteriorate the constraints on the cosmological parameters (Santos & Cooray 2006; McQuinn et al. 2006; Mao et al. 2008). The cosmological analysis of the 21cm signal will be essentially based on measurements of its three-dimensional power spectrum (see Section 3.3) and its evolution across cosmic time, although other observables could be used to get a better handle on the astrophysical contributions.

In the high precision cosmology era that we are entering, even if 21cm experiments cannot be competitive with other experiments such as Planck for the case of the standard cosmological model, they will help to put stringent constraints on the reionization history, thus helping to break degeneracies with other parameters measured by Planck, such as the running of the primordial spectral index (Pandolfi et al. 2010). Also, Mao et al. (2008) showed that at lower redshifts ($z < 9$), it should be possible to use tomographic measurements with the SKA to improve the sensitivity to spatial curvature and neutrino masses compared to Planck by a factor of 6 to $\Delta\Omega_k \approx 0.004$ and $\Delta m_\mu \approx 0.056$ eV (using Planck priors). The constraints on the curvature of the Universe have the advantage that they are less sensitive to uncertainties in the dark energy equation of state than the CMB alone (Knox 2006).

2.4 New Physics

Since we are entering unchartered waters, there are many opportunities for discovering new physics phenomena with SKA-low. Here we summarize some of these.

- **DM annihilation**
  Physically motivated Dark Matter (DM) models predict that the DM candidate may either decay or annihilate into standard model particles (see Bertone et al. 2005, for a review). The annihilation or the decay of even a fraction of the DM (which may be constituted of different species, coupled differently to the Standard Model of particle physics) would inject a shower of particles in the environment where the annihilation/decay takes place. The nature and spectrum of such a shower depends on the very nature of the DM, with a natural endpoint at the mass of the DM particle itself, $m_{\rm DM}$. In models popular today, such as those arising from SuperSymmetry or Kaluza-Klein theories, $m_{\rm DM}$ ranges between few GeV and few TeV: both leptons or hadrons injected at such energies will be partially absorbed by the environment, thus depositing energy which contributes to heat and ionize the IGM.
  The alteration of the ionization state of the IGM may be seen through the CMB cross-correlation power spectra (Padmanabhan & Finkbeiner 2005; Mapelli et al. 2006), and the forthcoming PLANCK data may show hints of, or rule out low mass DM particles self-annihilating with cross sections at the level required for thermal production in the early Universe (Galli et al. 2009)
  Yet, CMB loses sensitivity at particle masses higher than m_{DM} ∼50GeV and for decaying DM (Galli et al. 2009), whereas the 21cm line is best suited to explore this regime due to its sensitivity to smaller (and later-timed) energy injections (Furlanetto et al. 2006b). Expected brightness fluctuations at redshift $z \sim 50$ are of the order of fractions of a mK, with an amplitude of ∼2 for annihilating DM, and up to an order of magnitude lower for decaying DM, extending with weaker strength to lower redshifts $z \sim 20$. In light of the different dependence of such fluctuations on DM parameters (annihilation versus decay, mass, injected primary spectrum), their detection will help shedding light on the nature of DM itself, allowing to constrain lifetimes $\lesssim 10^{27}$s and self annihilation cross section $\langle \sigma v \rangle \sim 10^{-26}$cm^3/s (for $m_{\rm DM}$= 100GeV).
- **Evaporating black holes**
  Many inflationary scenarios predict the production of primordial black holes via the collapse of overdense peaks in the initial density field. Primordial black holes with masses in the range $M_{\rm pbh} = 10^{14} - 10^{17}$ g will evaporate via the release of Hawking radiation between recombination and present day (Ricotti et al. 2008). They therefore represent a possible source of IGM heating relevant for 21cm studies, which could result in spin temperature fluctuations (Mack & Wesley 2008). 21cm studies are most sensitive to the mass range $M_{\rm pbh} \sim 10^{14}$ g, which evaporate in a burst at redshifts $z \sim 30$ and, at sufficient number densities, could heat the IGM above the CMB temperature before star formation began. Higher mass primordial black holes would be hard to distinguish from decaying DM.
- **Cosmic strings**
  Cosmic strings are one dimensional topological defects that can be produced in particle physics phase transitions. As they move they produce a wake that stirs up the IGM inducing temperature and density fluctuations. Strings were originally put forward as a source of cosmological density fluctuations for seeding the growth of structure, although the high string densities this requires are now excluded by CMB observations. At lower number densities, cosmic strings might still exist and could be constrained via their heating effect on the IGM (Brandenberger et al. 2010). String wakes would appear as extended wedge-shaped regions with the string at the tip seen as emission features in high resolution 21cm maps. String tensions of $G\mu \lesssim 6 \times 10^{-7}$ might

be constrained and the strings typically span a Hubble radius in size. At high redshifts ($z \gtrsim 30$), future 21cm experiments should be able to constrain cosmic strings with tension $G\mu \sim 10^{-11}$ (Khatri & Wandelt 2008).

- **Variations in the fine structure constant (α)**
  The 21cm signal is very sensitive to the variations in α (e.g. $\nu_{21} \propto \alpha^4$, $A_{10} \propto \alpha^{13}$) and it is so far the only probe of the fine structure constant between recombination and $z \sim 8$. This effect can in principle be probed at high redshifts since a 1% change in α changes the signal by $> 5\%$ and imprints a characteristic evolution with redshift (Khatri & Wandelt 2007). However, since astrophysical effects are expected to affect the 21cm signal in the SKA frequency range, it may be hard to detect this signature with SKA.

3 Analysis of redshifted 21cm signal

The signal we want to observe is the redshifted 21cm signal from neutral hydrogen. This section explains in more detail how this signal depends on the astrophysical and cosmological parameters and the various ways in which it can be analyzed in order to study the topics outlined in Section 2.

3.1 Description of $\delta \mathrm{T_b}$ and its dependencies

The measurable quantity is the differential brightness temperature $\delta \mathrm{T_b}$. Equations 1 and 2 in Section 2 describe how it depends on the local properties of the IGM and on global cosmological parameters. Before we examine the various contributions, let us summarize the underlying assumptions of these equations.

- The IGM is assumed to be homogenous on kpc scales (within the 21cm line profile)
- The 21cm line is optically thin. The optical depth of the line is given by

$$\begin{aligned}\tau_{21\mathrm{cm}}(z) &= \frac{3}{32\pi}\frac{h_p c^3 A_{21\mathrm{cm}}}{k_B \nu_{21\mathrm{cm}}^2}\frac{x_{\mathrm{HI}} n_{\mathrm{H}}}{T_{\mathrm{S}}(1+z)(dv_\parallel/dr_\parallel)} \\ &= 9.6\times 10^{-3} x_{\mathrm{HI}}(1+\delta)\left(\frac{1+z}{10}\right)^{3/2} \\ &\left(\frac{T_{\mathrm{CMB}}}{T_{\mathrm{S}}}\right)\left[\frac{H(z)/(1+z)}{dv_\parallel/dr_\parallel}\right],\end{aligned} \tag{3}$$

which combined with the radiative transfer solution

$$\delta T_{\mathrm{b}} = (1+z)^{-1}(T_{\mathrm{S}} - T_{\mathrm{CMB}})\left(1-e^{-\tau_{21\mathrm{cm}}}\right), \tag{4}$$

for $\tau_{21\mathrm{cm}} \ll 1$ gives the solution in Equation 1. The assumption of low optical depth fails at $\delta > 10$ in fully neutral regions which is for example the case in DM halos of masses $\lesssim 10^7\ \mathrm{M}_\odot$ (also known as minihalos).

For the SKA science case, the most important aspect will be the fluctuations in the signal (see Fig. 1) since this is where the sensitivity and resolution of the instrument will bring the largest improvement over previous surveys. We can see from Equation 2 that fluctuations in δT_b originate from four different contributions:

1. fluctuations in the matter overdensity δ
2. fluctuations in the hydrogen neutral fraction x_{HI}
3. fluctuations in the spin temperature T_{S}
4. fluctuations in the line of sight velocity gradients.

3.1.1 Fluctuations from overdensity

These are the most straightforward to calculate as they result from the growth of cosmic structures. On comoving Mpc scales (which is the likely resolution of the SKA), the hydrogen density fluctuations are closely correlated to the Dark Matter fluctuations which only depend on the assumed cosmology and can be calculated using linear theory for most scales of interest. Baryon physics will be important mostly for the three other types of fluctuations. Density fluctuations dominate the signal during the Dark Ages (at $z > 30$). They can also be dominant at lower

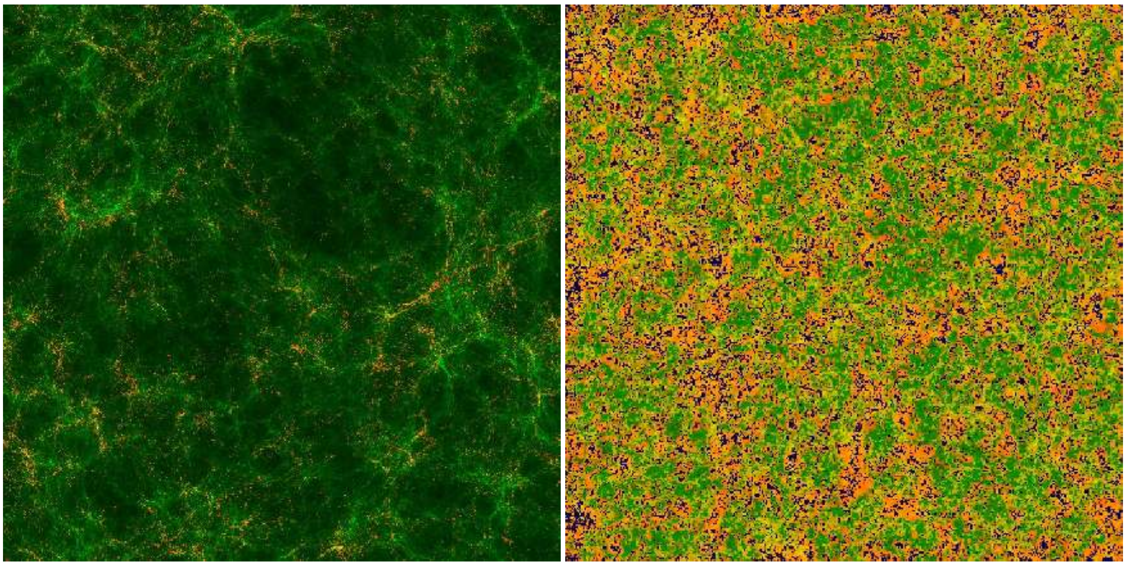

Fig. 1 *Left panel*: Cosmic Web at redshift $z = 8$ from an N-body simulation with boxsize $20h^{-1}$ cMpc and $5488^3 = 165$ billion particles resolving the halos hosting the first stars ($M > 10^5 M_\odot$). Shown are projections of the total density (green) and halos (orange). *Right panel*: Spatial slices of the ionized and neutral gas density at $z = 8$ from radiative transfer simulation with volume $425h^{-1}$ cMpc to a side. Shown are the density field (green) overlayed with the ionized fraction (red/orange/yellow) and the cells containing sources (dark/blue). Courtesy of I. T. Iliev and G. Mellema. More details about this simulation can be found in Shapiro et al. (2012a).

redshifts, during the Cosmic Dawn era if three criteria are met: the average ionization is still very small, the spin temperature is already globally coupled to the gas temperature (strong local Ly-α flux, see below) and the gas temperature is globally much higher than the CMB temperature so its fluctuations are damped. Such a regime may exist if there is a substantial population of X-ray sources during the Cosmic Dawn. Otherwise, overdensity fluctuations are mixed with fluctuations in both the spin temperature and neutral fraction.

3.1.2 Fluctuations from neutral fraction

Fluctuations in the neutral fraction are connected to the process of patchy reionization itself. The period in which these fluctuations are dominant is the one that we refer to as the Epoch of Reionization (EoR). The topology of these fluctuations depends on the nature of the sources (pervasive ionization for very hard X-ray sources, sharp fronts and bubbles for stellar type sources), their clustering properties, and the ionizing flux escaping into the IGM as a function of halo mass. Characterizing these fluctuations with respect to the source models is an important part of the scientific preparation of the SKA. Fluctuations in the neutral fraction dominate when the ionized regions are large enough to fill resolution elements of the telescope, provided the spin temperature is fully coupled to the gas temperature and the gas is heated to temperatures $\sim 10 \times T_{\rm CMB}$. The spin temperature coupling is expected to occur early, well before any significant ionization. Substantial heating may happen early but does depend on the amount of X-rays produced (e.g. Pritchard & Loeb 2012).

3.1.3 Fluctuations from the spin temperature

Fluctuations in the brightness temperature produced by fluctuations in the spin temperature are the less straightforward of the four. The local value of the spin temperature is the result of four competing processes (e.g. Furlanetto et al. 2006a):

1. coupling to the CMB temperature through absorption/re-emission of CMB photons
2. coupling to the gas kinetic temperature through collisions
3. coupling to the color temperature of the local radiation spectrum near the Ly-α frequency through resonant scattering (Wouthuysen-Field effect).
4. coupling to the local brightness temperature in the vicinity of radio-loud sources.

The last effect occurs when near radio-loud sources the 21cm photons from that source dominate over the 21cm photons from the CMB. In what follows we will not consider this localized effect.

As a result T_S can be written as:

$$T_S^{-1} = \frac{T_\mathrm{CMB}^{-1} + x_\alpha T_c^{-1} + x_c T_K^{-1}}{1 + x_\alpha + x_c}\,. \tag{5}$$

Here T_c is the color temperature of the Ly-α spectrum which is almost equal to T_K in situations relevant for the EoR (see Hirata 2006, for details). The factor x_c, the coupling coefficient though collisions, is non-negligible only in dense environments. The necessary densities for this are the average density for $z > 30$ or in a correspondingly overdense regions at lower redshifts. The coupling coefficient through Ly-α scattering, x_α, is proportional to the local Ly-α flux, modulated by a back-reaction factor (Chuzhoy & Shapiro 2006). The local Ly-α flux is determined by the distribution and luminosity of sources of ultra-violet radiation but also by the global neutral hydrogen distribution (Semelin et al. 2007). For more details on the computation of x_α and x_c see e.g. Furlanetto et al. (2006a).

Summarizing, for the epochs that can be studied by the SKA, fluctuations in the spin temperature are caused by fluctuations in the local kinetic temperature of the gas and fluctuations in the local Ly-α flux. Depending on the nature of the radiation sources, both the kinetic temperature and Ly-α flux can dominate the brightness power spectrum in the early EoR (Santos et al. 2008; Baek et al. 2010; Pritchard & Loeb 2012). The most likely scenario is that star forming galaxies produce sufficient ultra-violet photons to achieve complete Ly-α coupling quite early, perhaps even before $z = 20$, after which the spin temperature fluctuations are set by the gas temperature fluctuations. The latter is initially lower than the CMB temperature, leading to a strong global absorption signal, with fluctuations determined by adiabatic cooling. As X-ray sources start heating the neutral IGM, strong spin temperature fluctuations between cold and heated regions will appear, which will slowly disappear as the medium becomes more uniformly heated.

We note that the bulk-flows as discussed in Section 2.2 can lead to large scale fluctuations in the spin temperature. This will substantially increase the observability of brightness-temperature fluctuations during the Cosmic Dawn (Visbal et al. 2012; McQuinn & O'Leary 2012) and so allow SKA to study these higher redshifts in greater detail than previously thought.

3.1.4 Fluctuations from peculiar velocity

Unlike the three former sources of fluctuation, fluctuations induced by local velocity gradients are statistically anisotropic since only the projection of the gradient along the line of sight has an effect on the brightness temperature. Even if, overall, these fluctuations are weaker than the others, their anisotropic behavior is unique, and in the linear approximation, their power spectrum can be separated from the other sources of fluctuations, see Section 3.5. Moreover, at high z, in the linear regime, they are locally proportional to the fluctuations in the density field, so they can be used to probe the linear growth of structure (Barkana & Loeb 2005a), and constrain the cosmological parameters (Section 2.3). To derive high quality estimates of the cosmological parameters from observations with the SKA, however, it will be necessary to go beyond the simple linear treatment (e.g. Mao et al. 2012).

3.2 Tomography and its analysis

As explained above, during the EoR in a typical region of the IGM, the 21cm line is optically thin: once emitted, a photon is redshifted out of the line before it is re-absorbed. Therefore the redshifted 21cm signal carries information from the time and place where it was generated and thus it enables tomography of the signal. Even in the case where the thermal width of the line is set by a $T_K > 1000$ K medium, we could theoretically image several 1000s of distinct planes between redshifts 6 and 30. In the case of the SKA, if we aim at a reasonable signal to noise (S/N) ratio, we will more likely be able to observe a few hundreds of planes. SKA precursors will not reach a sufficient S/N for tomography.

To date most studies have focused on statistical quantities such as the power spectrum, which require far less sensitivity. What additional benefits are produced from analyzing the tomography? We can distinguish two approaches:

- **Characterizing individual objects**

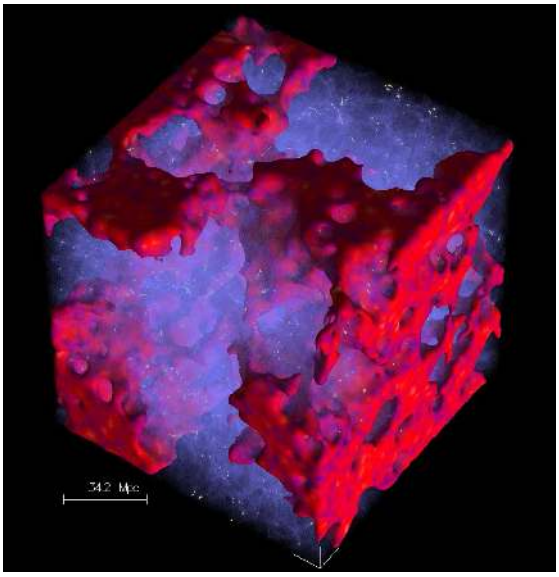

Fig. 2 A three-dimensional view of the ionization field produced by a numerical simulation. Red and non-transparent is neutral, blue and transparent is ionized material. Tomography with the redshifted 21cm line should give us a similar view of the Universe (Figure courtesy of B. Semelin).

In statistical diagnostics the local, real-space, information is lost. With tomography we should be able to identify individual features and interpret them. The simplest example is that of a single isotropic radiation source (a young galaxy, an intermediate mass black hole, etc..) which creates a distinct, roughly spherical pattern in the 21cm signal. If the average radial brightness temperature profile can be reconstructed, it can be compared to templates, and the properties of the source (luminosity and spectrum) can be inferred. There are, as yet, few works on the subject. Majumdar et al. (2012) devised an anisotropic filter to detect individual ionised bubbles around bright quasars and study how the age and luminosity of the quasar can be constrained, see also section 3.8.1. Vonlanthen et al. (2011) estimated the observability by the SKA of faint rings around ionizing sources created by the Wouthuysen-Field effect of upper Lyman lines. They emphasize how both resolution and the ability to stack a large number of objects, and thus a large FoV, are crucial factors for this type of analysis.

As the prospects of actual observations with SKA come closer, it is likely that many more ideas will emerge on how to extract information on individual objects, and combine them into statistical properties. Resolution, FoV and sensitivity will be crucial quantities for the efficiency of this approach with FoV allowing to compensate for sensitivity to some degree through the process of stacking. See Section 3.8.1 for more information about combining 21cm data with other observables from individual bright sources.

- **Studying the global topology of the signal**
  We can also consider statistical or integral quantities that can be computed from tomographic data only. While these will be computed from the brightness temperature, it should be easy to connect them to the ionization fraction as soon as the high spin temperature regime is reached.
  A first example is the bubble size distribution and its evolution with redshift (Iliev et al. 2006; Zahn et al. 2007; Friedrich et al. 2011). This is a powerful tool to test the models against the future tomographic observations, putting constraints on quantities such as the luminosity distribution of the sources at a given redshift.
  Another option is to evaluate topological quantities such as the genus (Ahn et al. 2010) or its close relative, the Euler characteristic (Friedrich et al. 2011). The evolution of these quantities with redshift can also put constraints on the source models.

The tomographic exploitation of the redshifted 21cm data is only just beginning. Some of the above cited works take into account real data limitations such as the resolution by convolving with a simple beam shape. However, robust predictions will have to factor in effects such as the sky/detector noise, imperfect foreground substraction and the complex beam shape.

Ideally we would like to be able to image the 21cm signal down to the resolution of the SKA core (arcminute scales). This should be feasible to rather low frequencies as the contrast between ionized and neutral regions is about 20 – 30 mK (at $z = 9$). Tomography of the neutral density field is harder as the level of density fluctuations at $1'$ resolution are about 4 – 6 mK (rms values at $z = 20$ and 9).

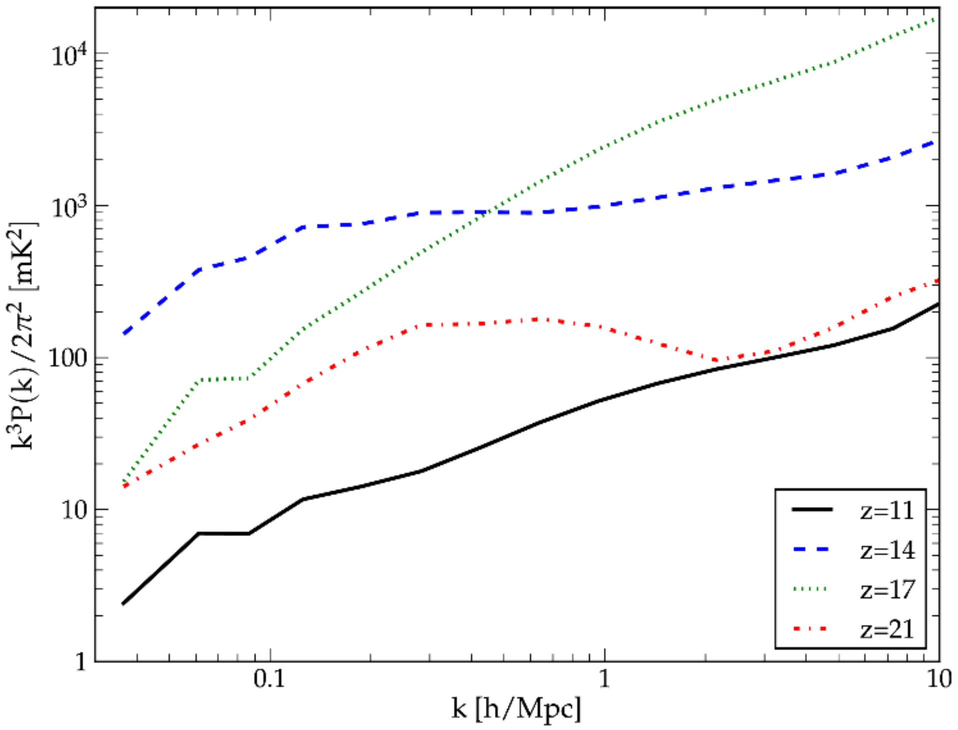

Fig. 3 A sample of spherically averaged 21cm power spectra ($k^3P(k)/(2\pi^2)$ or $\Delta^2(k)$) of the 21cm brightness temperature for $z \geq 11$. Figure 11 from Santos et al. (2010).

3.3 Power spectrum analysis

Imaging is powerful, but requires a high S/N per spatial-frequency resolution element (i.e. voxel). Therefore a need exists for alternative statistical measures that compress many individually noisy modes into quantities that can measured with high S/N. At the highest redshifts, SKA only has the sensitivity to make images on the largest scales and will have to rely largely upon statistical measurements to measure small-scale structure. At lower redshifts statistical measures are still useful as they characterize the signal with relatively few parameters summarizing properties that are harder to quantify numerically from images alone.

The main statistical measure is the power spectrum $P(\mathbf{k},z)$, the Fourier transform of the two point correlation function in real space, defined by the relation

$$\langle T_b(\mathbf{k},z)T_b(\mathbf{k}',z)\rangle = (2\pi)^3\delta^{(3)}(\mathbf{k}-\mathbf{k}')P(\mathbf{k},z), \tag{6}$$

where $\mathbf{k}$ is a wavenumber, z is the redshift and $\delta^{(3)}$ is the three-dimensional Kronecker δ–function. The power spectrum is a natural quantity to measure from interferometric visibilities which themselves represent a Fourier transform of the sky signal. It would contain all the statistical information if the signal had a Gaussian distribution (as is almost the case for the primordial density field). The presence of ionized bubbles and heating by astrophysical sources produces non-Gaussianity in the signal, which requires the use of higher order statistics (see Section 3.4). However, even when large ionized regions introduce substantial non-Gaussianity in the 21cm sigmal, the power spectrum is still useful as it provides information on typical sizes of HII regions.

The power spectrum is in general 3D, but it is common to consider the spherically averaged power spectrum $P(k,z)$, with $k = |\mathbf{k}|$ or, if redshift space distortions are accounted for, we expect there to be a cylindrical symmetry so that we may write $P(k_\perp, k_{||}, z)$ where $k_\perp$ is the wavenumber in the transverse direction and $k_{||}$ along the line of sight (McQuinn et al. 2006). As the 21cm fluctuations evolve as a function of redshift, so does the power spectrum making it important to measure it at different redshifts (Pritchard & Loeb 2008).

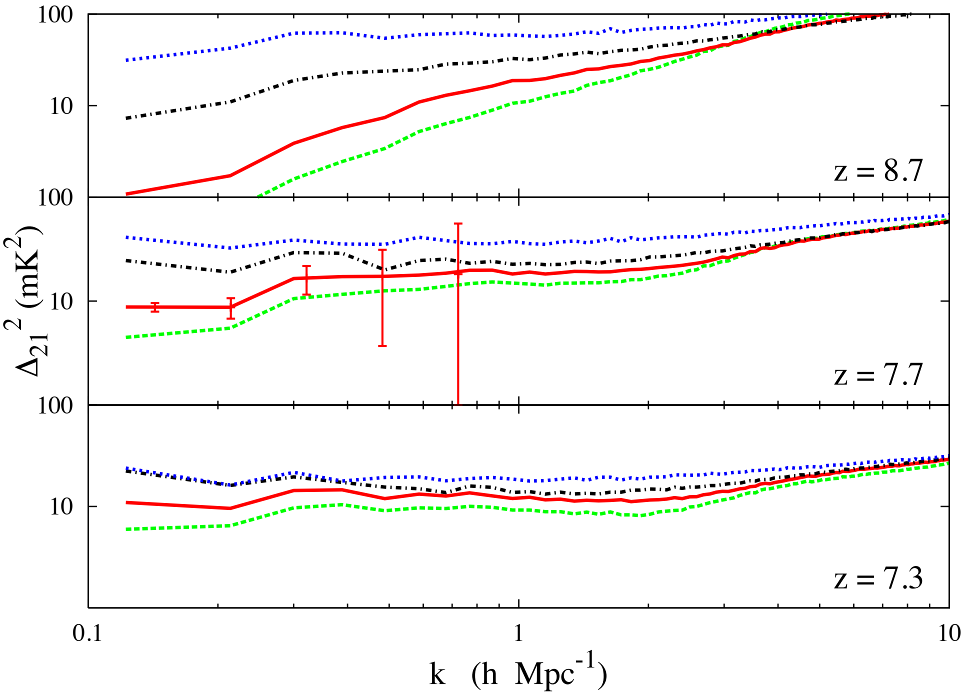

Fig. 4 A sample of spherically averaged 21cm power spectra ($k^3P(k)/(2\pi^2)$ or $\Delta^2(k)$) for four different reionization models (S1: red solid curves, S2: green dashed curves, S3: black dot-dashed curves, S4: blue dotted curves). For the top panels, the mass weighted mean ionized fraction ($x_{i,M}$) is ≈ 0.3, for the middle panels, ≈ 0.6 and for the bottom panels, ≈ 0.8. The error bars are the expected detector noise plus cosmic variance errors on the power spectrum for MWA (512 tiles), assuming 1000 h of integration and a bandwidth of 6 MHz. In model S2, reionization is driven mostly by low mass sources, in model S4 high mass sources dominate the process. Figure 17 from McQuinn et al. (2007b); for more details about the source models and other aspects, see the original paper.

During the Cosmic Dawn, when Ly-α or X-ray backgrounds drive spin-temperature fluctuations, detailed power spectrum measurements would yield information about the relative emission from galaxies and AGN (Santos et al. 2011). Figure 3 shows examples of spherically averaged 21cm brightness power spectrum as a function of wavenumber in different redshift bins during the Cosmic Dawn. The shape of $P(k,z)$ contains information about astrophysical sources. The models suggest that it is dominated by the clustering of the radiation sources on large scales and by their radiation profile on intermedate scales (Barkana & Loeb 2005b; Chuzhoy et al. 2006; Pritchard & Furlanetto 2007).

During reionization the overall shape of the power spectrum is determined by fluctuations in the neutral fraction. Simulations and theoretical work show that the key quantity that determines the shape of the power spectrum is the mean neutral fraction x_{H}, almost independently of the redshift or details of the sources (Furlanetto et al. 2004; Zahn et al. 2007; Iliev et al. 2012). However, if one looks more closely, then the details of the ionizing photon sources and the statistics of dense neutral photon sinks modify the shape of the power spectrum (McQuinn et al. 2007b). It is this level of precision that SKA should be targeting. Figure 4 illustrates this point with the power spectrum for four different ionizing source prescriptions (all normalised to produce the same neutral fraction). Distinguishing between these different models will be the driver for power spectrum sensitivity.

In practice, only a limited range of wavenumbers will be observable with sufficiently high signal to noise. The absolute smallest k is determined by the largest scale within one observation (FoV) and the absolute largest k by the resolution of the array. Table 3.3 gives an overview of typical $k_{\mathrm{min,max}}$ values for a given array configuration (see Section 5 for an extensive discussion on array configurations). At small wavenumbers, the loss of long wavelength modes along the line of sight from foreground removal is likely to limit power spectrum measurements to

Table 1: Some values of wave numbers for different angular scales at different redshifts (using $\Omega_\Lambda = 0.73$, $\Omega_{\rm m} = 0.27$, $h = 0.7$).

z	ν (MHz)	$\Delta\theta$ (5 km)	$k_{\rm max}$ (cMpc^{-1})	FoV (40m station)	$k_{\rm min}$ (cMpc^{-1})
9	142	$1.4'$	1.6	3.0°	1.3×10^{-2}
14	95	$2.2'$	0.93	4.5°	7.6×10^{-3}
19	71	$2.9'$	0.67	6.0°	5.4×10^{-3}
24	57	$3.6'$	0.52	7.5°	4.2×10^{-3}
29	47	$4.3'$	0.43	9.0°	4.2×10^{-3}

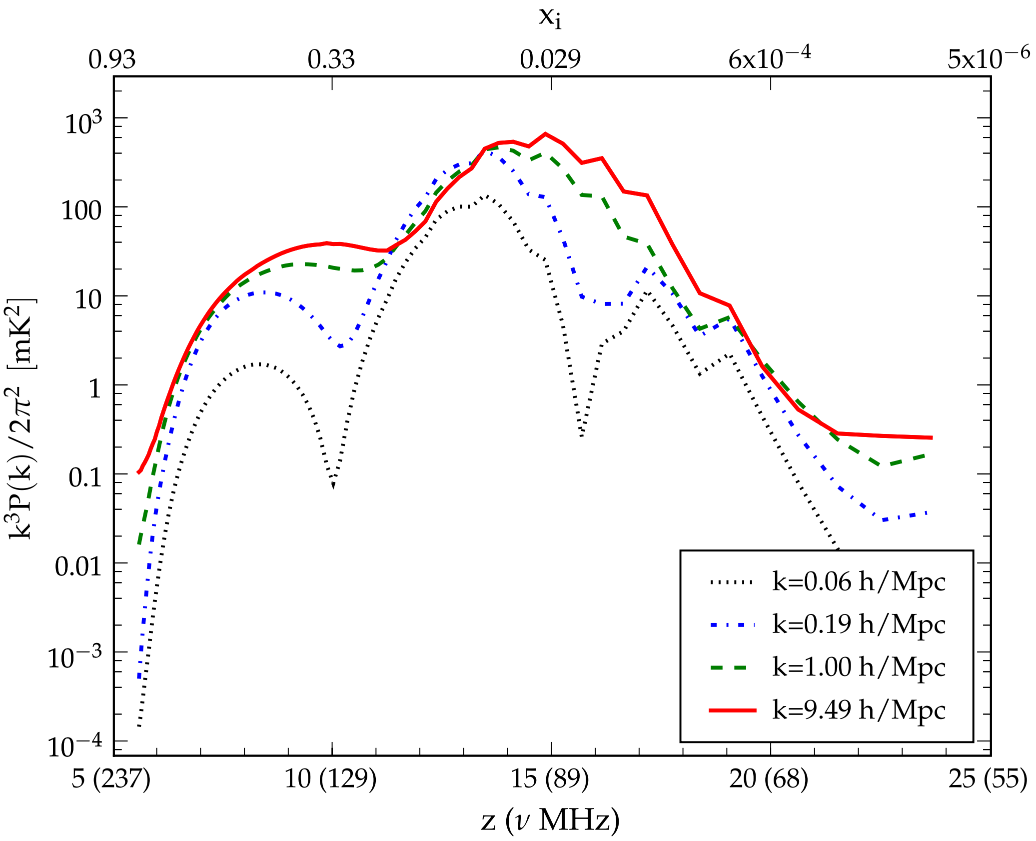

Fig. 5 Evolution of four different k-modes of the spherically averaged 21cm power spectra ($k^3P(k)/(2\pi^2)$ or $\Delta^2(k)$) with redshift. The lowest k-mode clearly shows the three epochs of Ly-α fluctuations, heating flucuations and ionization fluctuations. Figure 9 from Santos et al. (2008).

wavenumbers $k \gtrsim 0.01\,{\rm cMpc}^{-1}$. For larger wavenumbers, the increasing thermal noise due to sparse sampling of long baselines becomes a problem and is expected to limit SKA to scales $k \lesssim 5\,{\rm cMpc}^{-1}$. Between these limiting scales it should be feasible to measure the power spectrum at high precision.

Brightness temperature fluctuations from variations in the density, Ly-α flux, gas temperature, and neutral fraction evolve with redshift. This affects the power spectrum's shape and amplitude considerably. This overall evolution is captured in Figure 5, which shows the evolution of $P(k,z)$ as a function of redshift for several wavenumbers. Three different regimes can be discerned where Ly-α, temperature, and ionization fluctuations come to dominate the overall signal. By combining power spectrum measurements at different redshifts these different phases might be identified (Pritchard & Loeb 2008). Note in particular the large increase in power at $z \gtrsim 15$ during the Cosmic Dawn, which should allow SKA to probe this epoch. A caveat here is the need to select the bandwidth for individual redshift bins so that power spectrum evolution is minimised across the bin (the so-called light cone effect, see Section 3.5 and McQuinn et al. 2006; Datta et al. 2012b).

Before the power spectrum can be interpreted it must be understood and this requires detailed theoretical modeling. So far, this has followed three parallel approaches each with strengths and weaknesses. Detailed numerical simulations take a dark matter N-body code and paint on a prescription for galaxy formation and radiative transfer to produce simulation volumes. These are typically numerically expensive and so restricted to either relatively small volumes or small parts of parameter space, but are capable of high resolution giving insights into small scale structures (Mellema et al. 2006; Baek et al. 2010). At the other end of the spectrum are analytic models, which give useful insights into the power spectrum, especially in terms of its dependence on different parameters, but which tend to be relatively simple (Furlanetto et al. 2004; Pritchard & Loeb 2008). In between are semi-numerical simulations, which are in some sense specific realizations of analytic models, that are capable of simulating large volumes with an acceptable level of resolution (Mesinger et al. 2011; Santos et al. 2010). Analysis of large data sets will likely require semi-numerical simulations that have been validated by comparison against fully numerical simulations, but are interpreted with reference to insights from analytic models. At this point in time no standard framework exists to interpret observed power spectra, but steps in the direction of such a framework have been taken, see e.g. (Lidz et al. 2008; Iliev et al. 2012).

3.4 Higher order statistics

Given the nature of the reionization process the expected signal is non-Gaussian, hence using higher order statistics to characterize the data can reveal information that the power spectrum does not include. The left hand panel of Figure 6 shows an example of the Probability Density Function (PDF) of the brightness temperature at four different redshifts; the PDF is clearly non-Gaussian in all four cases. Therefore, higher order moments, like the skewness, as a function of redshift could be a useful tool for signal extraction in the presence of realistic overall levels of foregrounds and noise.

Harker et al. (2009b) (see also Gleser et al. 2006; Ichikawa et al. 2010a; Iliev et al. 2012) showed that the skewness of the 21cm signal, under generic assumptions, has a very characteristic evolution pattern against redshift (the right hand panel of Figure 6). At sufficiently high redshifts the signal is controlled by the cosmological density fluctuations which, in the linear regime, are Gaussian. At lower redshifts, and as nonlinearity becomes important, the signal starts getting a slightly positive skewness. As the ionization bubbles begin to show up the skewness veers towards zero until it crosses to the negative side when the weight of the ionized bubbles becomes more important than the high density outliers –note that high density outliers are likely to ionize first– but the distribution is still dominated by the density fluctuations. At lower redshifts the bubbles dominate the PDF and the neutral areas become the “new” outliers giving rise to a sharp positive peak to the skewness. As the end of reionization is approached the instrument noise, assumed to be Gaussian, dominates, driving the skewness again towards zero.

With high signal to noise data, one should be able to even obtain the PDF of the brightness temperature although the presense of bright foregrounds may affect this observable (Ichikawa et al. 2010b). Barkana & Loeb (2008) suggested an alternative statistic, namely the difference PDF which is the difference in 21-cm brightness temperature between two locations. This is a two-dimensional function of both the brightness temperature difference and the distance between the points. Further studies of the difference PDF show its use both in pinning down the reionization history but also put constraints on the properties of the ionizing sources (Gluscevic & Barkana 2010; Pan & Barkana 2012).

To date higher order statistics have only been explored for the EoR and the case of high spin temperature, so that the fluctuations are only due to variations in the density and ionized fraction. How they behave when substantial variations in the spin temperature exist is unknown. SKA will be sensitive enough to quantify higher-order statistics, especially at higher redshift where tomography on small angular scales might still remain hard.

3.5 Line of Sight effects / Redshift space distortion analysis

The LOS velocity gradient introduces an inhomogeneity in the three-dimensional power spectrum as the peculiar velocities shift the signal away from the cosmological redshift along the (LOS) frequency axis. If one can measure the power spectrum in terms of all three components of the wave vector **k**, one can characterize these redshift space distortions. Since only one direction differs from the others one can fully characterize the behaviour of the power spectra using k, the length of the wave vector, and μ, the cosine of the angle between the line of sight and the wave vector **k**, or $k_{\|}/k$. When only retaining linear terms in the expansion of the full power spectrum in terms of the power spectra of neutral fraction (x_{HI}) and density (δ) and assuming that $T_{\mathrm{S}} \gg T_{\mathrm{CMB}}$ one can show that the μ

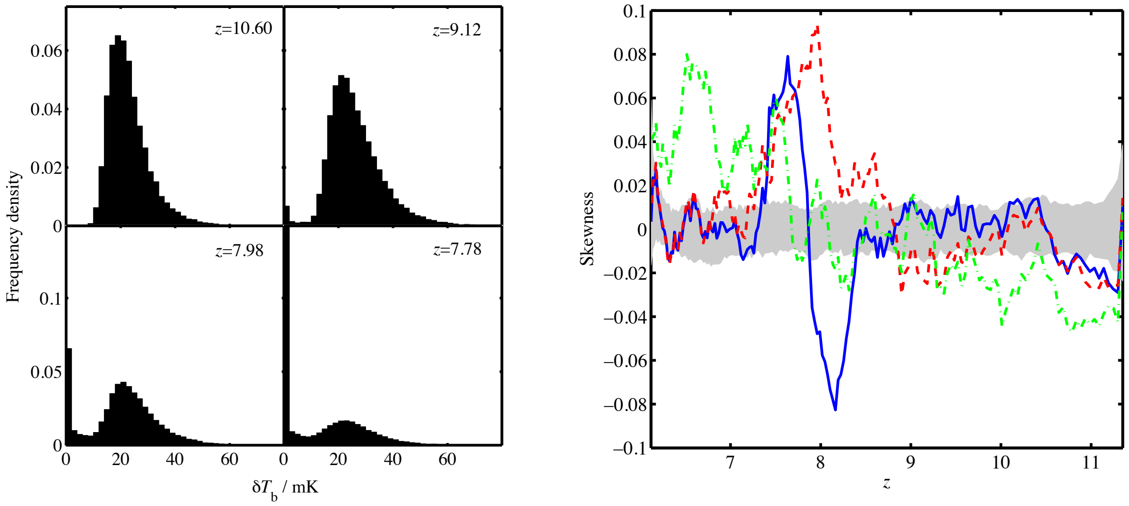

Fig. 6 *Left panel*: The distribution of $\delta T_{\rm b}$ in a certain cosmological simulation of reionization from Iliev et al. (2008) at four different redshifts, showing how the PDF evolves as reionization proceeds. Note that the y-axis scale in the top two panels is different from that in the bottom two panels. The delta-function at $\delta T_{\rm b} = 0$ grows throughout this period while the rest of the distribution retains a similar shape. The bar for the first bin in the bottom-right hand panel has been cut off; approximately 58 per cent of points are in the first bin at $z = 7.78$. *Right panel*: Skewness of the fitting residuals from data cubes with uncorrelated noise, but in which the residual image has been denoised by smoothing at each frequency before calculating the skewness. The three lines correspond to results from three different simulations from Thomas et al. (2009) and Iliev et al. (2008). Each line has been smoothed with a moving average (boxcar) filter of nine points. The grey, shaded area shows the errors, estimated using 100 realizations of the noise. Figures 1 and 6 from Harker et al. (2009b).

dependence can be written as

$$P(k,\mu,z) = P_{\mu^0}(k,z) + \mu^2 P_{\mu^2}(k,z) + \mu^4 P_{\mu^4}(k,z)\,, \tag{7}$$

where the $P_{\mu^4}(k) = P_{\delta\delta}$, the matter power spectrum, see Bharadwaj & Ali (2004); Barkana & Loeb (2005a). This conclusion also holds when one allows non-linear fluctuations in $x_{\rm HI}$ (Mao et al. 2012). It is this decomposition that opens the road to measuring $P_{\delta\delta}$ directly from the redshifted 21cm measurements.

However, the assumption of only linear variations is likely to be invalid through large parts of the EoR and in addition there is the additional LOS effect caused by evolution of $x_{\rm HI}$ and $T_{\rm S}$, the so-called light cone effect (Barkana & Loeb 2006; Datta et al. 2012b). Both the non-linear and light cone effects have not been extensively theoretically explored yet, but are likely to become more important at the later stages of ionization. The observed power spectrum may further suffer from the Alcock-Paczynski(AP)-effect when the wrong cosmological parameters are used to map the angular and frequency coordinates to real space coordinates (Nusser 2005; Barkana 2006). The AP-effect adds a μ^6 term to the μ-decomposed power spectrum of Equation 7.

The characterization of $P(k,\mu,z)$ is the first step in any analysis of all these LOS effects. The work of McQuinn et al. (2006) and Mao et al. (2008) considered the separation of the different P_μ terms in Equation 7. How successful this separation is depends on the behaviour of the different P_μ terms, which for P_{μ^0} and P_{μ^2} depends on the details of the reionization process.

The extent to which cosmological information can be extracted depends on the characteristics of the signal, which will be different for different phases of the CD/EoR. Different approaches have been proposed.

- **No assumptions on astrophysics**: In this approach only the P_{μ^4} term is used. Since this term is typically subdominant, this implies discarding much of the signal (Mao et al. 2012). Still, since this approach does not need any assumptions regarding the astrophysical processes it is the simplest and it can be used at all redshifts. Estimates show that it will be hard to extract cosmological information relying *only* on this effect (Mao et al. 2008). Additionally, the μ-decomposition may be affected by non-linearities in the velocity field (Shapiro et al. 2012b).
- **Simple Astrophysics**: Another avenue would be to analyze the full $P(k,\mu,z)$ at epochs where we expect the astrophysical contributions to be particularly simple. For example, if the radiative coupling and the heating

of the neutral IGM is efficient so that $T_S \gg T_{CMB}$ during most of the Cosmic Dawn (before any substantial reionization starts), then the 21cm signal would be just proportional to the DM field (Bowman et al. 2007). The challenge will be to identify the epoch when this happens, which in principle could be done by looking at the redshift evolution of large scale modes or the rms of the signal (Santos et al. 2011) as well as the global signal (Pritchard & Loeb 2008). This could be further confirmed by imaging a large patch where we do not find any obvious ionized regions, although there is always the danger of confusion with small fluctuations in the heating process or the ionization fraction.

- **Negligible Astrophysics**: An interesting approach, which needs to be further explored, is to look at very large scales (much larger than the typical "astrophysical scale", such as the size of ionized regions), so that we can use simple models for the astrophysical contribution. In this case we can in principle assume that the 21cm signal will be just a biased tracer of the underlying DM, thus making the cosmological analysis more straightforward. This was used in Joudaki et al. (2011) where it was shown that an SKA type experiment can constrain primordial non-Gaussianity at a level comparable to Planck, thus providing a crucial test of inflationary cosmology. It should also be possible to probe the Baryon Acoustic Oscillations, thus providing a standard ruler at an interesting time in the Universe evolution. Note however that a major design driver for this will be a large FoV (i.e. ~ 5 deg).
- **Modeling the Astrophysics**: The last possibility and the one which has to be used when one wants to analyze the full $P(k,\mu,z)$ at epochs of substantial reionization, is to try to fully model the astrophysical components of the 21cm signal, e.g. the ionization fraction and spin temperature fields (see Equation 1), to constrain the contribution from the underlying DM density field. This approach needs a full model of all contributions to the 21cm signal from either simple prescriptions of the ionization power spectrum and its cross-correlation with the density field (McQuinn et al. 2006; Bowman et al. 2007) or possibly from full simulations.

The analysis of redshift space distortions to date has concentrated on the effect of patchy reionization. However, SKA observations may provide measurements from periods in which fluctuations in the spin temperature dominate (Santos & Cooray 2006). This effect from peculiar velocities could then be used to separate the astrophysical contributions and provide extra information on the nature of the first objects emitting radiation (Barkana & Loeb 2005a; Santos et al. 2011).

3.6 The 21cm forest

An alternative to both the tomography technique from Section 3.2 and the power spectrum approach from Section 3.3 is to search for the 21cm forest, that is the 21cm absorption against high-z radio loud sources caused by the intervening cold neutral IGM and collapsed structures (e.g. Carilli et al. 2002; Furlanetto & Loeb 2002; Furlanetto 2006a; Carilli et al. 2007; Xu et al. 2009; Mack & Wyithe 2012; Xu et al. 2011). In fact the 21cm forest is more than a complement to tomography or power spectrum analysis. Since the strongest absorption features arise from small scale structures, the 21cm forest can probe the HI density power spectrum on small scales not amenable to measurements by any other means.

The photons emitted by a radio loud source at redshift z_s with frequencies $\nu > \nu_{21\mathrm{cm}}$, will be removed from the source spectrum with a probability $(1 - e^{-\tau_{21\mathrm{cm}}}$, see Equation 3), absorbed by the neutral hydrogen present along the LOS at redshift $z = \nu_{21\mathrm{cm}}/\nu(1+z_s) - 1$. Analogously to the case of the Ly-α forest, this could result in an average suppression of the source flux (produced by diffuse neutral hydrogen), as well as in a series of isolated absorption lines (produced by overdense clumps of neutral hydrogen), with the strongest absorption associated with high density, neutral and cold patches of gas.

This suggests that the absorption features due to collapsed structures, such as starless minihalos or dwarf galaxies (Furlanetto & Loeb 2002; Meiksin 2011; Xu et al. 2011) would be easier to detect than those due to the diffuse neutral IGM. However, this does strongly depend on the feedback effects acting on such objects. Because of the large uncertainties in the nature and intensity of high-z feedback effects (for a review see Ciardi & Ferrara 2005 and its updated version ArXiv:astro-ph/0409018), it is not straightforward to estimate the relative importance of the absorption signals from the diffuse IGM and from collapsed objects.

While gas which has been (even only partially) ionized has a temperature of $\sim 10^4$ K, gas which has not been reached by ionizing photons has a temperature which can be as low as that of the CMB. This neutral gas can be heated by Ly-α or X-ray photons, thus reducing the optical depth to 21cm. While Ly-α heating is not extremely efficient, heating due to X-ray photons could easily suppress the otherwise present absorption features (e.g. Mack

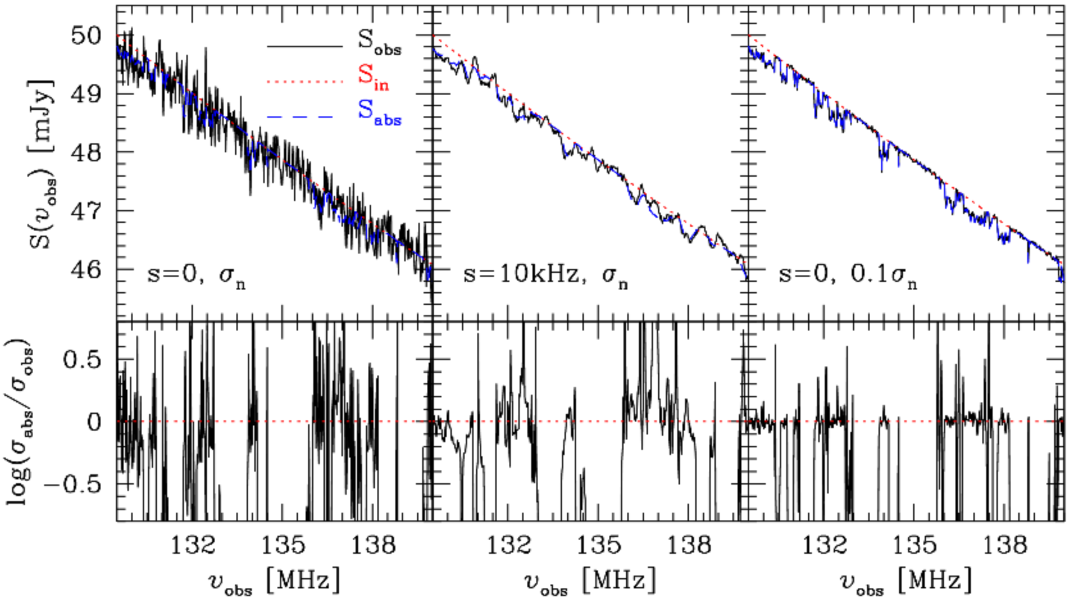

Fig. 7 *Upper panels:* Spectrum of a radio source positioned at $z = 10$ ($\nu \sim 129$ MHz), with a power-law index $\alpha = 1.05$ and a flux density $J = 50$ mJy. The red dotted lines refer to the instrinsic spectrum of the radio source, $S_{\rm in}$; the blue dashed lines to the simulated spectrum for 21cm absorption, $S_{\rm abs}$ (in a universe where neutral regions remain cold); and the black solid lines to the spectrum for 21cm absorption as it would be seen by LOFAR for an observation time $t_{\rm int} = 1000$ h and a frequency resolution $\Delta\nu = 20$ kHz. *Left upper panel*: $S_{\rm abs}$ and $S_{\rm obs}$ without any smoothing. *Middle upper panel*: $S_{\rm abs}$ and $S_{\rm obs}$ after smoothing over 10 kHz. *Right upper panel*: $S_{\rm abs}$ and $S_{\rm obs}$ without smoothing and with 1/10th of the LOFAR noise *Lower panels:* The ratio $\sigma_{\rm abs}/\sigma_{\rm obs}$ corresponding to the upper panels. Figure 10 from Ciardi et al. (2013).

& Wyithe 2012; Ciardi et al. 2013). This seems to suggest that observations of the 21cm forest would be possible to discriminate between different IGM reheating histories, in particular if a high energy component in the ionising spectrum was present.

The most challenging aspect of the detection of a 21cm forest remains the existence of high-z radio loud sources. Although a QSO has been detected at $z = 7.085$ (Mortlock et al. 2011), the existence of even higher redshift quasars is uncertain. The predicted number of radio sources which can be used for 21cm forest studies in the whole sky per unit redshift at $z = 10$ varies in the range $10 - 10^4$ depending on the model adopted for the luminosity function of such sources and the instrumental characteristics (e.g. Carilli et al. 2002; Xu et al. 2009), making such a detection an extremely challenging task. The possibility of using GRB afterglows has been suggested by Ioka & Mészáros (2005), concluding that it will be difficult to observe an absorption line, also with the SKA, except for very energetic sources, such as massive first stars. A similar calculation has been repeated more recently by Toma et al. (2011) for massive metal-free stars, finding that typically the flux at the same frequencies should be at least an order of magnitude higher than for a standard GRB.

Figure 7 shows the 21cm absorption spectrum due to the diffuse IGM for a bright radio source at $z = 10$ (i.e. $\nu \sim 129$ MHz). The intrinsic radio source spectrum, $S_{\rm in}$, is assumed to be similar to Cygnus A, with a power-law with index $\alpha = 1.05$ and a flux density $J = 50$ mJy. The simulated absorption spectrum, $S_{\rm abs}$, is calculated from a full 3D radiative transfer simulation of IGM reionization which resolves scales of ~ 15 kHz (Ciardi et al. 2012). In this simulation all reionization and heating is done by stellar spectra, leaving the neutral IGM in its cold state. The observed spectrum, $S_{\rm obs}$, is calculated assuming an observation time $t_{\rm int} = 1000$ h with the LOFAR telescope and a bandwidth $\Delta\nu = 20$ kHz. If the spectrum is smoothed over a scale $s = 10$ kHz (upper middle panel) or the noise is reduced by a factor of 0.1 similar to what is expected from the SKA (upper right panel) a clear absorption signal is observed. This is more evident in the lower panels of Figure 7, which show the quantity $\sigma_{\rm abs}/\sigma_{\rm obs}$, where $\sigma_i = S_i - S_{\rm in}$ and i=abs, obs.

As explained above, absorption features due to small collapsed objects can be much stronger than those due to the diffuse neutral IGM. Since their cross-sections are small, the best conditions for detecting them would be when Ly-α coupling pushes the spin temperature in their lower density outskirts to the gas temperature before these regions have been affected by any heating (see figure 22 in Meiksin 2011), conditions expected above $z \sim$

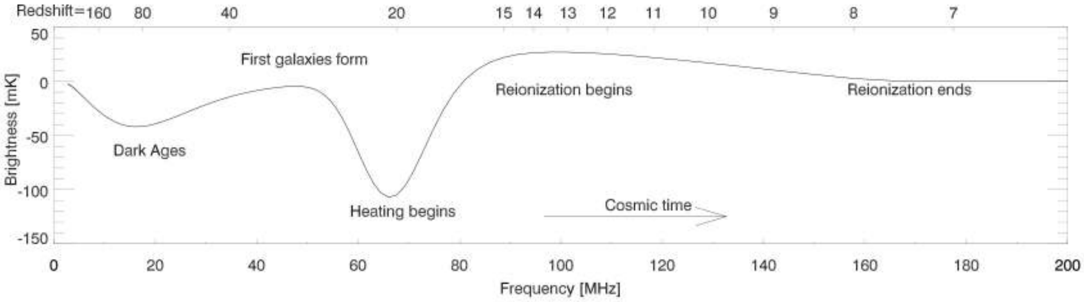

Fig. 8 Evolution of the global 21cm signal from the Dark Ages to the end of reionization. Figure 1 from Pritchard & Loeb (2012).

10. However, even after heating has started to suppress the 21cm absorption signal, some weak features due to collapsed structures may remain. Interestingly, even when it may not be possible to detect these weak features individually, they may be detected statistically through the excess brightness fluctuations they would produce over the telescope noise (see figure 29 in Meiksin 2011).

3.7 Global Signal

Tomography, power spectrum and 21cm forest measurements all give us information about 21cm fluctuations. Complementary to this would be measurements of the mean 21cm signal, referred to as the 'global signal' (Shaver et al. 1999; Furlanetto 2006b). This requires an absolute measurement of the 21cm brightness and can be considered to be the 21cm equivalent of the COBE/FIRAS black body measurement (Mather et al. 1990). In contrast, radio interferometers typically measure brightness fluctuations in the same way as WMAP observations of CMB anisotropies. Figure 8 shows the expected features in the global 21cm signal (Pritchard & Loeb 2010). At $\nu \sim 15$ MHz, during the dark ages, an absorption feature appears due to the collisional coupling to an unheated IGM that has been cooling adiabatically since recombination. This first absorption feature is determined by fundamental physics alone, but these low frequencies are unlikely to be accessible from the ground (Jester & Falcke 2009). The second absorption feature at $\nu \sim 60$ MHz occurs after star formation begins producing Ly-α photons, which couple spin and gas temperatures. Initially this leads to a deep absorption feature, but as sources of X-rays form and heat the IGM this absorption feature transitions into an emission feature. Progressive galaxy formation leads to ionizing UV photons that ionize the Universe and remove the 21cm signal altogether.

From this one-dimensional spectral measurement a few key pieces of information could be extracted. The positions of the various turning points would pin down the redshifts when the first galaxies and X-ray sources form and when reionization began and ended (Furlanetto 2006b; Pritchard & Loeb 2010). From this one could constrain the star formation rate, X-ray luminosity, and UV photon emissivity of early galaxies as a function of redshift. More detailed analysis of the 21cm signal might measure the thermal history of the IGM and so the presence of exotic heating sources (see Section 2.4).

Measuring the global signal can only be done using the auto-correlations of the SKA telescope, since a constant brightness temperature of HI provides no signal in the cross-correlation. We discuss this further in Section 5.3.1, in addition to its implications for SKA.

3.8 Connecting with other observables and telescopes

In this section we consider how combining SKA observations of the redshifted 21cm signal with other observations can teach us more about the Epoch of Reionization and the Cosmic Dawn.

3.8.1 Individual QSOs

The role of quasars during the EoR is a topic of debate. While they are generally believed to be important in heating the IGM (Zaroubi et al. 2007; Baek et al. 2010), it has been argued that the space density of quasars at high redshifts is too small to provide a significant contribution to the ionizing flux (Loeb 2009; Schmidt et al. 1995;

Boyle et al. 2000; Cristiani et al. 2004; González-Serrano et al. 2005). However, observations indicate that there may not be enough galaxies to fully ionize the universe (Bunker et al. 2010), and it has been claimed that quasars must play an important role after all, at least at lower redshifts (Volonteri & Gnedin 2009; Trac & Gnedin 2011).

Apart from the need to understand the role of quasars in ionizing the IGM, there are many unanswered questions regarding their intrinsic properties at high-redshift. The observation of QSO's with a central black hole mass of $\sim 10^9$ M$_\odot$ already at redshifts $6.5 < z < 7.0$ (Fan et al. 2006; Mortlock et al. 2011) raises questions about the formation and growth scenarios for supermassive black holes.

With the SKA we will be able to follow up quasars found with optical and near-IR data and study many of the unanswered questions above. Among other things, we would be able to study the properties of these quasars including how many are active, their lifetime and to what extent they contribute to the ionization of the IGM by studying their HII regions. Obscured (e.g. type-II) quasars, however, are harder to find and might require X-ray surveys or detection with SKA itself (e.g. very-steep-spectrum radio sources tend to be at higher redshifts).

The main near-IR surveys in the advent of the SKA are those with the VISTA telescope and with the future Euclid satellite. By extrapolating measurements of the luminosity function of quasars at redshift $z \sim 6$, Willott et al. (2010) estimated number densities out to $z = 9$. Uncertainties, especially when it comes to the knee of the mass function, could imply smaller number densities for the wider surveys as there is a minimum amount of time required for these sources to assemble.

However, from these extrapolations, one finds that VISTA related surveys such as VIKING (1500 sq deg to $H = 19.9$), VIDEO (15 sq deg to $H = 23.7$) and UltraVISTA (0.73 sq deg to 25.4) should all find several quasars at $6.5 < z < 7.5$ and a few at $7.5 < z < 8.5$. Euclid will have two surveys: a shallow (15000 sq deg to $H = 24$) and a deep survey (40 sq deg to $H = 26$). The wide survey should be able to detect around 1 quasar per 20 sq deg at $z \sim 7$, 1 quasar per 50 sq deg at $z \sim 8$ and 1 quasar per 200 sq deg at $z \sim 9$.

Analysis of the spectra of optically detected high redshift QSOs reveal that large HII regions (10 -100 cMpc in radius Fan et al. 2006; Carilli et al. 2010) are associated with these objects. Targeted observations of HII regions around known luminous QSOs will provide unique and more detailed information about their size and shape (Wyithe et al. 2005; Datta et al. 2008; Majumdar et al. 2011; Datta et al. 2012a). The anisotropy in the HII region shape which may arise due the rapidly expanding ionization font (Shapiro et al. 2006) and finite light travel time (Wyithe et al. 2005; Yu 2005; Majumdar et al. 2011) can also be probed with SKA. This information can further be used to calculate the QSO luminosity and age with higher accuracy, providing crucial parameters for understanding the formation of SMBHs during the EoR (Datta et al. 2012a; Majumdar et al. 2012). In addition, measurements of the contrast in 21cm emission between HII regions and the surrounding regions will provide measurements of the hydrogen neutral fraction of the outside IGM (Geil & Wyithe 2008). These measurements will be complementary to power spectrum measurements. Identification of large HII regions in the SKA 21cm tomography can guide a search for bright QSOs and galaxies in the middle of these regions (Wyithe et al. 2005; Datta et al. 2012a).

3.8.2 Galaxy surveys

To alleviate some of the problems associated to observations of the weak 21cm signal, several cross-correlation analyses with observations in other frequency windows have been proposed. The idea is that the noise/systematics in two observations of different frequency and strategy might cancel out. An exciting possibility would be a cross-correlation with galaxy surveys (Lidz et al. 2009; Wiersma et al. 2012). Even if SKA may have a high enough sensitivity not to need cross-correlation techniques in order to detect the signal, cross-correlating with other probes will improve our understanding of the process of reionization. In the case of galaxies, it will specifically help in answering the question which types of galaxies are mostly responsible for reionization.

Following Lidz et al. (2009) one can define the cross power spectrum between the 21cm emission and the galaxies as:

$$\begin{aligned} \Delta^2_{21,\mathrm{gal}}(k) &= \tilde{\Delta}^2_{21,\mathrm{gal}}(k)/\delta T_{b0} \\ &= x_{\mathrm{HI}}\left[\Delta^2_{x_{\mathrm{HI}},\mathrm{gal}}(k) + \Delta^2_{\rho,\mathrm{gal}}(k)\right. \\ &\qquad \left. + \Delta^2_{\rho x_{\mathrm{HI}},\mathrm{gal}}(k)\right], \end{aligned} \tag{8}$$

where δT_{b0} is the 21cm brightness temperature relative to the CMB for neutral gas at the mean density of the universe, x_{HI} is the neutral fraction and $\Delta^2_{a,b}(k)$ is the dimensionless cross power spectrum between fields a and b. In order to construct the cross power spectrum, one therefore requires three fields, the density field, ρ, the neutral

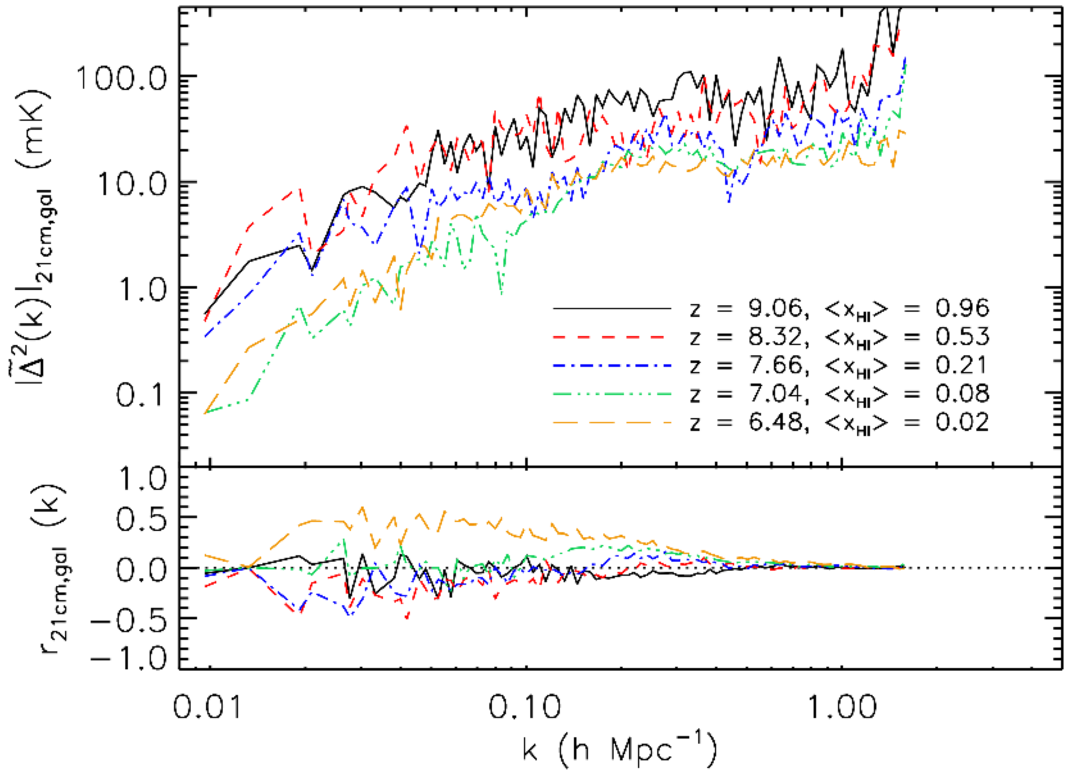

Fig. 9 The circularly averaged, unnormalized 2D 21cm – galaxy cross power spectrum ($\tilde{\Delta}^2_{21,\mathrm{gal}}(k)$; upper panel) and correlation coefficient (lower panel) for various redshifts/mean neutral fractions for a Ly-α Emitters survey. Figure 10 from Wiersma et al. (2012).

hydrogen field, x_{HI}, and the galaxy field, gal, which can be obtained via numerical simulations of galaxy formation and the reionization process.

It is found that the 21cm emission is initially correlated with galaxies on large scales, anti-correlated on medium, and uncorrelated on small scales. This picture quickly changes as reionization proceeds and the two fields become anti-correlated on large scales. These (anti-)correlations can be a powerful tool in indicating the topology of reionization and should form important diagnostic tools for SKA observations.

If the effect of observing and selecting real galaxies is taken into account, the result depends on the observational campaign considered. For example, for a drop-out technique (as in observations of Lyman Break Galaxies), the normalization of the cross power spectrum seems to be the most powerful tool for probing reionization. In particular, it is quite sensitive to the ionized fraction as different reionization histories yield similar cross power spectra for a fixed ionized fraction. When instead a more precise measurement of the galaxy redshifts is available (as in Ly-α Emitters surveys) and so the three-dimensional position of the galaxy is known, much more information about the nature of reionization can be extracted, as both the shape and the normalization of the cross power spectrum provide useful information. In addition, the observability of the Ly-α line from these galaxies is affected by neutral patches in the IGM and thus Ly-α Emitters surveys are particularly useful for EoR studies (McQuinn et al. 2007a; Jensen et al. 2013)

Figure 9 shows the 21cm - Ly-α Emitters cross power spectrum and correlation coefficient for a number of redshifts. Here the noise assigned to the 21cm survey is the one of the LOFAR telescope, while the Ly-α Emitters survey has the same characteristics of the one described in Ouchi et al. (2010) with the Subaru telescope. The effect of neutral patches in the IGM on the observability of these Ly-α Emitters is not included here.

3.8.3 Background radiation surveys

Apart from surveys of individual objects described above, there are also surveys of background radiation which can be correlated with the 21cm signal. Of these the near-infrared background (NIRB), X-ray background (XRB) and the backgrounds from redshifted molecular lines, are all associated with structures from the periods that SKA

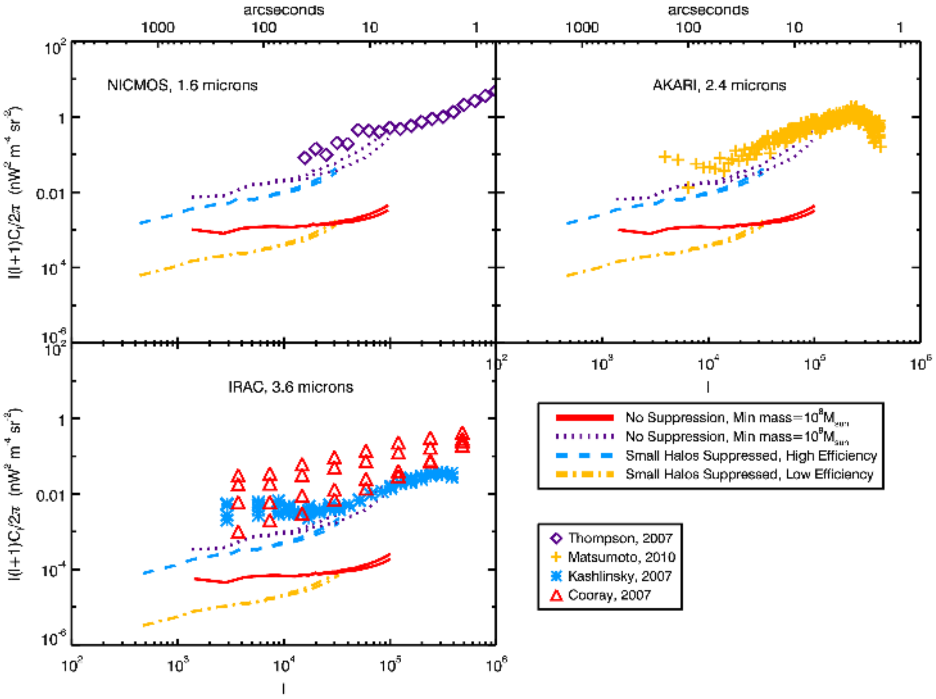

Fig. 10 NIRB sky power spectrum signals calculated theoretically, based on different simulations of the galaxy distribution and reionization patchiness, compared to observational results at 1.6 μm from the NICMOS camera, 2.4 μm from AKARI, and 3.6 μm from IRAC, as labelled. Figure 4 from Fernandez et al. (2012).

can study. The Cosmic Microwave Background (CMB) dates of course from the Epoch of Recombination, but the EoR is expected to leave its imprint on it.

The cross-correlation of the 21cm signal with the XRB appears not have been studied in any detail and we do not discuss it here.

- **Near Infrared Background**
  In the near-infrared spectral region of 1 to 5 μm, the sky shows a faint excess emission of extragalactic origin. Although expected and searched for since at least the 1960s (see Hauser & Dwek 2001, for a review), it was first measured in this wavelength range in the year 2000 by a combination of IRTS and COBE data (Gorjian et al. 2000; Matsumoto et al. 2000; Wright & Reese 2000). Such measurements are difficult due to the presence of the strong interplanetary zodaical light but seem to indicate a flux level of $\nu I_\nu \sim 10$ nW m^{-2} sr^{-1} above what is expected from the known galaxy population. Measurements of the fluctuation power spectrum at different wavelengths appear to be much less affected by zodaical light and yield fluctuation levels of ≈ 0.1 nW m^{-2} sr^{-1} (Kashlinsky et al. 2005, 2012 at 3.6, 4.5, 5, 8.8 μm with Spitzer; Matsumoto et al. 2011 at 2.4, 3.1 μm with AKARI; Thompson et al. 2007 at 1.1 and 1.6 μm with NICMSOS/HST).
  Theoretically, the most exciting interpretation of the NIRB is that it originates from the many small and faint galaxies at $z > 6$, some of which could still have massive metal-free (PopIII) stars (see e.g. Santos et al. 2002; Salvaterra & Ferrara 2003). Small galaxies are thought to dominate the ionizing photon budget during the EoR, but are as yet undetected in the deepest current surveys. If true, the NIRB would be an exquisite tool to study high-z galaxies and reionization as it would probe all sources rather than only the brightest ones. Models for example indicate that the power spectrum of fluctuations could distinguish between populations of galaxies with different clustering properties (see Figure 10 and Fernandez et al. 2010, 2012; Cooray et al. 2012a; Yue et al. 2013).
  However, the measured intensity of the NIRB is found to be ~ 10 times larger than both theoretically and observationally can be accommodated for by stars during reionization (Madau & Silk 2005; Salvaterra & Ferrara 2006) and also the predictions for the amplitude of fluctuations are typically below the measured data points (Cooray et al. 2012a; Yue et al. 2013). This indicates that our understanding of this background radiation remains incomplete and that in addition to the contribution from faint high-z galaxies, another yet unknown

foreground must dominate the observed NIRB. Cooray et al. (2012b) recently proposed that this foreground is composed of the diffuse light of intra-halo stars at intermediate redshifts ($z \sim 1$ to 4). However, the fact that the unknown component appears to have a clustering signal very similar to that of the EoR galaxies, is rather puzzling but may indicate that it arises from associated phenomena such as the gravitational energy release from quasar-like sources (Yue et al. 2013).

Cross-correlating NIRB fields with 21cm measurements could give a clear signal if the NIRB has a substantial contribution from the EoR. One should however keep in mind that the NIRB signal comes from a wide range of redshifts and does not carry precise redshift information, which will weaken the correlation signal at any given frequency. A theoretical investigation of the expected correlation signal would be useful to make firmer statements on how strong a signal can be expected. Still, a NIRB-21cm cross-correlation study should in principle be able to show whether the NIRB mostly originates from the EoR, thus solving the enigma of its origin. If it does, it would allow us to make statements about the clustering of the faint galaxy population most likely responsible for the reionization process and thus improve our understanding of the physics of the EoR. The use of large fields ($> 1^\circ$) is required to prevent the faint low-z sources present in the NIRB data to influence the result.

- **Cross-correlation with Intensity Mapping of Molecular and Fine Structure Lines**
  The NIRB provides a signal integrated over many redshifts units. An interesting alternative is the background caused by molecular and fine structure lines. These lines are generated in star forming galaxies and thus trace the star formation history. The two main species that have been considered are CO and CII. Even if experiments targetting CII or CO lines do not have the necessary sensitivity and resolution to probe individual galaxies during this epoch, the brightness variations of the line intensity can be used to map the underlying distribution of galaxies and DM (Basu et al. 2004; Visbal & Loeb 2010). Recently it has been proposed to use rotational lines of CO molecules to probe reionization (e.g., Gong et al. 2011; Carilli 2011; Lidz et al. 2011) showing that a measurement of the cross-correlation should be achievable even for LOFAR (Gong et al. 2011). The CII line on the other hand is generally the brightest emission line in star-forming galaxy spectra contributing to about 0.1% to 1% of the total far-infrared luminosity and will probe the onset of star formation and metal production in $z \sim 6-8$ galaxies. Gong et al. (2012) analysed the possibility of intensity mapping using this line, showing that a cross-correlation with results from an SKA phase 1 experiment should generate a high signal to noise (Figure 11). Such a detection will provide statistical information on the typical bubble size (when the correlation changes from negative to positive) and thus probe the astrophysical processes ocurring inside the ionized bubbles at a statistical level.
- **Cosmic Microwave Background**
  One of the leading sources of secondary anisotropies in the CMB is due to the scattering of CMB photons off free electrons (Zeldovich & Sunyaev 1969). The effect of anisotropies when induced by thermal motions of free electrons is called the thermal Sunyaev-Zel'dovich effect (tSZ) and when due to bulk motion of free electrons, the kinetic Sunyaev-Zel'dovich effect (kSZ). The latter is far more dominant during reionization (for a review of secondary CMB anisotropies see, e.g. Aghanim et al. 2008).

  The kSZ effect from a homogeneously ionized medium, i.e., with ionized fraction only a function of redshift, has been studied both analytically and numerically by a number of authors; the linear regime of this effect was first calculated by Sunyaev & Zeldovich (1970) and subsequently revisited by Ostriker & Vishniac (1986) and Vishniac (1987) – hence also referred to as the Ostriker-Vishniac (OV) effect. In recent years various groups have calculated this effect in its non-linear regime using semi-analytical models and numerical simulations (Gnedin & Jaffe 2001; Santos et al. 2003; Zhang et al. 2004). These studies show that the contributions from non-linear effects are only important at small angular scales ($l > 1000$), while the OV effect dominates at larger angular scales.

  The kSZ effect from patchy reionization was first estimated using simplified semi-analytical models by Santos et al. (2003) who concluded that it dominates over that of a homogeneously ionized medium. More detailed modeling of the effect of patchy reionization were subsequently performed using numerical simulations (Salvaterra et al. 2005; Iliev et al. 2007) and semi-analytical models (McQuinn et al. 2005; Zahn et al. 2005; Mesinger et al. 2012). Doré et al. (2007) used numerical simulations to derive the expected CMB polarization signals due to EoR patchiness. The CMB bolometric arrays Atacama Cosmology Telescope (ACT, Fowler et al. 2010) and South Pole Telescope (SPT, Shirokoff et al. 2011) are currently being used to measure the CMB anisotropies at the scales relevant to reionization ($3000 < \ell < 8000$). The SPT results are starting to put limits on the duration of reionization (Zahn et al. 2012).

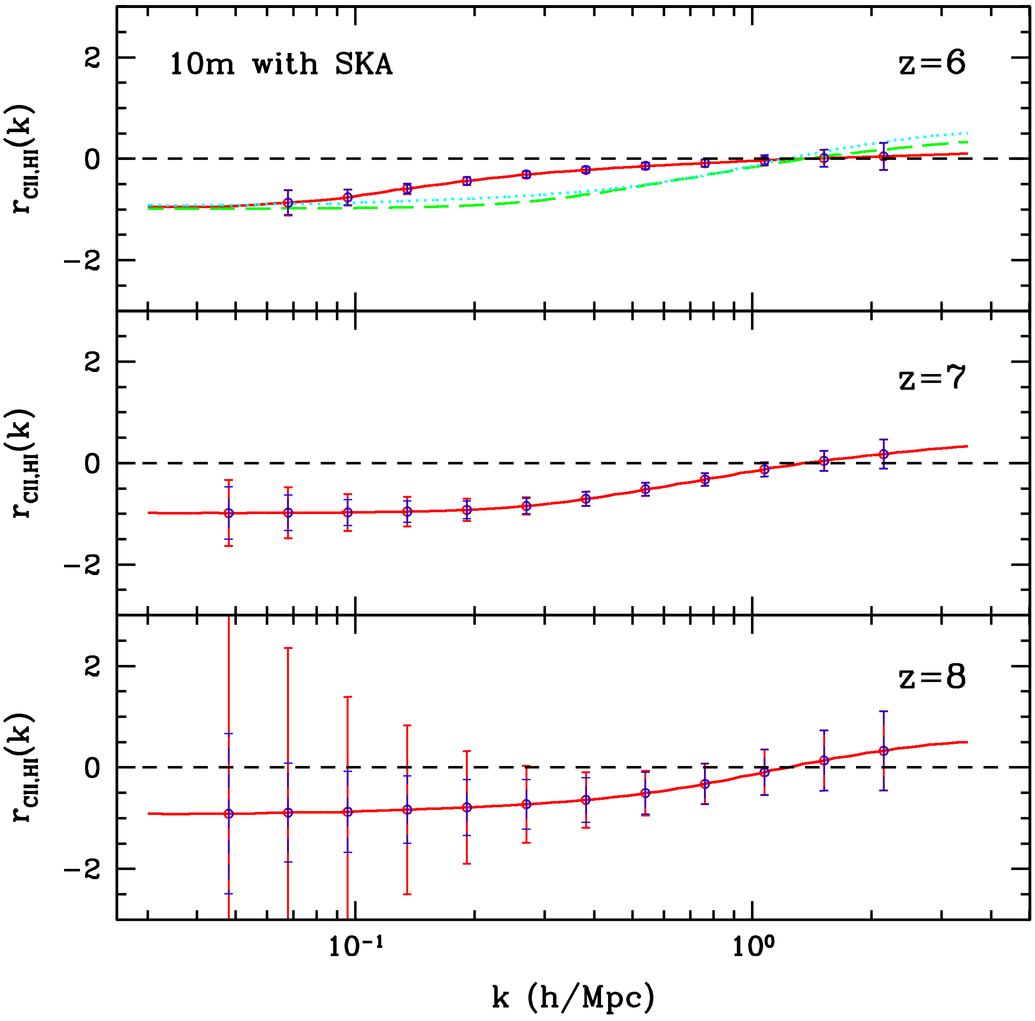

Fig. 11 The cross-correlation coefficient $r(k)$ of the CII (with 10 m dish) and 21cm emission (with SKA) at $z=6$, $z=7$ and $z=8$. The error bars of r are also shown (red solid), and the blue dashed ones are the contribution from the 21cm emission. We find the 21cm noise dominates the errors at $z=6$ and 7. In the top panel, the $r_{\rm CII,HI}(k)$ at $z=7$ (green dashed) and $z=8$ (cyan dotted) are also shown to illustrate the evolution of the ionized bubble size at these redshifts relative to $z=6$. Figure 13 from Gong et al. (2012)

Cross-correlation between the cosmological 21cm signal, as measured with SKA, and the secondary CMB anisotropies provide a potentially useful statistic. As in the cases described above, the cross-correlation has the advantage that the measured statistic is less sensitive to contaminants such as the foregrounds, systematics and noise in comparison to "auto-correlation" studies.

Analytical cross-correlation studies between the CMB temperature anisotropies and the EoR signal on large scales ($l \sim 100$) were carried out by Alvarez et al. (2006); Adshead & Furlanetto (2008); Lee (2009) and on small scales ($l > 1000$) by Cooray (2004), Salvaterra et al. (2005), Slosar et al. (2007) Tashiro et al. (2008) and Tashiro et al. (2011). Cross-correlation between the E- and B-modes of CMB polarization with the redshifted 21cm signal was done by Tashiro et al. (2008) and Dvorkin et al. (2009). Numerical studies of the cross-correlation were carried out by Salvaterra et al. (2005) and Jelić et al. (2010b).

These studies showed that the kSZ and the redshifted 21cm signal: (i) anti-correlate on the scales corresponding to the typical size of ionized bubbles; and (ii) correlate on the larger scales, where the patchiness of the ionization bubbles are averaged out (see Fig. 12). The significance of the anti-correlation signal depends on the reionization scenario (Salvaterra et al. 2005; Jelić et al. 2010b; Tashiro et al. 2011).

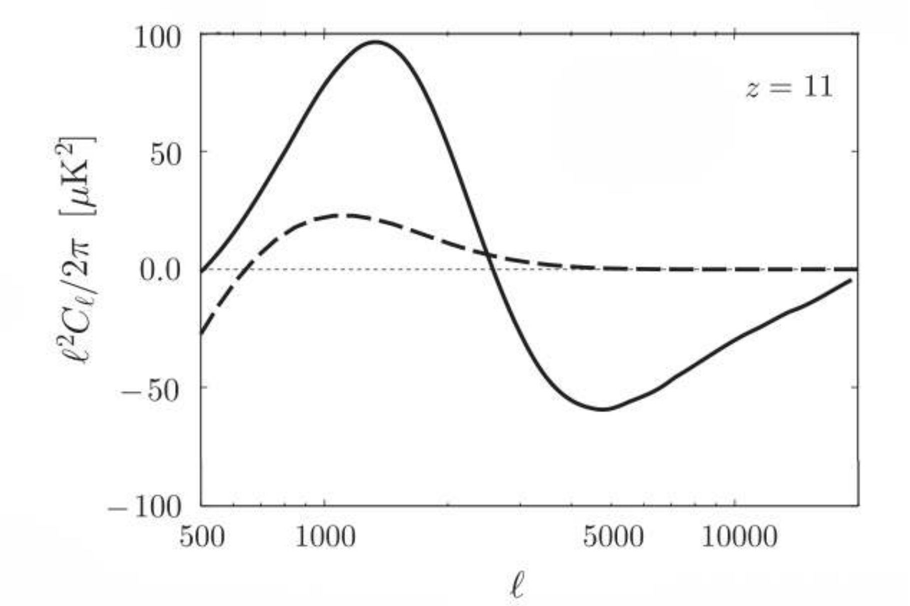

Fig. 12 An example of the cross-power spectrum of the kSZ and the cosmological 21cm signal at $z = 11$. The solid line is for a 'patchy' reionization history, while the dashed line is for a 'homogenous' history. Figure 3 (middle panel) from Tashiro et al. (2011).

Unfortunately, the cross-correlation signal turns out to be difficult to detect, even in radical reionization cases, assuming typical SKA and Planck characteristics (Tashiro et al. 2008, 2011). However, the kSZ signal induced during the EoR could possibly be detected in the power spectra of the CMB and used to place some additional constraints on this epoch in the history of our Universe.

4 Observational Challenges & Strategies

In this section we outline some of the important issues to consider when designing a CD/EoR observational strategy and basic design reference for SKA-low.

4.1 Fields size: sample variance and discovery space

The optimal observational field sizes and locations will be determined by a number of competing requirements, both scientific and technical. While in general it would be desirable to maximize the size of fields in order to obtain better statistics, there is a trade off between the field size and the array design: (1) Large FoV requires small station sizes, which for a fixed collecting area means a large number of stations and hence a high computing cost for correlation. We therefore need to identify the minimum requirements for the SKA survey field to achieve the desired EoR science goals. (2) Furthermore, given a finite sky coverage, the question is where this coverage should be placed to gain maximum synergy with other surveys, while at the same time maximizing the conditions for good quality data.

The main requirement for survey size is the desire to observe a representative sample of the Universe. This is important for minimizing sample variance (occasionally equated to cosmic variance in the literature) in statistical measurements of the power spectrum (see also Section 5). Crudely the number of modes with wavenumber k that fit into a survey volume V is given by $N_k = 4\pi\varepsilon k^3 V/(2\pi)^3$, for logarithmic bins of $\Delta k = \varepsilon k$ and the uncertainty in the power spectrum from the sample variance around redshift $z \approx 10$ is

$$\Delta P/P = 2/\sqrt{N_k} \approx 0.01 \left(\frac{k}{0.1\,\mathrm{Mpc}^{-1}}\right)^{-3/2} \left(\frac{V}{1\,\mathrm{Gpc}^3}\right)^{-1/2} \left(\frac{\varepsilon}{0.5}\right)^{-1/2}. \tag{9}$$

Thus, assuming $\varepsilon = 0.5$ a volume of 1 Gpc^3 is required to reduce sample variance to the 1% level on scales $\sim 0.1\,\mathrm{Mpc}^{-1}$ where the EoR signal is likely to be greatest. In Section 5.2.1 we further discuss the requirements for power-spectrum determinations, considering both noise and sample variance.

A rough scaling relation for the comoving volume of a cylindrical survey, accurate to ~ 10% over the relevant redshift range for CD/EoR observations ($z \approx 6-30$), is

$$V_{\rm survey} \approx 0.1\,\mathrm{Gpc}^3 \left(\frac{\theta}{5^\circ}\right)^2 \left(\frac{B}{12\,\mathrm{MHz}}\right) \left[(1+z)^{1/2}-2\right]. \tag{10}$$

We note that multi-beaming is not included in this volume calculation. The redshift dependence is relatively weak, about a factor of three over the full redshift range, but is the main source of the fit error here. A field of view of 5° across corresponds to a transverse comoving distance of ~ 1 Gpc, while 10 MHz gives a line of sight comoving depth of ~0.2 Gpc. The take away point of this back of the envelope calculation is that fields 5° across are sufficient to allow for sample variance limited errors of ~ 3% on the scales of greatest interest for the 21-cm power spectrum. To go to ~1% sample variance errors requires 10 such beams either through multi-beaming (see also Section 5.3) or sequentially.

A further important point is that although the line of sight direction can be well sampled to measure small-scale fluctuations, the largest scales we can extract are limited by the light cone effect (Section 3.5). Above which scale this becomes important depends on how fast structures evolve. Simulations suggest that in the worst case modes below $k \sim 0.1$ Mpc^{-1} are affected (Datta et al. 2012b). The frequency direction is further restricted by limitations in the foreground removal, which removes large scale modes. For the largest wavelength modes (small k values) all sensitivity thus has to come from the angular modes on the sky.

Another important requirement is that the observational volume needs to be considerably larger than the characteristic scale of ionized regions during reionization and of heated regions during the cosmic dawn. Theoretical studies and simulations show that ionized bubbles have characteristic sizes in the range 1-20 cMpc during reionization, corresponding to angular scales from below an arcminute up to ~ 10 arcminutes. This is illustrated in Figure 13, which shows the ionization, density, 21 cm signal, and galaxy distributions through a slice of a numerical simulation. These panels are 4° across at $z = 7.5$ and 6.8 and give an indication of the structures that SKA would image. The larger patterns in ionized regions correspond to scales of $\sim 120/h$ cMpc which corresponds to angular scales of ~ 1° (see e.g. Zaroubi et al. 2012). Again, there is a clear requirement for SKA fields that are several degrees across to provide a representative sampling of the ionized structures (see also Section 5.3). Large fields further maximize the possibility of serendipitous discovery of rare objects, for example, radio bright high redshift objects, within the main survey volume.

The field of view of the SKA affects imaging and power spectrum measurements differently. For power spectrum measurements it is important that an individual pointing contains all relevant k modes, so that the smallest k mode is fixed by the instantaneous field of view. Although it might be possible to produce a mosaic using multi-beaming, this is unlikely to accurately reconstruct modes with wavelengths longer than the size of an individual field. For imaging measurements, which operate in real space, different pointings could be used to stitch together a larger field. In imaging, we will typically be interested in counted statistics - the numbers and sizes of bubbles measured from individual images. In this sense, imaging studies have much in common with traditional galaxy surveys. As a consequence, the field of view requirements for imaging are likely to be less strict than for statistical measurements. Zaroubi et al. (2012) argue that since the density fluctuation power spectrum peaks at scales of $120h^{-1}$ cMpc (~ 1°) this will be roughly the scale of the ionized and neutral regions at the midpoint of reionization. Reionization simulations of a $425h^{-1}$ cMpc volume confirm this (Iliev & Mellema, private communication), see Figure 13. To properly capture this scale, an image size of *at least* ~ 2° should be aimed for. To summarize, a FoV ~ 2° across might be sufficient for imaging, but the larger FoV ~ 5° will be vital for power spectrum studies. We will discuss the implications for the design of SKA-low in Section 5.

Having argued for the need for fields that are at least ~ 5° in size, we turn to the question of where these fields should be located on the sky. For EoR searches, the key consideration is to minimize Galactic radio foreground emission making fields at high Galactic latitude desirable. Figure 14 shows the radio sky with the regions observable from MWA and LOFAR sites. Being located at the same site, the SKA-low sky is the same as that for MWA. Hopefully results from MWA and the South Africa-based PAPER will help in identifying the best fields with minimal galactic foreground emission and polarization.

Beyond minimizing foregrounds, it will be important to ensure the SKA fields overlap with other astronomical surveys. By 2025, many different galaxy surveys will have surveyed $\gtrsim 10,000$ deg^2 regions of the sky to differing

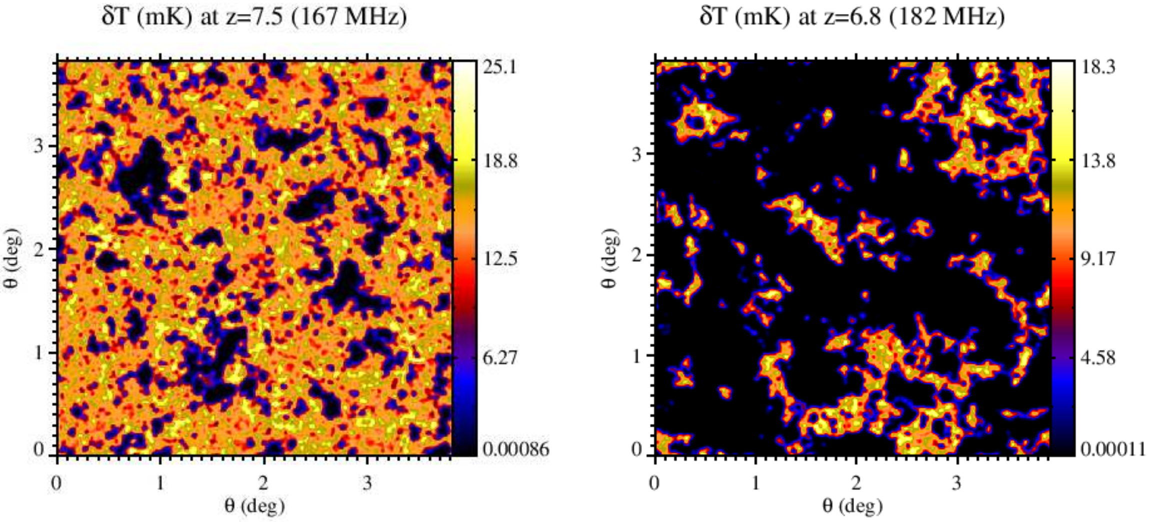

Fig. 13 Simulated maps of 21cm signal at two different redshifts. Each map is 425 cMpc/h on a side (corresponding to $\sim 4°$). The two images are drawn from the full cube at $z = 7.5$ (left, mean ionized fraction $x_{i,M} = 0.5$) and $z = 6.8$ (right, $x_{i,M} = 0.8$). The results have been smoothed with a Gaussian beam of $2'$ and a freqency bandwidth of 0.3 MHz. It can be seen that typical structures are captured at scales of 1–2°. Courtesy of G. Mellema and I. T. Iliev. More details about this simulation can be found in Shapiro et al. (2012a).

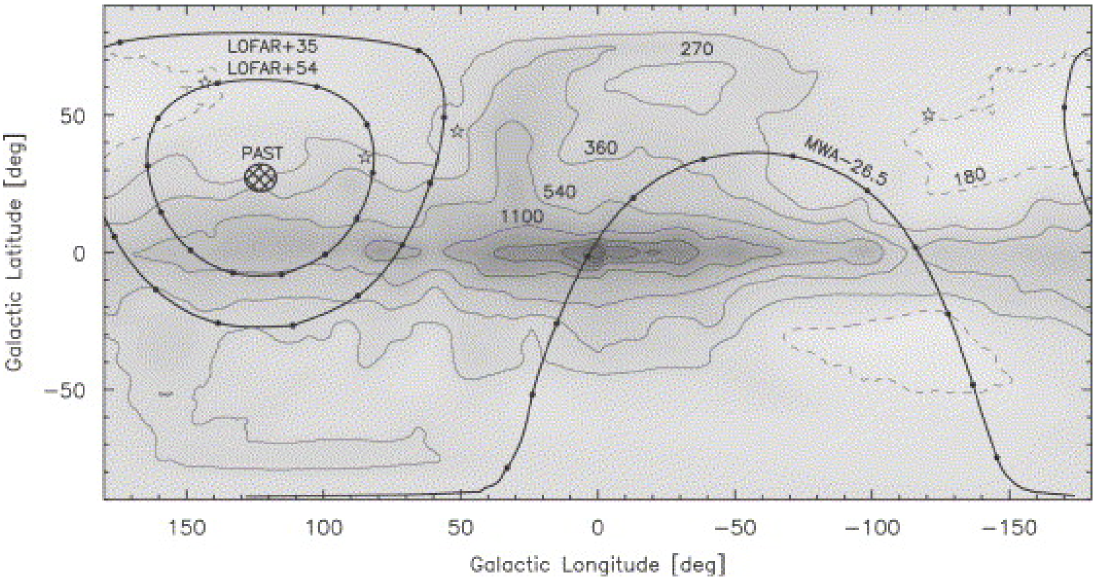

Fig. 14 Brightness temperature of the radio sky at 150 MHz (from Landecker & Wielebinski 1970) in Galactic coordinates. Contours are drawn at 180 (dashed), 270, 360, 540, 1100, 2200, 3300, 4400, and 5500 K. The north celestial pole area is cross-hatched. Heavy lines indicate constant declinations:-26.5°, +35°, and +54° with dots to mark 2h intervals of time. Star symbols indicate the coordinates of the four highest redshift ($z > 6.2$) SDSS quasars (found with the NASA Extragalactic Database, nedwww.ipac.caltech.edu). Figure 25 from Furlanetto et al. (2006a).

depths in optical and NIR bands. While the majority of these surveys are targeted at galaxies $z \lesssim 3$ the availability of optical/IR photometry on SKA fields will be important for the identification of radio bright high-z quasars for 21 cm forest studies (Section 3.6). Ground based surveys include BOSS (10,000 deg^2 - $\sim$ 7500 Northern Galactic Cap (NGC) remainder SGC (Eisenstein et al. 2011)) and VISTA. On a similar timescale to SKA, ESA will fly Euclid, which is perhaps the key survey instrument of comparable performance to SKA. Euclid will focus on areas $|b| > 30°$ (see Laureijs et al. (2011), section 5.2.3), making this a desirable location for SKA fields.

For direct correlation with SKA 21-cm maps, galaxies at $z \gtrsim 6$ are required and these are likely to be found as Lyman alpha emitters. The premier instrument for wide and deep field searches over the next decade will be the Hypersuprime Camera (HSC) on Subaru in Hawaii which was installed in August 2012. HSC has a $90'$ diameter FoV with a preliminary survey suggested as a layer cake with 300 $\deg^2$ shallow and 20 $\deg^2$ deep components. Overlap with the HSC deep field would be critical for LAE-21cm cross-correlation studies (Section 3.8.2).

In addition to all sky CMB surveys such as Planck there are a number of current small scale CMB experiments, such as SPT (Schaffer et al. 2011) and ACT (Dunkley et al. 2011), which are targeting the SZ signal in fields over $\sim 1000\,\deg^2$. The possibility of detecting the kSZ-21 cm cross-correlation has been discussed in Section 3.8.3. SPT and ACT are located at the South Pole and Chile respectively and so have fields accessible from the SKA site. Overlap of the SKA field with these CMB fields would allow for cross-correlation searches.

The final choice of SKA observing fields will depend primarily upon the radio sky, but also upon the ability to maximize coverage by other wavelength surveys as mentioned above. Deep and wide follow up observations with targeted facilities at other wavelengths will also be useful, for example with ALMA, TMT/GMT/E-ELT, and JWST. These instruments will all have coverage of the sky accessible to SKA from the southern hemisphere and so should place few constraints upon the choice of SKA field.

4.2 Foregrounds

In the frequency range of the CD/EoR experiments (say 40–240MHz; see Section 5.1) the foreground emission of our Galaxy and extragalactic sources (e.g. radio galaxies and clusters) dominate the sky. The amplitude of this foreground emission is $4-5$ orders of magnitude stronger than the expected cosmological 21 cm signal. However, given that the radio telescopes which are used for the EoR observations are interferometers and hence measure only fluctuations on given angular scales, the ratio between the measured foregrounds and the cosmological signal is reduced, typically to $2-3$ orders of magnitude (e.g. Bernardi et al. 2009, 2010).

In terms of physics, the foreground emission originates mostly from the interaction between relativistic charged particles and magnetic fields, i.e. synchrotron radiation. Galactic synchrotron radiation is the most prominent foreground emission and contributes about 70% to the total emission at 150 MHz (Shaver et al. 1999). The contribution from the extragalactic synchrotron radiation from mostly compact sources is $\sim 27\%$, while the smallest contribution ($\sim 1\%$) is from Galactic free-free emission, i.e. thermal emission of ionized gas.

The foreground emission is poorly constrained. The only all-sky map in the frequency range relevant for the EoR experiments is the 150 MHz map by Landecker & Wielebinski (1970), which a coarse, 5° resolution. The source counts from 3CRR catalog at 178 MHz (Laing et al. 1983) and 6C survey at 151 MHz (Hales et al. 1988) are too shallow for the deep EoR observations. Hence, in the last decade there has been a slew of the observational and theoretical efforts to constrain and explore the foreground emission.

Observations with the Giant Meter Radio Telescope (GMRT) have characterized the visibility correlation function of the foregrounds (Ali et al. 2008) and have set an upper limit to the diffuse polarized Galactic emission (Pen et al. 2009). Rogers & Bowman (2008) estimated the spectral index of the diffuse radio background between 100 and 200 MHz using the EDGES (Experiment to Detect the Global EOR Signature) antenna. The most recent and comprehensive targeted observations of the foregrounds have been done by the LOFAR-EoR team, using the Westerbork Radio Synthesis Telescope (WSRT; Bernardi et al. 2009, 2010) and the Low Frequency Array (LOFAR; Jelic et al., Labropoulos et al., and Yattawata et al., in preparation). These observations indicate that Galactic emission seems to be less prominent than expected by extrapolating from the higher frequency observations.

Foreground models capable of simulating maps of the foreground emission on arc minute scales in the frequency range of the EoR experiments are diverse. Jelić et al. (2008) made a first foreground model that includes both Galactic and extragalactic components of the foreground emission (see Figure 15). de Oliveira-Costa et al. (2008) used all publicly available total power radio surveys to obtain all-sky Galactic maps at the desired frequency range. More detailed simulations of Galactic emission were developed by Sun et al. (2008); Waelkens et al. (2009); Sun & Reich (2009); Jelić et al. (2010a), while maps of the extragalactic emission were developed by Jackson (2005); Wilman et al. (2008).

4.2.1 Removal

Once a well-calibrated data set cleaned of corrupting influences (i.e. interference, ionosphere, beam, etc.) has been obtained, the remaining major challenge will be the separation of the EoR signal from the astrophysical

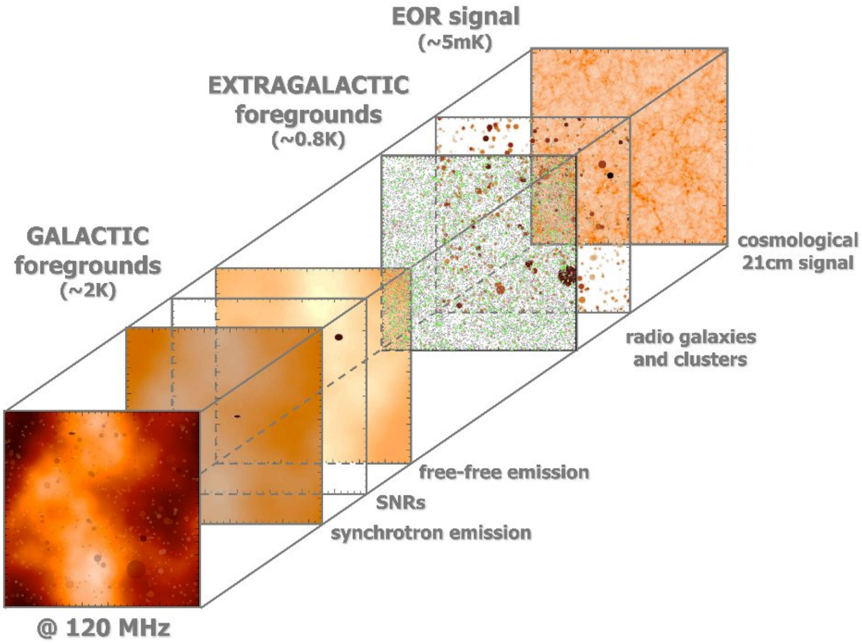

Fig. 15 Illustration of the various simulated Galactic and extragalactic foregrounds for the redshifted 21 cm radiation from the EoR. Courtesy from V. Jelić.

foregrounds. Foreground removal is generally considered to be a three stage process: bright source removal (e.g., Di Matteo et al. 2004; Pindor et al. 2011; Bernardi et al. 2011), spectral fitting (e.g., Shaver et al. 1999; Santos et al. 2005; Wang et al. 2006; McQuinn et al. 2006; Bowman et al. 2006; Jelić et al. 2008; Harker et al. 2009a, 2010; Petrovic & Oh 2011; Trott et al. 2012), and residual error subtraction (Morales & Hewitt 2004) though efforts have been made to merge these steps (Gleser et al. 2008; Mao 2012; Petrovic & Oh 2011).

The foreground fitting is usually done in total intensity along frequency, since: (i) the cosmological 21 cm signal is essentially unpolarized and fluctuates along frequency; and (ii) the foregrounds are smooth along frequency in total intensity and might show fluctuations in polarized intensity (see Figure 16). Thus, the EoR signal can be extracted by fitting out the smooth component of the foregrounds along the frequency direction. This can be achieved by using polynomials (e.g., Santos et al. 2005; Wang et al. 2006; McQuinn et al. 2006; Bowman et al. 2006; Jelić et al. 2008, and references therein), or more advanced non-parametric methods (Harker et al. 2009a; Chapman et al. 2012, 2013). However, one should be careful in using polynomials. If the order of the polynomial is too small, the foregrounds will be under-fitted and the EoR signal could be dominated and corrupted by the fitting residuals. If the order of the polynomial is set too large, the EoR signal could be fitted out. Hence, in principle it is better to fit the foregrounds non-parametrically – allowing the data to determine their shape – rather than selecting some functional form in advance and then fitting its parameters (Harker et al. 2009a; Chapman et al. 2012). In addition, fitting directly to the visibilities rather than the image cubes might be another avenue to remove foregrounds.

All current EoR radio interferometry arrays have an instrumentally polarized response, which needs to be calibrated. If the calibration is imperfect, some part of this polarized emission is transferred into a total intensity and vice versa. As a result, leaked polarized emission can mimic the cosmological signal and make its extraction more challenging (Jelić et al. 2010a; Geil et al. 2011). Although this could be a problem when analysing the intensity maps, no methods of foreground extraction have yet been implemented that take this effect into account. Future analysis including polarised data should establish how much this polarised leakage has to be controlled in order for proper foreground subtraction to be performed.

The following are some requirements of the foreground properties required for the EoR fields:

- high Galactic latitudes with low Galactic radio emission and polarization;
- minimal Galactic or extragalactic emission on any scale;
- minimal power in the foreground structure at angular scales of $10' - 30'$;
- no complex bright radio sources within or near the edges of the field.

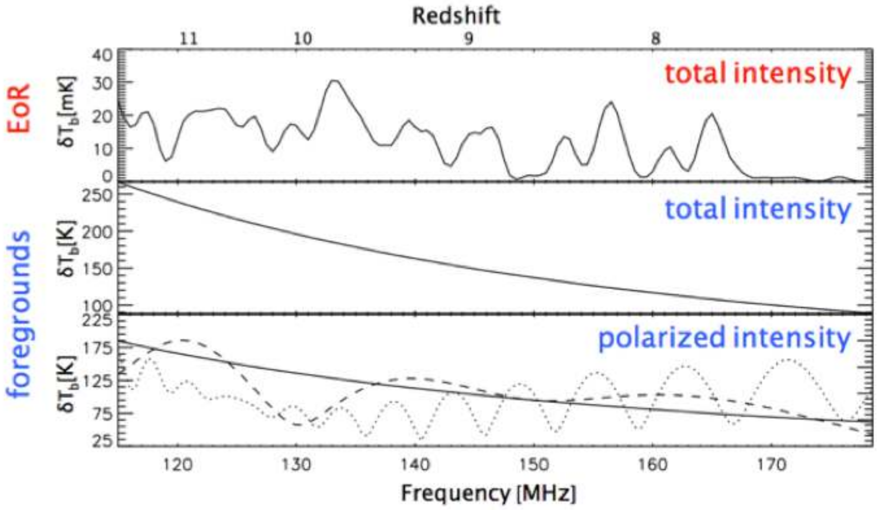

Fig. 16 Behaviour of the EoR signal and the foreground emission along the frequency direction (Thomas et al. 2009; Jelić et al. 2010a). The foreground removal techniques are based on the smoothness of the foregrounds in total intensity. The polarized component is not expected to be smooth, which combined with polarization calibration errors may complicate foreground removal. Courtesy of V. Jelić

A possible strategy for selecting those fields would be to observe a series of increasingly deeper but smaller fields, starting from an all-sky shallow survey. This "wedding-cake" approach could at the same time be used as global sky model for calibration and side-lobe leakage removal.

4.3 Ionosphere

One of the major distortions of the long wavelength radio-wave signal coming from cosmic sources is caused by the Earth's ionosphere and possibly even by the troposphere (Hewish 1951, 1952). Ionized gas causes both changes in phase and in amplitude of the radio-waves. These are directionally-dependent and can act differently on left/right-hand polarized waves due to Faraday rotation caused by the Earth's magnetic field. If not corrected for, especially at frequencies approaching the ionospheric plasma frequency around 5–10 MHz, the resulting image will be heavily distorted (see e.g. Cohen & Röttgering 2009) by an "ionospheric point-spread function" (e.g. Koopmans 2010).

One can look at the effect of the ionosphere in the following way (see e.g. Ratcliffe 1956): The sky can be described by a (infinite) set of points, each emitting a (Gaussian) random signal. The expectation value of the electric field squared is the source intensity and the random signal from different directions do not correlate (e.g Thompson et al. 2001). Each point emits a spherical wave, which just above the earth's ionosphere/atmosphere can be assumed planar. The latter is distorted while travelling through the ionosphere. Under the first-order Born approximation[5] one can approximate the plane-wave distortion by integrating over the index of refraction of the ionosphere via straight lines.

It can be shown that the spatially-varying phase distortion in the direction of a point source is proportional to a slice, perpendicular to the line-of-sight to the source, through the three-dimensional Fourier transform of the ionospheric refractive index (Koopmans 2010). For a wide field of view, these slices are tilted with respect to each other, causing their phase distortions to become increasingly uncorrelated over the field-of-view for a thick ionosphere (see e.g. Cohen & Röttgering 2009). This is equivalent to the iso-planatic patch in adaptive optics (AO), the area over which a single bright source can be used for AO corrections. One can show that the three-dimensional nature of the ionosphere then becomes important. This can be seen because looking under large angles away from the phase-center one sees structure in the ionosphere as function of height, under an oblique angle. For a 2D phase screen this is not the case except for very gradual change in projected density. As a result, directionally dependent phase-solutions are necessary for low-frequency wide-field arrays such as SKA, but also for present-day low-frequency arrays such as PAPER, MWA, GMRT and LOFAR.

---

[5] The physical distance of a deviation of the wave-vector from the straight line it would follow without the ionosphere, is smaller than the dominant scales that cause phase distortions of the plane wave.

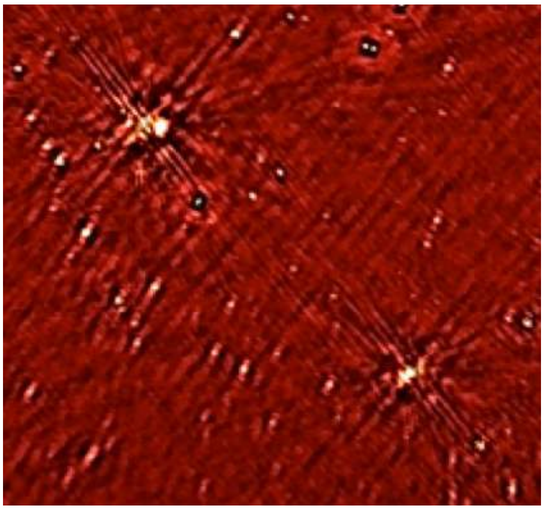

Fig. 17 A zoom-in on a LOFAR 150 MHz observation of the field around 3C196, showing what are presumably residual ionospheric effects around several brighter sources in the field. Note the correlation between the effect over the relatively small distance between the sources. These residuals are due to directionally-dependent ionospheric distortions on time-scales currently below the shortest solution interval in the calibration of the data. Taken from Labropoulos et al., in preparation

Some of the issues that therefore need to be confronted by any deep EoR observation with SKA are listed below:

- **Signal-to-Noise:** The ionosphere changes on time-scale of tens of seconds, which sets a maximum integration time beyond which visibilities start to de-correlate at some level (Bourgois 1981). Phase distortions correlate strongly between wavelengths, which can be used to compensate for short integration time. However, for a given bandwidth, the maximum integration time sets the S/N ratio of the images (or visibilities) and therefore the typical distance between brighter calibrator sources in the FoV. The lower the S/N ratio the further calibrator sources will be separated. If the distance between sources becomes too large, the EM phases of weaker sources in between them can partly de-correlate causing them to be smeared by "seeing" (see Figure 17). It is unclear at which level this seeing (i.e. blurring on arc minute scales) will show up and what effect it will have on the dynamic range of deep images with SKA. For example, currently a dynamic-range of about a million to one has been reached with LOFAR on fields with a bright (80 Jy) compact source (e.g. Yatawatta et al. 2013, and Lambropoulos et al. 2013 in preparation) using solution time-scales of $\sim$10 min. However, one still needs to go factor of $\sim$10-100 times deeper to reach mK sensitivity levels with SKA. Whether ionospheric seeing will limit this ability requires further study. The effect of seeing can however be eleviated by a larger collecting area of the array (i.e. calibrator sources can be fainter and thus closer together) and by the use of longer baselines (i.e. source confusion is limited in the modelling and ionospheric corrections). The question for SKA is therefore what signal-to-noise per integration time and bandwidth is required to enable ionospheric corrections over the entire image FoV to a level of $\sim$ 1 mK per few arcmin beam. It should also be investigated whether these effects are smeared out sufficiently and can be subtracted in the foreground removal process (e.g. in optical ground-based images PSF-blurred point-sources can be removed without deconvolution as long as the noise is not speckle-noise but thermally dominated; the latter is unclear in radio-astronomy to the depth of current or future low-frequency arrays).
- **Three-dimensional Ionosphere:** As mention above, the ionosphere is not well described by a 2D phase screen and requires 3D modelling at low frequencies a over wide fields of view. Deep observations e.g. with LOFAR (e.g. Yatawatta et al. 2013, and Lambropoulos et al. 2013 in preparation) and the GMRT (e.g. Cohen & Röttgering 2009) show strong directionally dependent image distortions below a few hundred MHz. This indicates that over the wide FoV of these arrays the 3D nature of the ionosphere cannot be neglected. A number of different approaches (or suggested approaches) have been taken thus far (e.g. Intema et al. 2009; Matejek & Morales 2009), among which are multiple phase screens, "rubber-sheet" models (which correct mostly for source motion, i.e. equivalent to tip-tilt corrections in the optical), interpolation of Jones matrices for calibrator source and 3D electron-density modelling. It remains unclear which, if any, of these approaches is the best compromise between complexity, computational speed and being physically correct. In addition, the effect of Faraday rotation might be more serious than expected causing non-zero XY visibilities for unpolarized sources due to differential Faraday rotation on baselines as short of ten of kilometers as seen with LOFAR (A.G. de Bruyn, private communications). If not accounted for, this might cause artificial polarization of the sky. All

these, and possibly yet unknowns effects, need to be accounted for to a level of μJy on baselines of a few km, where the EoR signal is expected to be seen with SKA-low.

- **Long Baselines:** Another important question that requires addressing is whether long baselines are required for SKA-low to correct for ionospheric effects on short baselines (where the EoR signal dominates). Ionospheric distortions should be smaller on shorter baselines because the ionosphere correlates much stronger over small physical distances. The outer scale of the ionosphere can be tens of kilometers and the inner scale meters (e.g. Thompson et al. 2001; Cohen & Röttgering 2009). In between these scales the power-spectrum is a steeply declining power-law. Hence most phase distortions are caused by large-scale structure (i.e. many kilometers). One notes however that the field-of-view of many current arrays is tens (few degrees) to hundreds of km (tens of degrees) projected on the ionosphere, incorporating many less correlated ionospheric structures and causing directionally dependent phase structure.
  However, on short baselines where these effects are smaller, the Galactic foregrounds are much brighter and source confusion is much larger. So small phase errors can be very hard to distinguish from a change in the sky model and small errors could cause leakage of the foreground emission into the EoR signal. Any such leakage at the level of μJy per few arc minutes in the emission over a $\sim$1 MHz bandwidth would be detrimental to the imaging of the EoR signal (e.g. Jelić et al. 2008). In this situation, the use of long baselines has many advantages: (i) the sky on long baselines is far simpler and consists mostly of compact easy-to-model sources, (ii) source confusion is far lower and on baselines of tens of kilometers can be below the EoR signal. Confusion noise can thus be avoided in the process of calibration. (iii) Compact bright source structure is far easier to determine using long baselines, allowing these sources to be subtracted from the shorter baselines without leaving residuals, (iv) Long baselines also allow sources to be seen along many different angles through the ionosphere helping dramatically in the determination of the 3D structure of the ionosphere. See Section 5.2.3 for more discussion as well.

4.4 Radio Frequency Interference (RFI)

The increasing demand for commercial usage of the electromagnetic spectrum makes it more difficult to carry out interference-free astronomical observations. The SKA will be larger with significantly more receiving elements and collecting area, and will thus be more sensitive than any existing radio interferometer. In addition, it will have large fields of view, large observational bandwidths with high resolution and the capability to simultaneously observe in multiple directions ('multi beaming'). All this brings new challenges to the data processing, including RFI excision.

Interference can occur due to a variety of reasons such as (but not limited to) sparking ignition systems, arcing sources, high-voltage power lines, satellite systems, the active Sun, malfunctioning receivers, incorrect observing parameters, communication systems, lightning, meteors, cars, trains and airplanes, etc. RFI has a complex time-frequency-polarization structure with a very high dynamic range in amplitude. Even though several signal processing methods are in use to counteract RFI, in practice there is no universal fool-proof technique. In view of this, RFI mitigation is achieved by using a combination of several engineering practices and techniques.

RFI mitigation is generally carried out at three principal stages of astronomical data processing, namely real-time pre-detection and pre-correlation processing, real-time post-correlation processing, and off-line processing (Fridman & Baan 2001; Bell et al. 2000). RFI mitigation is carried out at several stages starting from raw visibilities (or possibly even directly on the EM signal), calibration solutions where subtle errors may generally surface and be detected, and then on calibrated visibilities.

For the large data sizes generated by telescopes like SKA, a fully automatic computationally efficient scheme needs to be developed with the aim to achieve an effective, reliable and accurate RFI excision for SKA. Several examples of such automatic data-flagging systems exist (Offringa et al. 2010; Pearson 2002), but there are situations where manual intervention is still required for excising very subtle errors which escape automatic RFI excision. For SKA an approach exploiting the natural strengths of signal processing techniques and judiciously applying them at various stages of data processing is an inevitable requirement.

4.4.1 RFI environment and statistics

The number of interference points in the data varies with the site where the telescope is located, apart from other factors like in-house generated interference. For example, in LOFAR data the typical amount of data affected by

RFI is about 3 to 4% within the 120-240 MHz range. Typically the RFI detected is narrow band width a bandwidth less than 2 KHz.

A systematic study of detected RFI statistics for several days (distributed between 1994-1999) of astronomical observations at 151.5 MHz with the Mauritius Radio Telescope (MRT) revealed that the number of interference points falls monotonically with the strength of interference (Golap et al. 1998). This illustrates the important aspect that a still substantial low-level (close to the thermal noise) RFI population can exist in the data. Such low level RFI may need to be detected and dealt with for sensitive experiments such as EoR studies. Although SKA-low will be located in a remote area in Western Australia, astronomical observations can still be expected to be affected by RFI, especially of low-level strength, also from satellites, reflections from meteorite trails, reflections from the ionosphere of ground-based transmitters, airplanes, etc.

4.4.2 RFI mitigation for SKA

The following issues may be relevant for RFI mitigation at SKA. Foremost we need to reiterate that even if a good automatic RFI mitigation system can be developed, it will require substantial computational efforts and may imply some loss in signal integrity. Furthermore the future of RF allocations is difficult to predict and as a result so is the RFI environment. For the cosmological 21cm signal, it is important to study the effects and minimize any change in the statistical properties of the data which may be caused by the RFI mitigation system.

It is beneficial to have SKA located in an as radio-quiet zone as possible, although results with LOFAR show that some RFI can be dealt with even in urban environments (Offringa 2012; Offringa et al. 2013). Narrow-band RFI excision is relatively easier. Studies with LOFAR have shown that flagging techniques can excise RFI from a large fraction of the EoR imaging frequency range with very low levels of data loss (typically 3-4%), because of LOFAR's high time and frequency resolution of around 1 s / 1 kHz. Compared to this, the typical data loss is about 10% for astronomical observations with the MRT mostly due to the poor spectral resolution of 1 MHz. Therefore, it is imperative that SKA will have high spectral and time resolution.

The frequency ranges of FM stations (87-108 MHz) and DAB stations (180-230 MHz) are important for imaging the EoR, but it would be extremely difficult to use them (even after flagging) since transmitters might be seen continuously and occupy many spectral channels. Even in remote areas, the signals that are generated by the radio stations might need to be excised from the data to be able to image the EoR. Techniques currently in development that could suppress the transmitters, such as spatial filters and/or cyclostationary filters, might suffice but have never been applied on such a scale. Further research in such methods is therefore pressing, and possibilities to extract the EoR signals from non-contiguous spectra needs to be further investigated as well. Furthermore, RFI should be an important consideration in deciding the number of ADC (analog to digital converter) bits required for SKA and how many bits are needed in digital processing stages after digitization. Even with a radio-quiet site, the signal path should remain linear under the presence of strong transmitters. Additionally, its band-pass filters should be designed to block strong interference, and attenuate out-of-band interference. After all, even the most radio-quiet sites will see satellites and air-traffic, and the future radio environment might look different (Boonstra et al. 2009).

Depending on the algorithm used, the order in which data is stored is a relevant aspect for the speed of RFI mitigation and the process of data reordering can dominate the computational costs. Given the amount of data to process, RFI mitigation processing not only has to be automatic but might have to be integrated with the calibration and imaging process so as to minimize input-output load. Since the order in which RFI mitigation, calibration and imaging require the data are usually different, it would be very useful to formulate schemes/algorithms where there can be synchronization between the three processes for computational efficiency. Continuous monitoring should be carried out to generate valuable statistical data on RFI, which will be of additional help in combating it.

4.5 Calibration

The cosmological 21cm signal is weak compared to the foregrounds at all frequencies which are relevant for the study of the EoR and Cosmic Dawn, but more so at lower frequencies. Although it should be in principle possible to subtract these foregrounds, in order to do so, the signal should have a high degree of accuracy, or in other words, it needs to be calibrated to a level which allows the subtraction of foregrounds to the level that the cosmological 21cm signal can be detected. Calibration in this context thus is the correction of errors introduced by the propagation path and the instrument, as well as the removal of bright celestial sources from the data. After this first step, more specialized EoR specific data processing can be carried out (see Section 4.2).

There are many aspects connected to calibration and here we only want to list a few important points. The major sources of errors in a typical EoR observation can be categorized as follows:

- Atmosphere: Ionosphere and troposphere (see Section 4.3).
- Receiver beam shape: The phased array beams to be used in SKA stations are formed by coherent combination of multiple receiver elements (dipoles). During a synthesis observation, in order to track a given direction in the sky, the beam forming weights have to be varied. This will inevitably result in the variation of the beam shape over the full field of view (although it remains fairly constant along the tracking direction). Moreover, the beam shape of each station typically differs somewhat from the others, due to different element layouts as well as effects such as mutual coupling. Images made using such varying and heterogeneous beams will introduce distortions, particularly at the edges of the field of view. Apart from this, grating lobes could appear far away from the main beam beyond a certain frequency range, depending on the element configuration. Strong sources passing through grating lobes can act as sources of interference. The element beam will have a strong polarization response, necessitating full polarimetric data models.
- Receiver signal path: A cascade of amplifiers and other signal processing units comprise the path connecting a single station with the correlator. The properties of such units vary and has to be corrected for, both before and after correlation. For instance, in LOFAR, a major source of error in the signal path were station clocks being slightly out of synchronization. This problem has now been fixed through the implementation of a common clock for the core area. SKA may want to follow a similar strategy.
- (Unmodeled/Imperfectly modeled) Celestial sources: A requirement to obtain satisfactory calibration is the (at least partial) knowledge of the sky being looked at. This model is iteratively updated during calibration and consequent imaging. In particular, compact and bright foreground sources have to be modeled accurately. The model should not only have the intensity and polarization of each source, but also the shape information. In almost all cases some sources will have structure above or around the resolution scale. Therefore, having high resolution data (from longer baselines) is crucial for such sources. Short baselines are also affected by emission from the Galactic plane.
- Smearing: Due to limited capabilities to process (correlate/calibrate) as well as store data, some form of averaging has to be performed, both in time and in frequency. This distorts images, particularly those with a wide field of view.
- Closure errors: Errors that cannot be decomposed as belonging to stations are called closure errors. There are various causes for closure errors. For instance, nonlinearities introduced at the receiver frontend (saturation, quantization errors) could cause closure errors. Furthermore, imperfect models of bright extended sources used in calibration would also introduce such errors.

Ideally, calibration will be able to reduce all these errors to below the theoretical noise level. Some of these errors are controllable and can be reduced by a careful system design (e.g., the clock synchronization) or handling of the data (e.g., smearing due to averaging).

4.6 Selected results from SKA precursors and pathfinders

Here we summarize some results from SKA precursors and pathfinders relevant for CD/EoR science. The relevant telescopes are WSRT, LOFAR, MWA, PAPER and GMRT.

- WSRT: Observations with the WSRT-LFFE (Low Frequency Front End) served as a pathfinder for the LOFAR-EoR experiment and hence for SKA as well. The observed fields were centered at the quasar 3C196 (80 Jy in peak intensity at 150 MHz) and the North Celestial Pole (NCP, brightest source 5 Jy at 150 MHz). Both fields are well away from the galactic plane and are also target fields for the LOFAR-EoR observations. A dynamic range of about 150,000 to 1 was reached in the 3C196 field (Bernardi et al. 2010). The limitations were mainly due to source confusion and ionospheric variations. In the 3C196 field, off-axis sources could be removed with an accuracy better than 1%. Polarization was calibrated in a direction independent fashion by solving for the off-diagonal elements of the Jones matrix. Given the equatorial mount of the WSRT, a single solution was usually sufficient to obtain a polarization accuracy at the 0.5% level throughout the whole 12h synthesis. Since there is no well-established polarized beam for WSRT at very low frequencies, instrumental polarization of

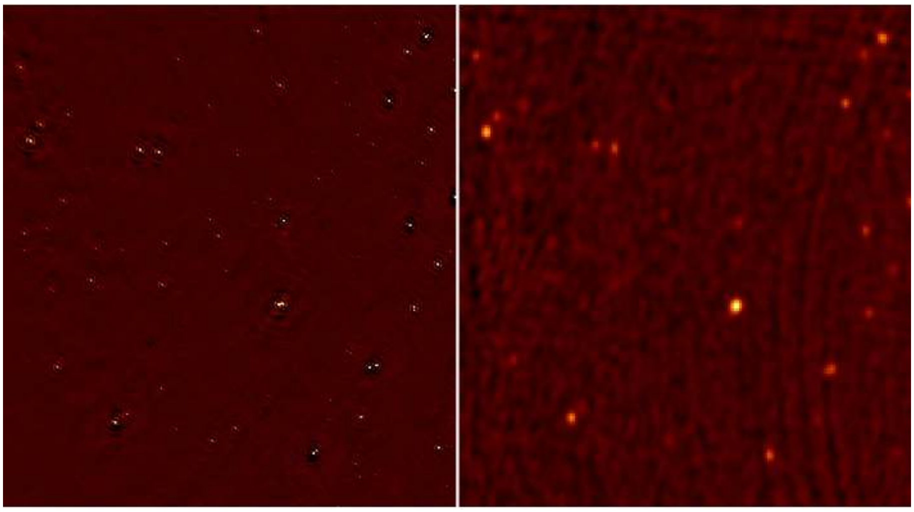

Fig. 18 Deep observations of a small area in the 3C196 field at 150 MHz. *Left panel*: LOFAR, *Right panel*: WSRT. Based on data from Labropolous et al., in preparation and Bernardi et al. (2010).

points sources was corrected by fitting their response in the image plane, assuming that all their Stokes Q & U signals were due to instrumental polarization. This set the first limit on the power-spectrum of the Galactic foregrounds (Bernardi et al. 2009, 2010).

- LOFAR: During the commissioning phase, LOFAR regularly observed the same two fields as were previously observed with WSRT, namely 3C196 and NCP. The frequency range used was 115-165 MHz. With an effective integration time of about 10 hours, a noise level of about 100 μJy (NCP) and a dynamic range of about 0.5 million (3C196) was reached. The main limitations currently are due to imperfect knowledge of the sky model, as well as ionospheric and beam shape errors. A noteworthy fact is that the noise level reached is within a factor of 1.5-2 of the theoretical limit. The increase in sensitivity compared to WSRT as well as more advanced calibration techniques (in particular directionally-depenend calibration) as well as the longer baselines up to $\sim$100 km allowed for these substantially better results (Yatawatta et al. 2013).
- MWA: The Murchison Widefield Array (MWA, Tingay et al. 2013) consists of 128 aperture arrays (known as tiles) distributed over a $\sim$ 3 km diameter area at the Australian SKA site. A 32 tile prototype has operated since 2010 and some results from this 32T array have been published (Williams et al. 2012; McKinley et al. 2013). An early demonstration of the real-time calibration and imaging pipeline was obtained on a field centred on PictorA (Ord et al. 2010). This observation had an effective integreation time of 8 hours observations and 100 MHz frequency coverage.
- PAPER: The Donald E. Backer Precision Array to Probe the Epoch of Reionization (Parsons et al. 2010) consists of 64 isolated dipoles at the South African SKA site. PAPER employs a novel calibration technique based on delay-delay filters (Parsons & Backer 2009; Parsons et al. 2012b; Pober et al. 2013). Given the limited collecting area, PAPER will employ re-configurability into a maximum redundancy configuration in order to achieve the deepest sensitivity on a limited range of k modes (Parsons et al. 2012a). Not employing any beam-forming, the observations are done in drift scan mode. An expansion from 64 to 128 elements is in progress and in the future the array may even grow to 256 elements.
- GMRT: The GMRT reionization experiment is an ongoing effort to detect neutral hydrogen 21-cm signal statistically at 150 MHz. Ali et al. (2008) characterized the foregrounds on sub-degree angular scales at this frequency and find that the measured multi-frequency angular power spectrum is roughly in agreement with the expected value (Datta et al. 2007). They also found the foregrounds to be oscillatory in frequency. This measured oscillatory behavior can be reduced by suppressing the side-lobe response of the primary antenna elements. Ghosh et al. (2012) found that the suppression works best at the scales for which there is a dense sampling of the uv-plane. These authors also measured the fluctuations in the galactic diffuse emission at the $10'$ scale after removing bright radio sources. Pen et al. (2009) have carried out 150 MHz GMRT observations at a high Galactic latitude to place an upper limit of $\sqrt{\ell^2 C_\ell/2\pi} < 3$K on the polarized foregrounds at $\ell < 1000$. Paciga et al. (2011) placed an upper limit on the 21-cm power spectrum during the EoR of (70 mK)^2 at wavenumbers of $k = 0.65$ h/Mpc which after a more careful handling of the foreground subtraction had to be

increased to $(248\ \mathrm{mK})^2$ for $k = 0.50\ h/\mathrm{Mpc}$ (Paciga et al. 2013). This shows how proper foreground removal remains a challenge. Removal of RFI, compensation for ionospheric disturbances, proper calibration of radio sources etc., are among the major challenges that the GMRT faces currently though efforts are ongoing to overcome some of the hurdles (Roy et al. 2010; Prasad & Chengalur 2012).

4.7 Lessons learned from current SKA pathfinders

The early observations from the telescopes mentioned above are still quite far from their ultimate goal of detecting any EoR signal. However, the following aspects important for reaching a detection have already become clear.

- The wide fields of view that are observed include thousands of celestial sources and atmospheric/instrumental corruptions that significantly vary with direction, time and frequency. Therefore, an efficient and accurate calibration along different directions is essential. Until recently, (sequential/simultaneous) calibration approaches based on the concept of peeling were the only methods available for such calibration. However, recent developments have provided substantial improvements both in computational cost and accuracy (Yatawatta et al. 2008; Kazemi et al. 2011).
- Subtraction of bright sources (down to the noise level; see e.g. Trott et al. 2012) requires construction of accurate source models. In a typical observation, a few complicated sources, and thousands of point, double, and triple sources can be seen. Accurate models are needed not only for the complicated extended sources but also for the thousands of weaker compact sources. In particular, orthonormal basis functions such as shapelets (Yatawatta 2010) and prolate spheroidal wave functions (Yatawatta 2011) provide efficient ways of representing extended sources. In order to construct these accurate models, long baselines are essential.
- Although it is popular to quote a dynamic range reached in order to indicate the quality of the calibration process, it should be realized that this quantity is not the entirely correct criterion for measuring the quality of EoR observations (see e.g. Braun 2013). If the field contains a very bright source, chosen for calibration purposes, one can obtain a very high dynamic range without actually reaching the theoretical noise limit. On the other hand, in a field with only weak sources, the maximally achievable dynamic range is relatively low but the noise limit could be reached, provided proper calibration. At this point it is hard to make firm statements on whether the presence of a bright source in the field is to be preferred over the absence of one, although LOFAR observations of the 3C196 (with bright source) and NCP (without a bright source) fields seem to suggest that in both cases the thermal noise can be reached.
- For producing an accurate source model construction and calibration along multiple directions, it is important to achieve a high, preferably full, *uv* coverage.
- Full polarimetric calibration is essential to handle the element beam polarization response as well as differential ionospheric Faraday rotation.
- Finally, experience with LOFAR has shown that long baselines greatly benefit directionally-dependent calibration, modelling of the sky as well as ionospheric corrections.

In the next section we further examine the basic requirements for SKA-low that allow the science as outlined in the earlier sections to be accomplished.

5 Implications for SKA design

Having presented (i) an overview of the science one might envisage doing with SKA-low, (ii) how one might want to do it and some of the observational aspects relevant for this, we now give an overview of what this implies for the design and lay-out of SKA-low. The critical issues that need to be considered for Cosmic Dawn/EoR science are the following:

- **Frequency Coverage:** This sets the redshift range over which the HI signal from cosmic dawn and epoch of reionization can be observed. Current observational and theoretical constraints set this frequency range.
- **Antenna Distribution and uv-coverage**: The distribution of antennas is important for the detection of the EoR signal on short baselines (less or equal to a few kilometers), calibration of the instrument, correction for ionospheric effects, reduction of confusion noise and determination of the structure of bright compact source and foreground removal, using especially the longer baselines. In addition, instantaneous *uv*-coverage sets limits on the number of antennas for a given collecting area and core area.

- **Field of View, Multi-beaming and Station Size:** The FoV of the smallest array element for which visibilities are stored (e.g. dipole, tile, station) determines the largest scale for which information can be retrieved (e.g. through imaging or power spectra, etc.). The largest scale needed for CD/EoR science therefore sets the minimal FoV. Multi-beaming can increase the total FoV, but cannot recover fluctuations and structures on scales larger than the single beam FoV (without substantial computational cost).
- **Collection area or $A_{\mathrm{eff}}/T_{\mathrm{sys}}$:** This sets the overall sensitivity of the array both for deep multi-epoch imaging (i.e. tomography) and instantaneous signal-to-noise for calibration purposes. In combination with the antenna distribution it also sets the sensitivity for power-spectrum measurements.

We discuss each of these in more detail in the following sections.

5.1 The Frequency Coverage

In this section we present the optimal frequency range inferred from current knowledge about the CD and EoR[6]. The redshift/frequency range proposed here is well motivated, especially at low redshifts by observations of the Gunn-Petersson effect, and at higher redshifts through better understood physics and theoretical models that reproduce the current observational constraints at $z \lesssim 10$.

5.1.1 Upper and lower limits

The upper limit on observations of neutral hydrogen during the CD/EoR is set by the time when the Universe becomes (nearly) fully ionized again at $z_{\mathrm{low}} = (\nu_{21}/\nu_{\mathrm{up}} - 1)$, where $\nu_{21} = 1420\,\mathrm{MHz}$. Below z_{low} only a small fraction of the Universe remains neutral, residing mostly in galaxies. Studying this residual neutral HI constitutes a different science case (e.g. galaxy evolution, baryon acoustic oscillations, etc) that will not be addressed in this white paper. It is generally accepted that reionization is completed around $z_{\mathrm{up}} \sim 5-6$ based on the Gunn-Peterson absorption as observed in high-z quasars (Fan et al. 2006). Conservatively a rise in the optical depth for HI absorption and dark gaps, presumably due to patches of neutral hydrogen, are starting to appear around $z = 5.6$ which correspond to $\nu_{\mathrm{up}} = 215\,\mathrm{MHz}$. Some neutral patches might remain at even lower redshifts at a level of as much at $\sim 10\%$ at $z \sim 5$ (Mesinger 2010). One might argue that this is the transition phase between the EoR and the phase in which galaxies as we see them today start to emerge and evolve over time. An upper frequency limit of $\nu_{\mathrm{up}} = 215\,\mathrm{MHz}$, however, seems to be the best estimate to cover the end of the EoR.

A stringent lower limit in principle does not exist, because hydrogen is mostly neutral after the recombination era ($z \sim 1100$), although it is not expected to be observable for all redshifts below that. A lower limit is therefore given by when the first redshifted 21-cm signals are detectable. As explained in Section. 3.1 this requires the spin temperature of the neutral-hydrogen gas to be different from the CMB temperature, which requires either the presence of Ly-α photons or high densities. Below $z \sim 30$ extended regions of high density become very rare. When sufficient Ly-α photons appear depends on early star formation and black hole growth, which is not really known and motivates the high redshift SKA observations of the Cosmic Dawn in the first place. Based on the (nominal) theoretical models from Pritchard & Loeb (2008) as shown in Figures 19 and 20, one infers a lower limit on the start of 21-cm absorption due to the first stars and itermediate mass black holes of $\nu_{\mathrm{low}} = 54\,\mathrm{MHz}$, which corresponds to $z = 25$[7]. We note however that this value depends on the star forming efficiency and the amount of radiation escaping the (proto-)galaxies in three spectral bands: Lyman band, ionizing UV and X-rays. These parameter are somewhat constrained by the existing observational data, but there is still large uncertainty. Figure 20 shows predictions for the evolution of the brightness temperature power spectrum from both theoretical models (Pritchard & Loeb 2008) and radiative transfer numerical simulations (Baek et al. 2010). One can check that the shape and amplitude are similar in both approaches, but that the redshift where features appear differ. Semi-numerical models (Santos et al. 2008) show the same pattern, with general agreement on the shape and amplitude, but different redshifts for the features. The redshift discrepancy is mainly due to the uncertainty in the star forming efficiency and the limited resolution of the simulations. Moreover, the recent discovery of a coupling between large and small scale modes in the the dark-matter distribution during recombination, causing bulk velocity flows

---

[6] This section is based on a memo written by two of the co-authors (LVEK and BS) as part of the SKA Science Working Group to inform the SKA Project Office on the optimal frequency range(s) for high-redshift HI studies.

[7] We note that these redshifts are not as precisely determined as quoted here from either observations or theory, but we would like to be precise in corresponding redshifts and frequencies.

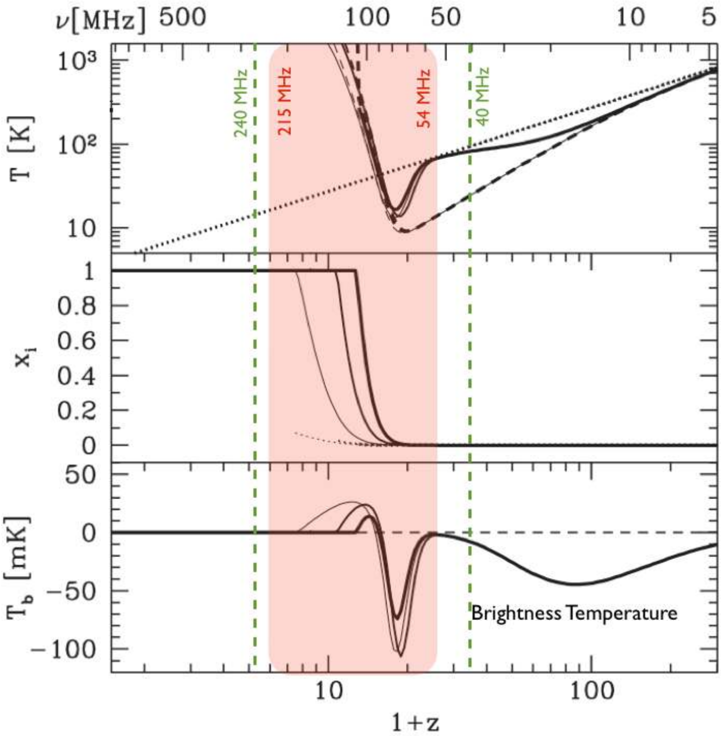

Fig. 19 Top panel: Evolution of the CMB temperature $\mathrm{T_{CMB}}$ (dotted curve),the gas kinetic temperature $\mathrm{T_K}$ (dashed curve), and the spin temperature $\mathrm{T_S}$ (solid curve). Middle panel: Evolution of the gas fraction in ionized regions x_i (solid curve) and the ionized fraction outside these regions (due to diffuse X- rays) x_e (dotted curve). Bottom panel: Evolution of mean 21 cm brightness temperature T_b. In each panel we plot curves for model A (thin curves), model B (medium curves), and model C (thick curves). From Pritchard & Loeb (2008).

in the HI gas (Tseliakhovich & Hirata 2010), predicts a substantially increase the strength of 21-cm brightness temperature fluctuations (factors 2–3) up to redshift as much as $z \sim 40$ (Visbal et al. 2012; McQuinn & O'Leary 2012). Consequently, if $z = 25$ is a reasonable upper limit encompassing most the nominal models above, a wider frequency range should be allowed for than the current 70-MHz lower limit, although possibly not designed for (e.g. by using a flexible set of frequency filters). This would allow the study of these new and exciting physical processes. Indeed, counter of expectations, LOFAR has taught us that interferometric imaging can be done down to frequencies ∼20 MHz (see e.g. van Weeren et al. 2012).

5.1.2 Extreme Range and Optimal Frequency

An extreme lower limit – excluding exotic physics – is when Ly$-\alpha$ emissivity (and star-formation) is extremely strong early on (by a factor of around ∼100 up from nominal) and is stronger than X-ray heating. In that case, 21-cm absorption due to Wouthuysen-Field coupling could start as early as $z \approx 35$ (Pritchard & Loeb 2012) or at $\nu \approx 40$ MHz, possibly leading to further enhanced and observable 21-cm brightness temperature fluctuations due to bulk flows at these redshift (Visbal et al. 2012; McQuinn & O'Leary 2012). Similarly, as argued by Mesinger (2010), hydrogen could remain partly (∼ 10%) neutral till $z \approx 5$ or $\nu \approx 240$ MHz. A more encompassing range, larger than 4:1, would therefore be 40–240 MHz (i.e. 6:1). One might strongly argue that this range should be allowed for by SKA, but not optimized for, since it covers most conceived and exotic CD/EoR scenarios.

The sensitivity of an antenna or a collection of antennae ('station') is normally expressed as $A_{\rm eff}/T_{\rm sys}$ or in short A/T which stands for the effective collecting area over the system (noise) temperature. The dominant contribution to $T_{\rm sys}$ at low frequencies is the sky the value of which decreases quickly with increasing frequency. For dipoles collected in stations $A_{\rm eff}$ remains roughly constant below the optimal frequency $\nu_{\rm opt}$ and above it decreases roughly as $\propto (\nu/\nu_{\rm opt})^{-2}$, as the station becomes sparse. Therefore, A/T will typically be optimal near or above $\nu_{\rm opt}$. A precise choice of the optimal frequency also impacts the collecting area per dollar. Choosing $\nu_{\rm opt}$ too low will lead

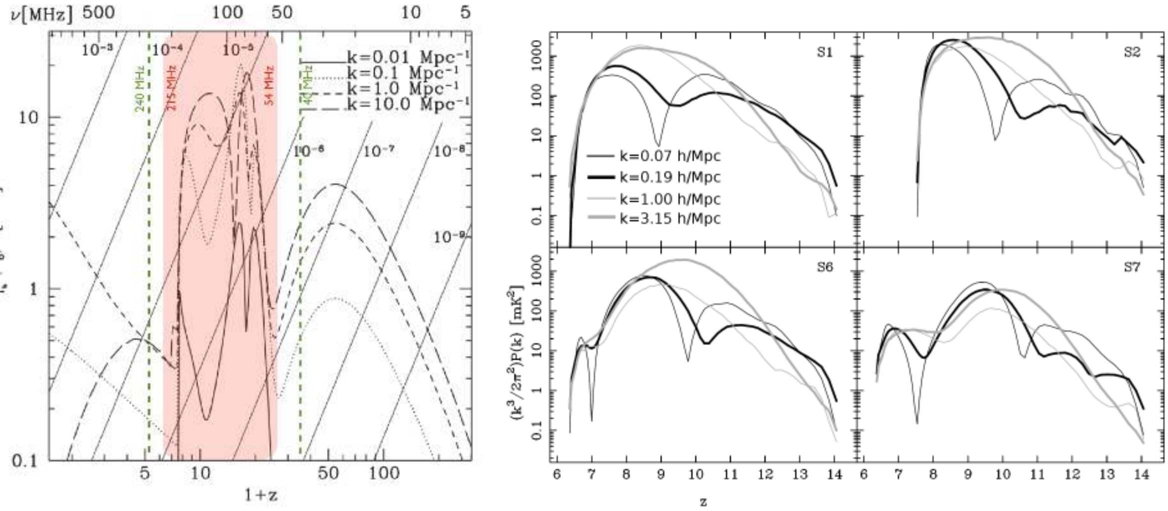

Fig. 20 **Left:** Evolution of power spectrum fluctuations based on theoretical modeling. The different curves show $P(k,z)$ as a function of z at fixed k for k = 0.01, 0.1, 1, 10 Mpc^{-1}. Diagonal lines show $\varepsilon T_{\rm fg}(\nu)$, the foreground temperature reduced by a factor ε ranging from 10^{-3} – 10^{-9} to indicate the level of foreground removal required to detect the signal. Adapted from (Pritchard & Loeb 2012). **Right:** Evolution of the brightness temperature power spectrum with redshift, based on numerical simulations. $k = 0.07$ h/Mpc (thin black), $k = 0.19$ h/Mpc (thick black), $k = 1.00$ h/Mpc (thin gray) and $k = 3.15$ h/Mpc (thick gray). From model S1 to S7 the X-ray contribution is increasing. From Baek et al. (2010).

to considerably more collecting area per dollar at low frequencies but less at high frequencies. Given the frequency range of 54–215 MHz chosen as being optimal and also a broad "peak" in the brightness temperature fluctuations as seen in the right panel of Figure 19, an optimal frequency in the middle of this range i.e. $\nu_{\rm opt} = 108$ MHz would be best.[8]

5.1.3 Full Frequency Coverage

It is concluded that 54–215 MHz (i.e. a 4:1 range) is the most favorable range to cover the SKA-1 and 2 CD/EoR science case for redshifts $z = 5.6 - 25$, with an optimal frequency at $\nu_{\rm opt} = 108$ MHz ($z = 12$, but see footnote 8). The most narrow (3.5:1) range would be 54–190 MHz. Despite these "most optimal" but narrow ranges which in principle can be observed with a single dipole receiver system with an efficiency exceeding 0.1, one might strongly argue (in situations where possible) for these limits to be 'soft', allowing observations – albeit with limited sensitivity – over a wider range of 40 – 240 MHz ($z \approx 5 - 35$) to cover less likely and more exotic scenarios for the start of the Cosmic Dawn and end of the EoR, and potentially therefore consider a dual-band receiver system such as LOFAR for the lower and higher frequencies in the range 40 to 240 MHz..

5.2 Antenna distribution, Sensitivity and Collecting Area

Which antenna distribution for SKA-low would be optimal for reionization and cosmic dawn studies is still a matter of debate. In this section will draw some general conclusions which depend on optimizing both power spectrum and tomography measurements. Different SKA precursors (e.g. MWA, PAPER, LOFAR) follow different strategies, even though they all focus on power spectra determination. The differences are mostly in the ratio between longer and shorter baselines, collecting area and 'core area', the area over which the shorter baselines are distributed.

In determining the antenna distribution, one should account for

---

[8] We note that this assumes that the collecting area (or $A_{\rm eff}$ per antenna) that can be purchased per dollar is a function of $\nu_{\rm opt}$. We suspect, however, that it will not be a strong function and that $A_{\rm eff}$ goes up with $\nu_{\rm opt}$ going down, for fixed costs, because dipoles do not linearly grow in cost with their effective collecting area. Hence, one might consider the extreme case where dipole size is not a cost factor. In that case $A_{\rm eff}$ grows with $(\nu/\nu_{\rm opt})^{-2}$ and offsets the loss in collecting area due to sparseness at frequencies greater than $\nu_{\rm opt}$. In that case, choosing a very low value of $\nu_{\rm opt}$ makes more sense, but could be limited by other factors such as land use, etc. A final choice of $\nu_{\rm opt}$ should therefore factor this cost in.

- How well can the science goals be achieved (i.e. power spectra, tomography, etc). This mostly involves maximizing the ability to detect the signal of interest over a wide range in redshifts and angular scales.
- How well can (i) RFI be excised, (ii) the instrument be calibrated for instrumental and ionospheric effects and (iii) foreground contaminants be removed (see Sect. 4). These questions focus more on observational strategies and on biases in the modeling, leakage, mode-mixing, covariance, etc.

Any observation has a set of unknown parameters that need to be solved for: (1) the sky model as function of direction and frequency and (2) the instrumental/ionospheric model. Solving both without introducing artifacts in the resulting sky model (which includes the HI signal), that ultimately could prohibit the science to be carried out, is of utmost importance in CD/EoR observations, especially because the signal is expected below the noise in all current experiments. For SKA the S/N ratio is expected to exceed unity for scales larger than a few arcminutes, at least for the higher frequencies. In this case biases should play a less important role. However, for power spectrum analyses at lower frequencies where some modes will have $S/N<1$, bias can still be very important.

Hence, whereas most studies and thinking thus far focused solely on how well the power spectra of redshifted 21cm intensity fluctuations can be measured (e.g. Bowman et al. 2006; McQuinn et al. 2006) this should not be taken as the only guidance for an array design. Whereas this is indeed the goal of *all* current SKA precursors, in the era of SKA itself, *tomography* (i.e. direct imaging of neutral hydrogen structures) is at least as important as measuring power spectra. Tomography comes with its own requirements which we will discuss below.

An example of this is the following: the most prominent features during the late stages of reionization are the ionized bubbles, which are a few to tens of Mpc in size; their positions correlate on scales of $\sim 120h^{-1}$ Mpc (Zaroubi et al. 2012), i.e. of order a degree at redshifts around $z \approx 10$. These bubbles have a contrast of ~ 30 mK (see Equation 2) between their fully-ionized inner region and the surrounding neutral hydrogen. What is important to map out these tomographic features, is not a baseline distribution that maximizes the sensitivity for power spectra measurements on that angular scale by making the array as compact as possible and hence placing many visibilities inside one uv-resolution element and through which phase information is discarded, but to have baselines that have instantaneous sensitivity on both the spatial and frequency scales of these bubbles (arc minutes, but also degrees!) and at the position of these bubbles in the images.

Whereas a very compact array might be well-suited to measure power spectra for a range of k-modes, using both their parallel (sky) and perpendicular (frequency) components, it will be ill-suited to image small-scale (arcminute) bubbles in the hydrogen distribution. The latter requires more baselines on scales of several kilometers rather than several hundred meters (see e.g. Zaroubi et al. 2012). Long(er) baselines are also very useful for foreground subtraction and calibration. They ‘see’ a simpler sky foreground consisting predominantly of relatively compact sources. These sources constitute a major contaminant whose effects have to be removed from the shorter baselines (where the CD/EoR HI signal predominantly is found) in order to reduce confusion noise and strong model degeneracies. The ability to resolve compact sources also allows for much easier calibration and three-dimensional ionospheric tomography as discussed in Section 4.3.

It is therefore critically important not only to optimize for power spectrum measurement, but also for tomography, and for the ability to calibrate the instrument and remove foregrounds. All this suggests that long(er) baselines are very useful, if not critical.

5.2.1 Power spectra measurements

Before considering the requirements for tomography and calibration, we first address those related to power spectrum measurements. To measure the power spectrum of the redshifted 21-cm signal, baselines should be placed at uv-points that correspond to the k-modes of interest. However, for measuring the three-dimensional power spectrum one should add to these the modes from the (Fourier-transformed) frequency domain.

Based on the derivation in McQuinn et al. (2006), and verified numerically, one can show that for a constant density of visibilities in the uv-plane, the noise error on $k^3P(k)/2\pi^2$ that dominates over cosmic variance in most instances (except for SKA itself where the S/N exceed unity per mode), can be written as[9]:

$$\boxed{\Delta^2_{\rm Noise} = \left(\frac{2}{\pi}\right) k^{3/2} \left[D_c^2 \Delta D_c \times \Omega_{\rm FoV}\right]^{1/2} \left(\frac{T_{\rm sys}}{\sqrt{B t_{\rm int}}}\right)^2 \left(\frac{A_{\rm core} A_{\rm eff}}{A^2_{\rm coll}}\right)} \tag{11}$$

---

[9] This equation is not given in this form in McQuinn et al. (2006), but has been derived using the same method as outlined there. In this form is gives the important scaling relations with array parameters useful to understand power-spectrum measurements.

This equation assumes that one integrates over $\Delta k = \varepsilon k$ with $\varepsilon = 1$ (i.e. one dex in k-scale; for other values of ε the above equation scales as $1/\sqrt{\varepsilon}$). It is extremely useful because its overall scaling relations hold very well and can easily explain the difference between different arrays (see discussion below). We note that $\Omega_{\rm FoV} = \lambda^2/A_{\rm eff}$ is the FoV of the smallest beam-formed receiver element, which sets the area of the sky that can be observed in one single pointing. The distances D_c and ΔD_c are the comoving distances to the redshifts where the frequency is centered and the comoving distance corresponding to a bandwidth B at that comoving distance. Hence the factor within the square root is the observed comoving volume. Because the error on the power spectrum decreases as the square-root of number of independent k-modes – a number proportional to $k^{-3/2}$ – and because $\Delta^2_{\rm Noise}$ scales as $\propto k^3 P^{\rm N}(k)$, the overall scaling of the noise error on the power spectrum is $k^{3/2}$. In addition, the term $(T_{\rm sys}/Bt_{\rm int})^2$ is the variance of the total power of a single receiver element for a bandwidth B and total integration time $t_{\rm int}$. Finally, the noise error scales with the factor $(A_{\rm core}A_{\rm eff}/A^2_{\rm coll})$, where $A_{\rm core}$ is the core area in which the receiver elements are distributed, $A_{\rm eff}$ is the effective collecting area per receiver element and $A_{\rm coll}$ is the total collecting area of the array (i.e. the number of stations $N_{\rm stat}$ times $A_{\rm eff}$). Even though this equation is only valid for a perfectly uniform density of uv-points, its scalings are correct. Redistributing the receivers will only tend to tilt the dependence on k.

Equation 11 highlights a number of points:

- First, we find that *power spectrum sensitivity is much better, in an absolute sense, for small k-modes.* Although this would naively imply that more compact arrays are better, it also implies that different k-modes are emphasized in that case. In general cosmological information is mostly contained in the smaller-k modes (i.e. large scales, peaking around 1 degree), whereas the larger-k modes mostly probe the astrophysics of reionization and the cosmic dawn (see Sections 2 and 3). Comparing arrays based on sensitivity at different k-modes is therefore comparing sensitivity to cosmology versus that to the astrophysics of reionization. One should compare arrays *only* for a fixed k mode and then evaluate how well the same scientific questions can be answered.
- Second, *the noise error decreases when more cosmic volume is probed.* This can be seen from the first two terms. The error scales with the square root of the number of independent k-modes within a range of Δk (in the above equation $\Delta k = k$). Hence the k-volume scales as k^3, but the comoving volume $\mathcal{V}$ scales with $\Omega_{\rm FoV} \propto 1/A_{\rm eff}$. Since the size of an independent element scales as $1/\mathcal{V}$, one finds that the error scales as $\sqrt{\mathcal{V}}$. At the same time, the number of independent modes increases with $1/A_{\rm eff}$ which allows the noise variance to scale as $A_{\rm eff}$ as shown in the last term of Equation 11. Combining the two terms, one gains in sensitivity by $\sqrt{A_{\rm eff}}$.
- Third, shrinking the core area ($A_{\rm core}$) substantially increases the sensitivity of the array (i.e. decreases the error), but at the cost of loosing the longer baselines and sensitivity for larger k-modes, if the collecting area of the array remains fixed. Shrinking the array can partly offset the loss in sensitivity when its total collecting area ($A_{\rm coll}$) decreases, but it also shifts sensitivity to lower k-modes, where the effects of the cosmic dawn and reionization are far less obvious. Shrinking an array to compensate for loss in collecting area is therefore not a cure to make up for a loss in sensitivity, because it shifts the focus of the science (i.e. from CD/EoR to cosmology).
- Fourth, the last factor in Equation 11 can be explained more intuitively as follows: as a trick we multiply it with $(A_{\rm eff}/A_{\rm eff})$. We then see that $(A_{\rm eff}/A_{\rm coll})^2 = N^{-2}_{\rm stat}$, where $N_{\rm stat}$ is the number of stations inside the core. The remain factor $(A_{\rm core}/A_{\rm eff})$ is the number of independent modes in the uv-plane that are covered by all visibilities. Since the number of visibilities is $\sim N^2_{\rm stat}/2$, the last factor in the above equation is nothing else than half the number of visibilities per uv-resolution element, $\langle n^{\rm cell}_{uv}\rangle$. Combining the last two factors, we see that it represents the noise variance per uv-cell after an integration time $t_{\rm int}$ and using a bandwidth B. This factor also allows a simple scaling from image noise to power spectrum noise, because it enters in the instantaneous noise error per image resolution element.

In summary, Equation 11 has two main contributing components: (i) the first two (apart from $2/\pi$) factors indicate the inverse of the square root of the number independent k-modes and (ii) the last two factors provide the noise variance per uv-cell. We note that this is very similar to what was found in Morales & Hewitt (2004) but provides a somewhat more intuitive picture. Keeping k, $T_{\rm sys}$, B and $t_{\rm int}$ the same, for different array configurations, we find the following scaling relations for the important array parameters:

$$\boxed{\Delta^2_{\rm Noise} \propto \left(\frac{A_{\rm core}\sqrt{A_{\rm eff}}}{A^2_{\rm coll}}\right) \propto \left(\frac{A_{\rm core}}{N^2_{\rm stat}A^{3/2}_{\rm eff}}\right) \propto \left(\frac{A_{\rm core}}{\sqrt{N_{\rm stat}}A^{3/2}_{\rm coll}}\right)\,.} \qquad (12)$$

Table 2: Parameters used for the SKA precursors/pathfinders and different SKA configurations to derive sensitivities for power spectrum measurements.

Telescope	$N_{\rm ant}$	Distribution	$A_{\rm eff}$ (m^2)	$R_{\rm core}$ (m)	$R_{\rm max}$ (m)
MWA	112	R^{-2}	14.5	20	750
PAPER	128	constant	7.1	x	150
LOFAR	48	R^{-2}	804	150	1500
LOFAR-AARTFAAC	288	constant	25	x	150
SKA	50; 150; 450	R^{-2}	$10^6/N_{\rm ant}$	500	2000; 5000

Equation 12 show that $A_{\rm coll}$ and the $A_{\rm core}$ are the two critical parameters, because they have the most impact on $\Delta^2_{\rm noise}$. It is better to first set $A_{\rm eff}$ to the optimal choice in terms of field of view and costs, and then vary $N_{\rm stat}$ until the required $A_{\rm coll} = N_{\rm stat} \times A_{\rm eff}$ is reached for power spectrum and/or tomographic requirements. We come back to this when discussing the required field of view, i.e. a maximum on $A_{\rm eff}$ (see Sect.5.3).

Although collecting area is the most critical factor, it can partly be compensated for – for a fixed but measureable k-range – by making the array more compact and splitting the collecting area in smaller stations or receiver elements. The latter increases the number of visibilities and lowers the thermal noise per uv-cell, but also increases the number of required correlations by a large factor, increasing the correlator and processing costs substantially. Two illustrative examples to improve the S/N by a factor of two are the following:

(a) Decreasing $\Delta^2_{\rm Noise}$ by a factor two requires a four times smaller $A_{\rm eff}$ for a fixed collecting area and core size, and thus generates 16 times more visibilities, requiring a 16-fold more powerful correlator as well as substantially more computing power to process and store these data.

(b) In contrast, the same factor of two requires only a factor $2^{2/3} \approx 1.6$ more collecting area (see Equation 12). This might increase the price per station a little, but would most likely be cheaper than the required correlator and processing costs and probably not affect the overall cost of running the array by very much. To collect the same sky coverage then requires $4 \times 2^{2/3} \sim 6$ beams, at substantially less correlator costs.

It is clear from the above arguments that the best approach to keep computational requirements within limits is to increase $A_{\rm eff}$ (per station) to a level that still probes all k modes of scientific interest within its field of view and to ensure sufficiently good uv-coverage. This most rapidly decreases the noise error on the power spectrum, if station size is not the largest cost-driver. Although a balance might have to be found, it is probably far cheaper to build more collecting area per station and create more station-beams, rather than increase the correlator capacity by an enormous amount to build the same sky from many more visibilities. The former approach also lends itself better to a staged build-out from SKA phase 1 to phase 2, because the processing capacity for multi-beaming could be added later as processing power increases and becomes cheaper.

Hence in summary: *A simple scaling relation shows that improving power spectra measurements benefits far more from a modest increase in collecting area rather than a split of the array in more stations for a fixed collecting area.* The station size is also limited by arguments based on the required field-of-view and uv-coverage (Sect.5.3).

SKA compared to its precursors/pathfinders PAPER, MWA, LOFAR Figure 21 shows the results of a more precise numerical array-sensitivity calculation based on the formalism in McQuinn et al. (2006). We use the latest numbers in the literature for PAPER, MWA and LOFAR and compare the results to different array configurations for SKA. Table 5.2.1 lists the parameters used. The formalism in McQuinn et al. (2006) reproduces Equation 11 exactly for the same assumptions and the same scaling relations. To properly compare the different arrays, we take $k = 0.1$ cMpc^{-1} as the reference point where to compare sensitivities.

PAPER and MWA: We find that the current array-configurations of PAPER and MWA perform equally well, even though PAPER has a smaller collecting area ($A_{\rm coll}$) than MWA and a similar number of stations. The lower collecting area of PAPER is compensated by making the array even more compact than MWA, hence lowering $A_{\rm core}$. Equation 12 shows that this improves the power spectrum sensitivity of the array. In addition, PAPER gains sensitivity by having a somewhat smaller $A_{\rm eff}$, since only single dipoles are used rather than tiles. Overall this results in PAPER and MWA having similar sensitivities to the power spectrum. Both PAPER and MWA are able to probe only the smallest k modes, because of their compact configurations. We note however that the expected

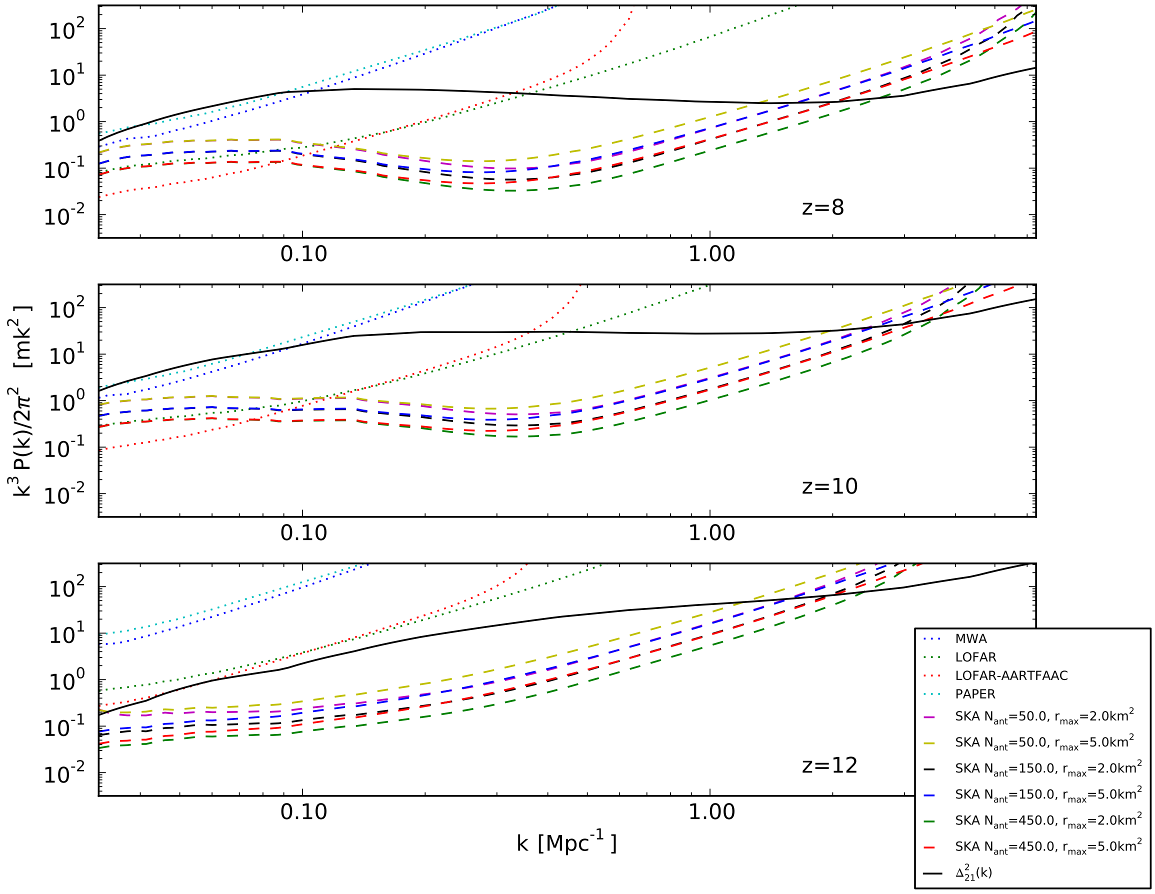

Fig. 21 Comparison of current arrays, PAPER, MWA and LOFAR, with SKA, assuming B=10 MHz, $t_{\rm int} = 1000$ hrs and $\Delta k = k$. For the existing arrays we assumed the latest published (or inferred) specifications, see Table 2. The black line indicates the expected power spectrum of the 21cm power signal.

HI power spectrum drops quite rapidly below k=0.1 cMpc^{-1} (see Figure 21), which mostly offsets the gain in sensitivity. These low k-values also predominantly probe cosmology, rather than the evolution of ionized bubbles (e.g. Zaroubi et al. 2012). Hence shrinking the array helps more than splitting the array if the collecting area is kept fixed, but also shifts the science focus of the array from CD/EoR to cosmology.

LOFAR and LOFAR-AARTFAAC: LOFAR at the same k value has an order of magnitude better sensitivity, as can be seen in Figure 21. This is because LOFAR's collecting area exceeds that of MWA by a factor of ∼10, which yields a factor ∼30 in sensitivity. This more than offsets the factor 2.5 decrease in the number of stations, which increases $\Delta^2_{\rm Noise}$ by a factor ∼1.5. We note that the original MWA design had a four times larger collecting area which made it more equivalent to LOFAR in terms of power spectrum measurements. At lower k values we note that cosmic variance flattens the curves a little making the difference mostly depend on the power spectrum itself and the number of modes being probed. In that case more compact arrays with larger beam-sizes will gain, but not enough to offset the difference. The beam-size of LOFAR is relatively small, and hence the largest scales or smallest k modes ($k < 0.01$ cMpc^{-1}, not shown in Figure 21) cannot be measured well. However, the expected drop in the 21-cm power spectrum on these scales makes these modes inaccessible even for SKA. Probing those very large scales is therefore only possible for SKA if the array is split in extremely small receiver elements, hugely increasing the required correlator and processing capabilities and potentially making it impossible to calibrate the array (e.g. Braun 2013).

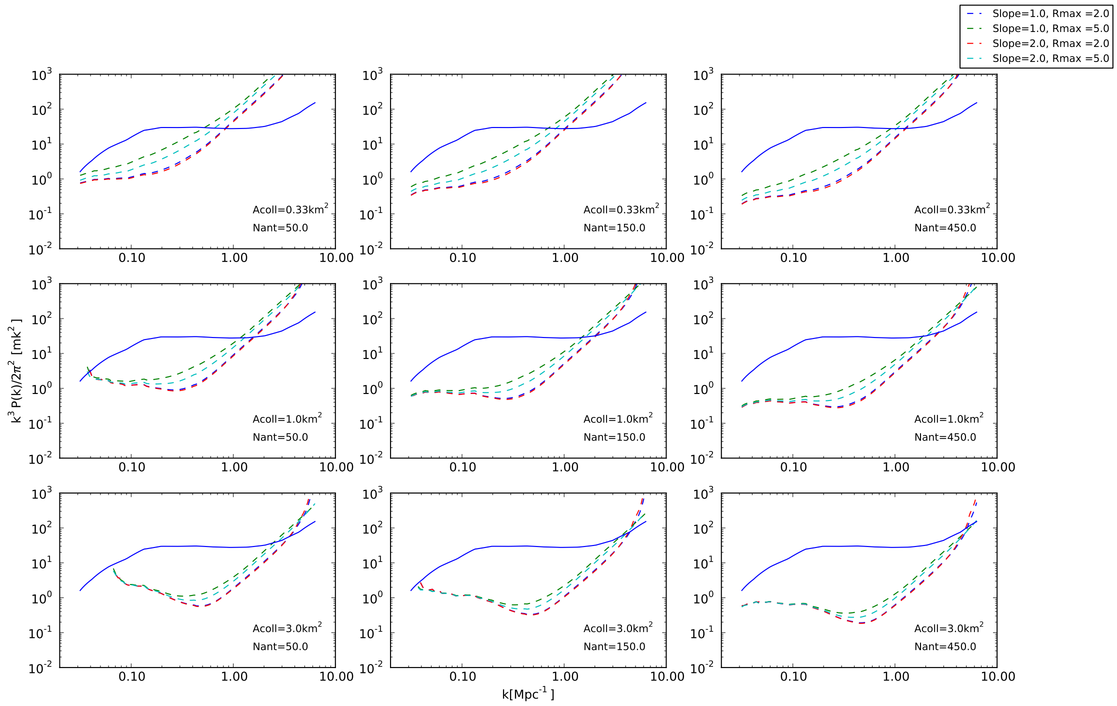

Fig. 22 Comparison different array configurations for SKA, assuming B=10 MHz, $t_{\mathrm{int}} = 1000$ hrs and $\Delta k = k$. Collecting area, number of stations and antenna distribution are varied. The blue line indicates the expected power spectrum of the 21cm signal.

We have also calculated the power spectrum sensitivity of the AARTFAAC system (e.g. Prasad & Wijnholds 2012). This addition to LOFAR allows all 288 tiles/dipoles of the superterp station in the inner 300 m core to be cross-correlated and is currently being implemented. AARTFAAC can improve the performance of LOFAR on scales $k < 0.2$ cMpc^{-1} by a factor of five *if* it can be properly calibrated. We note that such a hybrid array could be considered for SKA as well to boost its power-spectrum capabilities.

SKA: Finally, Figures 21 and 22 show the sensitivity of SKA itself, varying A_{coll}, N_{stat} and also A_{core} (by varying the core radius r_{max}) and the distribution of the visibilities. Whereas the latter seems to have little impact, we note two things: (i) one gains about a factor of $\sim$3 in sensitivity by going from 50 to 450 stations, as expected for a fixed k-mode. (ii) Small values of k can be probed only for smaller station sizes as expected, but as previously mentioned this requires an increased correlator capacity. (iii) Below $k < 0.1$ cMpc^{-1}, curves of similar beam size (i.e. number of stations) but different core areas converge, suggesting that on larger scales the noise error is negligible and sample variance dominates at redshifts below 10; above that redshift the sky is much brighter and the noise error dominates also on large scales. None of the current arrays is in that regime. (iv) Over the full range, a more compact array (i.e. two versus five km radius) performs better. Building a more extended core ($>$ 2 km) is therefore not required for power spectrum analysis. Longer baselines of course remain important for sky modeling, calibration, etc.

5.2.2 Tomography/imaging

When considering power spectrum measurement, we saw that the collecting area, core area, and station sizes have varying levels of impact on improving the power spectrum sensitivity.

Tomography is helped most by increasing the total collecting area on a given angular scale, since increasing the number of modes (by increasing the beam size) does not help. These structures cannot be imaged (except on very large scales) by using massive redundancy of baselines as is done with extremely compact arrays that only focus on the 21cm power-spectrum detection. Such compact arrays are incapable of imaging structures on scales of a few arcminutes, which requires at least baselines of a few kilometers. Obtaining substantial sensitivity on

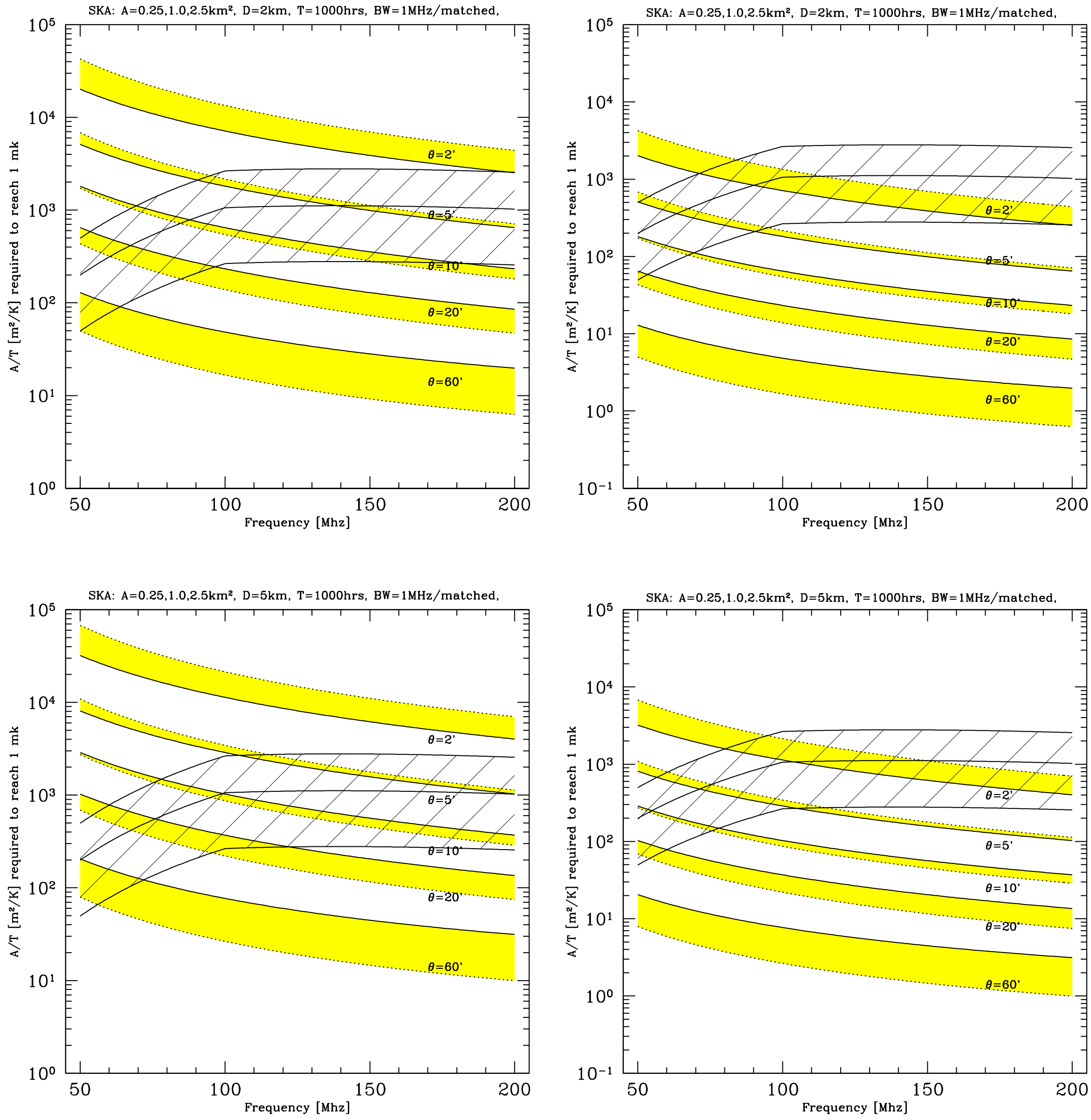

Fig. 23 Shown are the A/T requirements for SKA to reach 1 mK (left) or 10 mK (right), respectively, in 1000 hrs of integration and using a BW of 1 MHz/matched (solid/dashed declining lines). Top/bottom rows show arrays with a core diameter of 2 and 5 km, respectively. The rising-flat dashed region indicates an SKA with a 1 km^2 (center), 0.25 km^2 (lower), 2.5 km^2 (upper) physical collecting area, respectively, and an optimal frequency of 100 MHz. If the A/T requirement fall below this line for angular scales of 2, 5, 10, 20 and 60 arc minutes (top to bottom), then tomography at that angular scale can be done in 1000 hr to that level rms.

those baselines therefore requires spreading stations/receivers over a wider area, which goes somewhat against the requirements for power spectrum measurement.

To illustrate the required tomographic sensitivity for SKA-1&2, we use two different criteria both set by the science requirement discussed in Sect.3 of this white paper:

- *Tomography to a $\delta T_b = 1$ mK level on a few arcmin scales, required to map out hydrogen brightness temperature fluctuations in the IGM over cosmic time during the cosmic dawn and epoch of reionization.*
- *Tomography to $\delta T_b = 10$ mK level over many arcmin scales to map out ionized bubbles during the Epoch of Reionization.*

The first criterium is already a requirement in the Design Mission Reference (DRM) of SKA and is set by the expected HI brightness temperature features during the Cosmic Dawn and Epoch of Reionization inside neutral patches (see Section 3.2). During the later phases of the EoR, neutral hydrogen is being progressively ionized in bubbles/patches around star forming galaxies. Because the hydrogen total intensity signal is $\sim$30 mK, these patches have a much larger contrast than HI fluctuations inside neutral patches (see e.g. Zaroubi et al. 2012, for a discussion). In fact, they will be observed as 'holes' in the sky by an interferometer.

Again we assume an array with a physical collecting area of 1 km^2, an integration time of 1000 hrs for either a fixed bandwidth of 1 MHz or a bandwidth that matches the spatial resolution. We assume baseline distribution of R^{-1} inside a 2 or 5 km diameter core. This distribution roughly matches the baseline distribution that we assumed for the power spectrum analysis, over an order of magnitude (from $|u| \sim 10^2 - 10^3$). The station size is not relevant as long as the scales of interest are below the size of the station beam. In addition, we assume an optimal frequency above which the array becomes sparse ($\propto (\nu_{\rm opt}/\nu)^2$) for $\nu_{\rm opt} = 100$ MHz and $T_{\rm sys} = 100 + 300 \times (150/\nu)^{2.55}$ K.

Because the EoR centers around redshifts $z \approx 10 \pm 4$, we see from Figure 23 (right panels) that such features could be imaged at $\gtrsim 3\sigma$ level on scales of a few arcminutes. If we ask what SKA can do in terms of tomography at the 1 mK level, to which current instruments hope to get with power spectra, one needs to look at Figure 23 (left panels). Scales larger than $5'$ can be reached by an SKA with baselines up to 5 km down to around 50 MHz. At this resolution one can reach 1 mK rms in 1000 hrs at frequencies above 140 MHz, whereas at resolutions of $10'$, $20'$ and $60'$ this is reached at frequencies of 85, 60 and below 50 MHz. *Hence we can map brightness temperature of HI to at least 1 mK on degree scales over all frequencies and redshifts.* Bubbles that have a much higher contrast and probably only occur at lower redshift (higher frequencies) can be imaged on scales of $\sim 2'$ as well, assuming they have 30 mK contrast. At high redshifts large scales dominate and imaging at the tens of arcminute scales can be reached by SKA for the nominal numbers given above.

5.2.3 Longer Baselines

Whereas EoR/CD science will be mostly restricted to short (few-km long) baselines, experience gained with e.g. LOFAR shows that longer baseline are extremely useful and potentially critical to maximize our ability to calibrate the instrument and ionosphere and remove foregrounds (especially compact sources). The deepest images at frequencies corresponding to redshifted 21-cm emission from LOFAR reach in all three cases a level of $\sim$0.1-0.2 mJy rms continuum noise over a bandwidth of 48 MHz on baselines out to several tens of kilometers. To reach this level, directionally-dependent calibration using the longer-baseline data for compact sources was crucial. Reaching this depth, i.e. the thermal noise level, using only the shorter baselines is extremely difficult (see also Braun 2013).

Confusion Noise and FG removal Whereas it is not clear that longer baselines are absolutely critical, having longer baselines substantially reduces the computational effort of calibrating the instrument, because the sky-model on these baselines consists of mostly compact, rather than extended sources and confusion is substantially reduced (confusion noise on the shorter baselines is a few mJy, much larger than the thermal noise). Compact sources can more easily be removed using these longer baselines without impacting the science done on shorter baselines.

Directionally dependent instrument calibration One other issue, mostly neglected in the literature, is that the amount of information contained on larger baselines in general is larger than on the shorter baselines, which are heavily redundant. The independent information that we can maximally obtain per time-stamp is the number of independent resolution elements in uv-ν space. In case of otherwise similar arrays, the one with on average much shorter baselines will have a higher level of redundancy and therefore fewer independent data-point that can be used for calibration purposes, while at the same time reaching a higher signal-to-noise ratio per mode (by having more visibilities per resolution element). Calibrating on shorter baselines also requires a far more extended and complex sky-model (i.e. including the MW foreground, rather that mostly bright compact sources), which quite easily leads to larger calibration errors. Finally, bias is increased if the non-linearity in the models is large and/or the S/N ratio is small (e.g. Cook et al. 1986). The latter is still under-appreciated in the current literature on calibration, but it is a well-known effect in ML-statistics in cases of low S/N ratio and strong model covariance.

Ionospheric corrections In addition to instrument calibration, longer baselines also allow for an easier modeling of the three-dimensional ionosphere above the array. Just as for instrument calibration, it is far easier to model the ionosphere using long baselines where its effects are more clearly visible (either because compact sources move and distort through refractive effects, or break up through diffractive effects). Applying long-baseline ionospheric solutions to the shorter baselines through proper model projection, has – in the case of LOFAR – further simplified the modeling. Despite this, it remains difficult to correct for the ionosphere, but it is hard to imagine how stable ionospheric solutions can be obtained with only short baselines.

All of this suggest that long baselines, although not proven to be absolutely essential, substantially help in correcting deep integrations for (i) compact FG source removal, (ii) calibration of the instrument on simple compact bright calibrators and (iii) visualize and correct for ionospheric and directionally-dependent beam effects. Geometric arguments show that baselines needed for ionospheric calibration should be as large as the imprint of the FoV at the height of the ionosphere. This is roughly 25 km per 5° FWHM FoV for an ionosphere at 300 km height.

5.2.4 Power spectra versus Tomography

There could potentially be a conflict between the two strategies for the baseline distribution discussed in the previous sections: sensitivity for power spectra naively drives one toward more compact arrays (e.g. MWA and PAPER), whereas tomography of EoR bubbles and structure requires baselines that can image on scales of a few arcminutes. As we saw, tomography benefits from an increase in collecting area, whereas, for a fixed number of stations, such an increase has little impact on the power spectra. The small k-modes will be sample-variance dominated, so improvement can only come from an increase in the FoV. However, increasing the collecting area by making the stations larger will actually reduce the FoV.

In Figures 24–27, we summarize the sensitivity of different array configurations and compare these to the requirements from both tomography and power-spectrum determination. We conclude that for tomography at least a collecting area of 0.5–1 km^2 is required for a nominal 1000hr integration time, whereas the power-spectrum measurements require a number of stations of at least a few hundred (i.e. station sizes smaller than $\lesssim$50 meter), otherwise SKA could perform even worse in power spectrum measurements than its current precursors that have much smaller collecting areas but also smaller stations (i.e. large fields of view). In all instances, SKA will be substantially better at tomography because of its superior sensitivity per spatial resolution element.

The “sweet-spot” is therefore, as expected based on the the original conception of the SKA, that at least a collecting area approaching 1 square kilometer is required, but also that station sizes should be relatively small (i.e. $\lesssim$50m) compared to the 180 m that is currently often mentioned in SKA documentation. A too small field of view is detrimental for power-spectrum measurements (see also Sect.5.3 for an more extensive discussion on the issues of field-of-view). How small stations really can become depends on correlator costs and calibratability which might be an issue for the current smallest SKA pathfinders such as MWA and PAPER, but also for LOFAR (see Braun 2013).

5.3 Instantaneous Field-of-View and Multi-beaming

The minimum field of view (i.e. that of the station beam) of SKA should be set by the largest scale of the HI brightness temperature fluctuations that is of interest (or conceivably possible to measure) over the redshift/frequency range indicated in the previous sections (e.g. Sect.4.1). The reason is that most of the information on scales exceeding this beam size is lost and can only partly (if at all) be recovered by multi-beaming or mosaicking in the image or uv-space. This requires deconvolution of the uv-data, however, which is computationally expensive and leads to large uncertainties and errors if the beam-shape is not well known. If the largest relevant scales are not contained in the station beam, they will thus mostly be inaccessible, both for tomography and power spectrum measurements. As we showed Section 4.1, it is important to reach scales of order a few degrees.

Building up an equivalent area of the sky through multi-beaming does not provide the same image or information as when observing it with a single equivalently-large beam. Scales larger than the individual station beams are effectively lost or highly uncertain when recovered.

The largest possible scale of interest should therefore fit well inside the beam size, such that beam uncertainties do not play a major role. This scale is around a few degrees and corresponds roughly to $k \sim 0.01$ Mpc^{-1}. This scale is of interest at redshifts of $\gtrsim$ 12, which corresponds roughly to 100 MHz. Hence, if the optimal frequency of the array is chosen at this frequency, a 5 degree station beam size at this frequency should be sufficient to cover all scales of interest for redshifts larger than $z \sim 12$, where the beam size increases. This implies a station size of

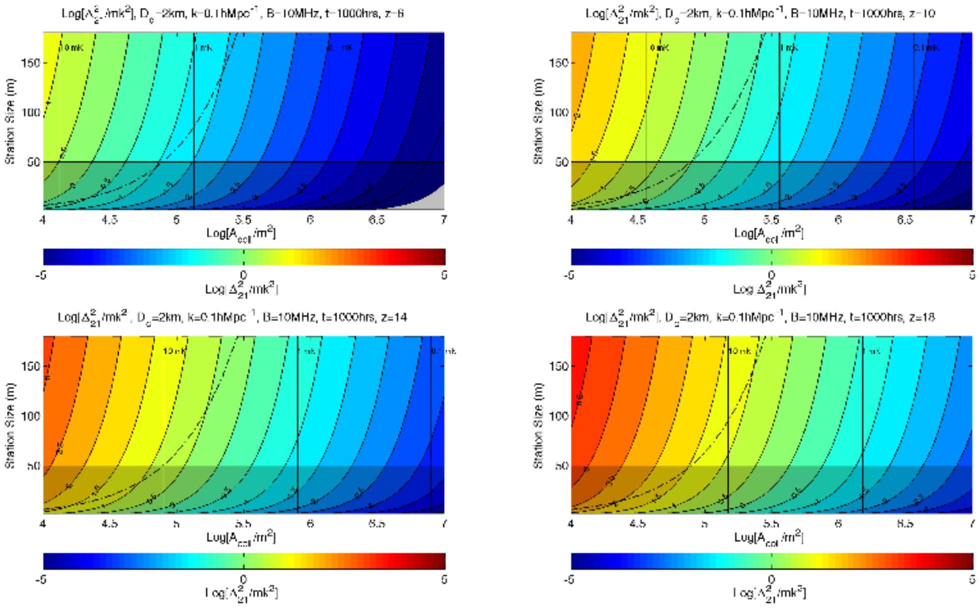

Fig. 24 Shown are the power spectrum and tomographic sensitivity for $k = 0.1$ hMpc^{-1} as described in Eqn.11 for an array of diameter of 2 km with a constant visibility density, for a range of collecting areas, station diameters and redshifts. An integration time of 1000 hrs is assumed and a bandwidth of 10 MHz for the power spectrum determination. For tomography (vertical lines of constant collecting area) a bandwidth matching the k-scales at that redshift is assumed. The dashed line indicates the demarkation below which the instantaneous uv-coverage has a filling factor of order unity. The gray box demarcates the region for which the field-of-view of the array exceed the required ∼5 degrees at 100 MHz.

roughly $\lesssim$35 meters. Within the beam also a sufficient number of k-modes (∼100) can be measured to reduce the sample variance below ∼ 3% per beam (Sect.4.1). Multi-beaming could reduce this sample variance further.

Below this redshift, the amplitude of the power spectrum on these large angular scales rapidly decreases and the dominant k-modes are on arcminute to tens of arcminutes scales. These scales also easily fit within the beam even at the highest frequencies (lower redshifts) of around 200 MHz where the beam size would reduce to $\gtrsim$2.5 degrees for station sizes ∼ 35m. A beam size of ∼10 degrees at ∼50 MHz, ∼5 degrees at ∼100 MHz and ∼2.5 degrees at ∼200 MHz therefore seems sufficient to image all possible scales of interest over the full frequency/redshift range (say 50–200 MHz).

The required station size of around 35 meters or less, is substantially smaller than the 180 meter station currently proposed for SKA in phase 1. The latter stations would preclude the detection of the largest scale modes at all redshifts, effectively excluding high-z cosmology and EoR studies. Many extremely interesting physics phenomena (e.g. bulk-flows, etc) are occurring at the degree scale [10]

At the same time, there is no need to go to stations much smaller than ∼ 35 meters. For mapping scales larger than the station beam, multi-beaming can be used. These images will not contain structures larger than the beam-size, for example from the Milky Way (the greatest contaminant in EoR studies), but they will provide a complete census of the EoR and Cosmic Dawn without substantial loss of information. We note that mosaicking either in image or uv-space is considerably cheaper computationally than cross-correlating all elements and producing images on scales far exceeding 5 degrees, since no CD/EoR-relevant science is expected on these scales.

5.3.1 Global Signal Requirements

The problem of measuring the global 21cm signal is one of bandpass calibration of instrument gain and receiver temperature, and not of collecting area or thermal noise. In theory, a single well calibrated dipole can build up the required signal to noise ratio within a day. While single antenna experiments have put interesting constraints on

---

[10] We note that somewhat larger beams might be ok (station size perhaps up to 70 meters) with multi-beaming and uv-plane dithering but this will require careful thinking about how to connect these multi-beamed data into a single power spectrum in overlapping areas. It can best be done in the uv-plane by combining the visibilities brought to a common phase-center. Also a hybrid system where only a sub-set of receiver elements inside stations are beam-formed and correlated could be considered.

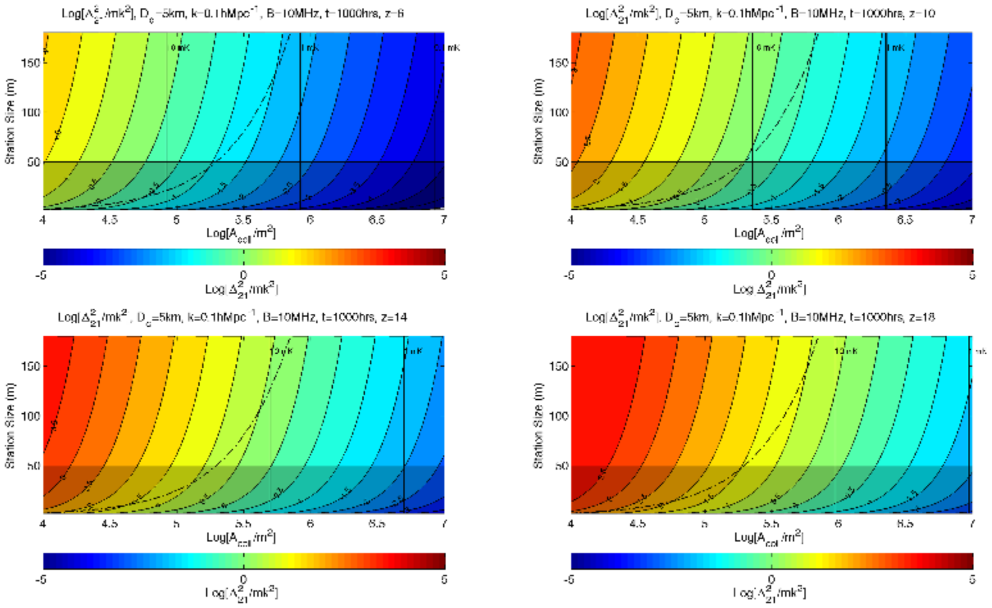

Fig. 25 Idem as Fig.24 for an array of 5-km diameter.

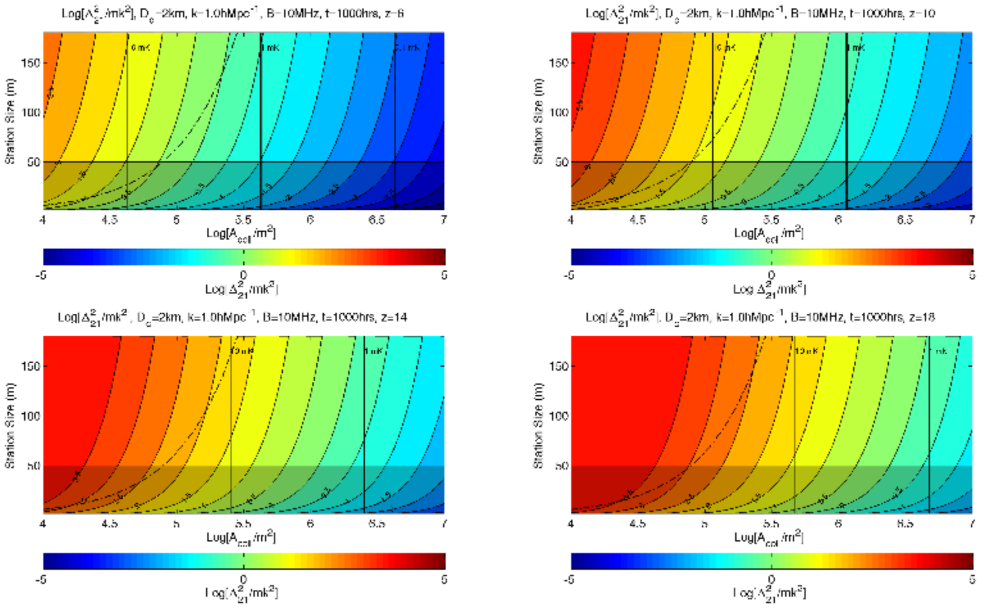

Fig. 26 Idem as Fig.24 for an array of 2-km diameter and $k = 1$ hMpc^{-1}.

the global 21cm signal (Bowman & Rogers 2010), in practice they suffer from systematic errors introduced by the frequency dependent instrument response. Having an antenna element as part of an interferometric array such as SKA provides significantly better constraints on bandpass gain calibration and estimation of frequency dependent antenna element beam. Moreover an array environment facilitates better algorithms for RFI detection, provides information on ionospheric and multipath conditions for assessment of data quality and facilitates foreground subtraction using interferometric sky images.

Cross-correlations (or visibilities) measured by an interferometer are not sensitive to a global signal, as the global signal has significant power only at the origin of the *uv*-plane (zero baseline). On the other hand, the autocorrelations of elements in an array provide a zero baseline measurement, contain the global signal power and

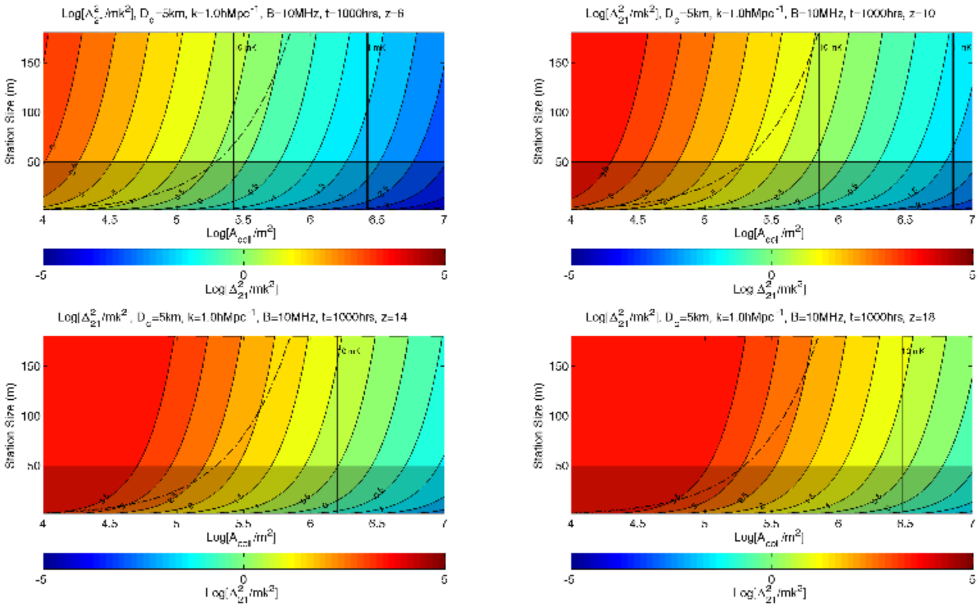

Fig. 27 Idem as Fig.24 for an array of 5-km diameter and $k = 1$ hMpc^{-1}.

receiver noise (the receiver noise drops off in non-zero baseline visibilities) which has to be modeled in addition to the instrumental gain. This has traditionally been achieved by switching between the sky and a calibrated noise source. Therefore, using antenna elements that are both part of an array and have calibrated noise injection have the potential to significantly reduce systematic errors.

Another possible approach to detect the global 21cm signal involves blocking a significant portion of the instrument field of view with an obstacle such as the moon (or even a man-made structure). This creates a hole in the otherwise uniform global signal and couples power into the visibilities (cross correlations) even on non-zero baselines. This technique enables measurement of a global signal without using the auto correlations and hence does not need switching between the sky and a calibrated noise source. However, it is still in its infancy (Briggs et al. in prep.).

There are several current efforts attempting a global signal measurement. EDGES (single dipole) targets the decline of the HI signal through reionization. New concept experiments are attempting a detection of the expected absorption trough at ~70 MHz where the first luminous structures were formed: array based observations with LOFAR-LBA stations (Harish & Koopmans in prep.), observations with the Long Wavelength Array (LWA) in beam forming mode (Bowman priv. comm.), observations with the Large-aperture Experiment to detect the Dark Ages (LEDA, Greenhill & Bernardi 2012) and Dark Ages Radio Explorer (DARE, Burns et al. 2012; Harker et al. 2012) - a proposed single dipole space mission.

Due to its less demanding requirement on collecting area and number of stations, a global 21cm measurement has the potential to generate early science for the SKA during its commissioning phase. Successful measurement of the global signal also has a potential to establish the reionization redshift range accurately for future SKA tomography experiments. A global signal experiment will also provide useful benchmarks on the calibratability of the instrument's frequency response. To facilitate a global signal measurement with the SKA, it is desirable to have calibrated noise injection on at least a few antenna elements. These antenna elements may be dipoles that are physically apart from the SKA stations. Furthermore, to measure the full evolution of the global signal, a frequency coverage of ~ 40 to 200 MHz is desirable.

5.3.2 Beam-size and calibration

Apart from the science requirements, there are also calibration issues that need to be considered in the choice of beam size as recently worked out in great detail by Braun (2013). A larger beam size requires more directionally dependent solutions (for e.g. the ionosphere, beam shape, etc). Multiple smaller beams in that case have the advantage that they can be flexibly distributed over the beam of the smallest (non beam-formed) receiver element of the station, allowing for example bright calibrators to be placed in or near each station beam. This might not be possible for a single large beam if there is an insufficient number bright calibrators in a single contiguous region. A second consideration is related to the ionosphere, which for a wide beam requires a full three-dimensional treatment (e.g. Koopmans 2010). Although this still holds for beams of ∼5 degrees at 100 MHz, modeling the ionosphere for multiple smaller fields will be easier than for a single contiguous wide field, especially at higher resolutions.

We thus conclude that the upper limit on the station size is set by science requirements, whereas the lower limit is mostly set by costs (e.g. correlator, electronics, etc) and the ability to calibrate the instrument. A sweet-spot seems to be around ∼35m, although somewhat smaller and larger sizes could probably be accommodated. We again stress that 180m stations are really detrimental for CD/EoR science because of the tiny instantaneous field of view of such an array and the inability to recover large-scale information on the sky through multi-beaming.

5.3.3 Connection between station size, total collecting area and uv-filling

Finally, the station size (hence beam size) is intimately connected to the instantaneous *uv* filling. For a fixed physical station size $D_{\rm stat}$ inside a core diameter of $D_{\rm core}$, it is easy to show that for a fully non-redundant array the requirement for the minimum number of station to acquire full instantaneous *uv*-coverage is

$$N_{\rm stat} \geq D_{\rm core}/D_{\rm stat}.$$

For say $D_{\rm core} = 2\,{\rm km}$ and $D_{\rm stat} = 35\,{\rm m}$ the minimum number of stations would be at least $\gtrsim$60 and fewer for larger stations. Very large stations only lead to good instantaneous *uv*-coverage for a smaller core area, if the total collecting area is fixed, which goes at the cost of losing resolution in tomography (again emphasizing the sometimes conflicting power spectra and tomography requirements). Note that such an array will have a collecting area of

$$A_{\rm coll} = D_{\rm core}/D_{\rm stat} \times \pi(D_{\rm stat}/4)^2 = (\pi/4)D_{\rm core} \times D_{\rm stat}.$$

For 60 stations of size 35 m this yields 60,000 $\rm m^2$, similar to LOFAR, which is insufficient for most of the SKA CD/EoR science requirements. For such stations the collecting area requirement automatically leads to a well filled *uv*-plan. Hence there is friction between instantaneous *uv*-coverage, core collecting area and station size. To have the required station beam size of at least 5 degrees at 100 MHz one simply needs stations that are not too large. This requires many more stations than for 180-m size stations for example, but would satisfy the instantaneous *uv*-coverage criterium. Even if the latter is not critical, to satisfy the A/T requirements of SKA more smaller stations are strongly preferred, even required, over a smaller number of larger stations. This is particularly true if they are distributed over a core area with a diameter of 2-5 km although this can be alleviated if the core area is made smaller. Since tomography on scales corresponding to 5 km baselines will be very hard, a smaller core area (∼ 2 km) might be the best option possibly with most of the stations within a few km core area. We note that this statement is independent of the use of longer baselines for calibration purposes.

6 Recommendations

In this section, we summarize succinctly our recommendations for an optimal SKA array configuration for CD/EoR science requirements.

6.1 Choosing an optimal and affordable SKA CD/EoR array

We conclude that the best strategy for designing an SKA array optimized for EoR/CD science is: (1) Set the largest scale one would like to probe and match the station size to that requirement; additional sky area is then build up via multi-beaming (which will provide more samples, but no data for scales larger than the FoV) (2) Scale the core area to an area that can probe all power-spectrum *k*-modes of interest *and* still enable tomography (i.e. imaging) on the smallest angular scales probed by $k_\perp$ which require somewhat larger baselines. (3) Set the number of stations or collecting area (since the station size has now been fixed) to reach the required tomography and power spectrum sensitivity level and use multi-beaming to reduce sample variance. We note that in phase-1 one might start with a more compact array with some longer baselines, and during phase-2 extend the core further, as well as add more long baselines. An initial very compact array however would not allow tomography on small (arminute) spatial scales.

6.2 Towards an optimal reference design

A reference design that satisfies all criteria for power spectrum determination and tomography from arc minute to degrees scales would be the following for SKA-1 and 2[11]:

1. An absolute minimal frequency range 54–190 MHz; an optimal frequency range 54–215 MHz and a wide frequency range of 40–240 MHz; The latter frequency range fully covers the Cosmic Dawn and EoR eras for all currently conceivable scenarios, whereas the first one is the most narrow 3.5:1 range that a single dipole receiver element can cover with more than 10% efficiency over the entire bandwidth[12]. A full frequency coverage (40–240 MHz) would argue for a dual-band receiver system at the lowest frequencies.
2. A frequency resolution of $\sim$100 KHz suffices for power-spectra and tomography studies since it is well below the spatial scales that can conceivably be measured by SKA. A much higher resolution of $\sim$1 KHz, however, is required for neutral HI absorption line studies to resolve very narrow (i.e. low-velocity dispersion) lines and for RFI excision.
3. A physical collecting area $A_{\rm coll} \gtrsim 1\,{\rm km}^2 \times (\nu_{\rm opt}/100{\rm MHz})^{-2}$ for $\nu_{\rm opt} < 100$ MHz and at least 1 km^2 for $\nu_{\rm opt} \geq 100$ MHz. This collecting area ensures sensitivities of $\gtrsim$ 1 mK on scales of $\gtrsim$ 5 arc minutes (with matching bandwidths) over the entire redshift range of the SKA-low, sufficient to accomplish most science goals in 1000 hrs of observing time.
4. An optimal frequency ($\nu_{\rm opt}$; corresponding to a $\lambda/2$ size of a receiver dipole) around 100 MHz, but possibly lower with increasing physical collecting area to compensate for loss in effective collecting area (see item above) if the size of the receiver element is not a major cost driver and if station-beam side lobes can be suppressed sufficiently by placing them in a semi-random pattern.
5. A core area with a diameter of $\lesssim$ 5 km with most collecting area ($\sim$75%) inside the inner 2 km for power-spectrum and large-scale tomography studies, plus baselines out to 5 km for arcminute-scale (i.e. EoR bubble) tomography. This is in line with current ideas on the layout of the SKA core area. The total core collecting area should be at least that given in item -3-.
6. A set of longer baselines ($\sim$ 10–20% of the core collecting area) up to $\sim$100 km for calibration, ionospheric modeling[13] and for building a detailed sky model. SKA-pathfinders (in particular LOFAR) show that many image artifacts are due to errors in the subtraction of bright compact sources and the ionosphere and both benefit tremendously from the use of longer baselines to model the sky and the ionosphere.
7. A station size of order $\sim$35 m which corresponds to a 2.5–10 degree field-of-view from 200 MHz down to 50 MHz, which covers all (known) scales of interest. We propose that multi-beaming can be used to cover larger areas of the sky simultaneously and reduce sample variance in power-spectrum studies. A very small station size is likely more costly and harder to calibrate and a much larger station would be detrimental for the science case.

The proposed basic SKA-low array design allows most CD/EoR science goals, described in this white paper, to be reached in 1000 hrs of observing time, but undoubtedly will raise many new and groundbreaking scientific questions as well. We note that many of the requirements are already part of the DRM of SKA. However, we also propose a number of clear differences: We argue for

(i) a wider (and lower) frequency range, going well below the 70 MHz envisioned for SKA-1. This could potentially argue for the use of a dual-band receiver system.
(ii) a smaller station size of $\sim$35 m, compared to the $\sim$180 m currently envisioned for SKA-1, to ensure that *all* scales of interest easily fit within a single station beam,

---

[11] We recognize that more details need to be worked out especially on costs and calibratability of the array, but as far as we are aware this array design does not have major show stoppers and could be used as a starting point for a more detailed design.

[12] These ranges have been argued for as well in the Memo "Is There an Optimum Frequency Range for SKA1-lo? Question 1 of the Magnicent Memoranda II" by Huynh et al.

[13] These baselines exceed the imprint of the station beam on the ionosphere and larger beam-sizes therefore require longer baselines, somewhat counterintuitively.

(iii) the use of longer baselines out to tens of kilometers for instrument/ionosphere calibration and sky-modeling purposes.

7 Summary

This White Paper summarizes some of the exciting scientific prospects of studying the Cosmic Dawn (CD) and Epoch of Reionization (EoR) through the redshifted 21-cm emission line, in particularly focussing on prospects for the Square Kilometre Array (SKA) and how science goals translate in to a basic reference design that allow these science goals to be reached. We focus not only power-spectrum measurements, which are driving all current EoR pathfinder telescopes (e.g. GMRT, PAPER, MWA, LOFAR), but also, and more importantly, on imaging/tomography of the Cosmic Dawn and Epoch of Reionization. Whereas the basic reference design that we propose is relatively close to that proposed in many SKA documents and memos, it deviates in a few instances. The most of important are (a) a frequency coverage extending to lower frequencies / higher redshifts than previously envisaged, driven mostly by improved knowledge since 2004 (when the SKA Science Case was written) of when reionization occurred and what physics plays a role and (b) a station size being substantially smaller than the currently proposed sizes for SKA 1 and/or 2, but substantially larger than the single receiver elements that also have been suggested (e.g. HERA). A smaller station size is driven mostly by the need to cover the largest relevant angular scales for both power spectrum analysis and imaging/tomography in the instantaneous FoV while keeping the correlator costs as low as possible. Multi-beaming can be used to increase the sampling of the scales captured in one beam. Whereas we regard this manuscript as a living document which, using input from the community, will be updated as our understanding progresses, we view this first version as a starting point for a realistic SKA-low array for CD/EoR studies.

The SKA is expected to revolutionize the studies of the earliest phases of star and galaxy formation in the Universe. Whereas precursors can only probe the power spectrum of the 21cm signal from the Epoch of Reionization, SKA will allow tomography of most, if not the entire, period, on scales which will allow us to follow the growth of ionized regions from initially small to large. At the same time, SKA will also for the first time explore the earlier phases of the Cosmic Dawn, before substantial reionization, probably mostly in a statistical way, but possibly also with low resolution tomography. These studies will teach us fundamentally new things about both the earliest phases of star and galaxy formation, as well as cosmology and even have the potential to lead to the discovery of new physical phenomena.

The 21cm signal from neutral hydrogen can be analyzed in different ways. Imaging at different frequencies will give us a tomographic volume with both spatial and evolutionary information. These data sets can be analyzed to characterize the sizes and shapes of ionized regions, as well as the density structures in still neutral regions. This information can also be combined with other probes of the EoR/CD, such as galaxy and QSO surveys, and the different types of background radiation (NIRB, atomic & molecular lines, CMB), allowing us to make the connection between the properties of the galaxies and the effect they have on the IGM.

Analysis of the power spectrum of the 21cm signal will characterize the relevant length scales, as well as provide fundamental cosmological information through the analysis of the redshift space distortions. Since the distribution function of the 21cm signal is non-Gaussian, further analysis using higher order statistics will also be used.

The discovery of bright radio sources from the EoR will enable us to study the 21cm forest, giving information about small scale structures in the IGM. Using the auto-correlations of the SKA elements will allow us to extract the evolution of the global 21cm signal, tracing the global rise of star formation and the emergence of X-ray sources during the Cosmic Dawn through to the gradual disappearance of the neutral hydrogen during the EoR.

In order to trace the relevant size scales, fields of view of $\gtrsim 2^\circ$ already at the highest frequencies are required. These fields need to be observed within one observation and cannot be reconstructed from different observations of smaller fields.

The redshifted 21cm signal has to be retrieved from data containing strong foregrounds, mostly galactic, but also extragalactic. In order to minimize the effects of foregrounds, the observed fields should be located in areas of low foreground emission and without strong polarization features. The techniques for foreground subtraction will be put to the test on the data from SKA precursors in the coming years.

Additional complications to deal with are radio frequency interference (RFI) and effects caused by the ionosphere. Experience with LOFAR shows that even in a radio-loud environment, RFI can be dealt with, provided the telescope has sufficient frequency and time resolution, as well as a sufficient number of ADC bits. Correcting for ionospheric effects will require reconstructing some of the three-dimensional structure of the ionosphere. For this data from long baselines is important.

Since the redshifted 21cm signal is weak and the foregrounds strong, the accuracy of calibration has to be high in order to extract the 21cm signal from the total signal. Apart from dealing with effects caused outside the array, this also puts constraints on the quality of the hard- and software components of SKA. Any effects caused by these components should be small and stable enough to be calibrated out.

The active precursors to SKA-low, namely GMRT, LOFAR, PAPER and MWA, have not yet succeeded in detecting any redshifted 21cm signal. Still, the experiences gained in observing at these low frequencies are important for the development of SKA-low. The coming years will see an increase in the activities of many of these precursors. The expectation is that one or more of the precursors will at least statistically detect a signal from the EoR. It is essential that the experience from these activities will keep finding its way into the SKA project.

To enable the exciting prospects of in depth studies of the Cosmic Dawn and EoR, the low frequency part of SKA needs to be carefully designed to maximize the scientific return. Ideally we should be able to trace to entire CD/EoR period, implying a frequency coverage of 40 – 240 MHz, with an optimal frequency of around 100 MHz. Sacrificing the lower frequency part of this interval will remove the capability to trace the effects of the earliest stars, and lowering the maximum frequency will prevent us from mapping out the last larger neutral patches remaining in the Universe. If a ratio of 6:1 is unattainable, a still acceptable range would be 54 – 215 Mhz (4:1) or 54 – 190 Mhz (3.5:1).

Measuring a power spectrum and performing tomography impose different types of constraints on the design of an interferometer. We propose that the best compromise between the two is to first determine the total collecting area needed for tomography and to then choose the station size needed to capture the relevant angular scales. Imaging requirements of ~ 1 mK sensitivity on scales of a few arcminutes imply a collecting area of $\sim 1\ \mathrm{km}^2$ as has been clear from the inception of SKA.

For the CD/EoR, the largest angular scale to which we have to be sensitive is around 5°. An optimal choice for the station size is therefore around 35 m. It is important to stress that multi-beaming/mosaicking cannot be used to reconstruct information about scales larger than a station beam since this information is not contained in the observations.

Since tomography at angular scales smaller than a few arcminutes is not possible anyway, the large majority of the stations should be distributed over an area with a diameter of about 2–5 km. In addition to this there should be 10–20% much larger baselines which are needed for calibration. Experience with LOFAR has shown that resolving bright objects to angular scales $10\times$ below the scale of arcminutes one is interested in, is essential. These longer baselines are also expected to substantially improve the capabilities to correct for ionospheric distortions. Therefore baselines up to ~ 100 km are required.

To enable 21cm absorption studies against bright sources, a frequency resolution of 1 kHz is required. This resolution is also beneficial for RFI excision. Although the site of SKA-low is characterized by a very low level of RFI, both dealing with the remaining RFI and with the ionospheric effects call for a high frequency resolution, as well as time resolution.

References

Adshead P. J., Furlanetto S. R., 2008, MNRAS, 384, 291
Aghanim N., Majumdar S., Silk J., 2008, Reports on Progress in Physics, 71, 066902
Ahn K., Hong S. E., Park C., Kim J., Iliev I. T., Mellema G., 2010, ArXiv:1008.3914
Ali S. S., Bharadwaj S., Chengalur J. N., 2008, MNRAS, 385, 2166
Alvarez M. A., Komatsu E., Doré O., Shapiro P. R., 2006, ApJ, 647, 840
Baek S., Semelin B., Di Matteo P., Revaz Y., Combes F., 2010, A&A, 523, A4
Barkana R., 2006, MNRAS, 372, 259
Barkana R., Loeb A., 2005a, ApJ, 624, L65
Barkana R., Loeb A., 2005b, ApJ, 626, 1
Barkana R., Loeb A., 2006, MNRAS, 372, L43
Barkana R., Loeb A., 2008, MNRAS, 384, 1069
Basu K., Hernández-Monteagudo C., Sunyaev R. A., 2004, A&A, 416, 447
Bell J. F., Ekers R. D., Bunton J. D., 2000, PASA, 17, 255
Bernardi G. et al., 2009, A&A, 500, 965
Bernardi G. et al., 2010, A&A, 522, A67
Bernardi G., Mitchell D. A., Ord S. M., Greenhill L. J., Pindor B., Wayth R. B., Wyithe J. S. B., 2011, MNRAS, 413, 411

Bertone G., Hooper D., Silk J., 2005, Phys. Rep., 405, 279

Bharadwaj S., Ali S. S., 2004, MNRAS, 352, 142

Boonstra A. J., Weber R., Colom P., 2009, in ”Proceedings of Wide Field Astronomy & Technology for the Square Kilometre Array (SKADS 2009). 4-6 November 2009. Chateau de Limelette, Belgium. Published online at http://pos.sissa.it/cgi-bin/reader/conf.cgi?confid=132

Bourgois G., 1981, A&A, 102, 212

Bouwens R. J. et al., 2011, Nature, 469, 504

Bouwens R. J. et al., 2010, ApJ, 709, L133

Bouwens R. J. et al., 2012, ApJ, 752, L5

Bowman J. D., Morales M. F., Hewitt J. N., 2006, ApJ, 638, 20

Bowman J. D., Morales M. F., Hewitt J. N., 2007, ApJ, 661, 1

Bowman J. D., Rogers A. E. E., 2010, Nature, 468, 796

Boyle B. J., Shanks T., Croom S. M., Smith R. J., Miller L., Loaring N., Heymans C., 2000, MNRAS, 317, 1014

Brandenberger R. H., Danos R. J., Hernández O. F., Holder G. P., 2010, J. Cosmology Astropart. Phys., 12, 28

Braun R., 2013, A&A, 551, A91

Bunker A. J. et al., 2010, MNRAS, 409, 855

Burns J. O. et al., 2012, Advances in Space Research, 49, 433

Carilli C. L., 2011, ApJ, 730, L30

Carilli C. L., Gnedin N. Y., Owen F., 2002, ApJ, 577, 22

Carilli C. L. et al., 2010, ApJ, 714, 834

Carilli C. L., Wang R., van Hoven M. B., Dwarakanath K., Chengalur J. N., Wyithe S., 2007, AJ, 133, 2841

Chapman E. et al., 2013, MNRAS, 429, 165

Chapman E. et al., 2012, MNRAS, 423, 2518

Chuzhoy L., Alvarez M. A., Shapiro P. R., 2006, ApJ, 648, L1

Chuzhoy L., Shapiro P. R., 2006, ApJ, 651, 1

Ciardi B., Bolton J. S., Maselli A., Graziani L., 2012, MNRAS, 423, 558

Ciardi B., Ferrara A., 2005, Space Sci. Rev., 116, 625

Ciardi B. et al., 2013, MNRAS, 428, 1755

Cohen A. S., Röttgering H. J. A., 2009, AJ, 138, 439

Cooray A., 2004, Phys. Rev. D, 70, 063509

Cooray A., Gong Y., Smidt J., Santos M. G., 2012a, ApJ, 756, 92

Cooray A. et al., 2012b, Nature, 490, 514

Cristiani S. et al., 2004, ApJ, 600, L119

Datta K. K., Choudhury T. R., Bharadwaj S., 2007, MNRAS, 378, 119

Datta K. K., Friedrich M. M., Mellema G., Iliev I. T., Shapiro P. R., 2012a, MNRAS, 424, 762

Datta K. K., Majumdar S., Bharadwaj S., Choudhury T. R., 2008, MNRAS, 391, 1900

Datta K. K., Mellema G., Mao Y., Iliev I. T., Shapiro P. R., Ahn K., 2012b, MNRAS, 424, 1877

de Oliveira-Costa A., Tegmark M., Gaensler B. M., Jonas J., Landecker T. L., Reich P., 2008, MNRAS, 388, 247

Di Matteo T., Ciardi B., Miniati F., 2004, MNRAS, 355, 1053

Doré O., Holder G., Alvarez M., Iliev I. T., Mellema G., Pen U.-L., Shapiro P. R., 2007, Phys. Rev. D, 76, 043002

Dunkley J., et al., 2011, ApJ, 739, 52

Dvorkin C., Hu W., Smith K. M., 2009, Phys. Rev. D, 79, 107302

Eisenstein D. J. et al., 2011, AJ, 142, 72

Ellis R. S. et al., 2013, ApJ, 763, L7

Fan X. et al., 2006, AJ, 132, 117

Fernandez E. R., Iliev I. T., Komatsu E., Shapiro P. R., 2012, ApJ, 750, 20

Fernandez E. R., Komatsu E., Iliev I. T., Shapiro P. R., 2010, ApJ, 710, 1089

Fialkov A., Barkana R., Tseliakhovich D., Hirata C. M., 2012, MNRAS, 424, 1335

Field G. B., 1959, ApJ, 129, 551

Fowler J. W. et al., 2010, ApJ, 722, 1148

Fridman P. A., Baan W. A., 2001, A&A, 378, 327

Friedrich M. M., Mellema G., Alvarez M. A., Shapiro P. R., Iliev I. T., 2011, MNRAS, 413, 1353

Furlanetto S. R., 2006a, MNRAS, 370, 1867

Furlanetto S. R., 2006b, MNRAS, 371, 867

Furlanetto S. R., Loeb A., 2002, ApJ, 579, 1

Furlanetto S. R., Oh S. P., Briggs F. H., 2006a, Phys. Rep., 433, 181

Furlanetto S. R., Oh S. P., Pierpaoli E., 2006b, Phys. Rev. D, 74, 103502

Furlanetto S. R., Zaldarriaga M., Hernquist L., 2004, ApJ, 613, 1

Galli S., Iocco F., Bertone G., Melchiorri A., 2009, Phys. Rev. D, 80, 023505

Geil P. M., Gaensler B. M., Wyithe J. S. B., 2011, MNRAS, 418, 516

Geil P. M., Wyithe J. S. B., 2008, MNRAS, 386, 1683

Ghosh A., Prasad J., Bharadwaj S., Ali S. S., Chengalur J. N., 2012, MNRAS, 426, 3295

Gleser L., Nusser A., Benson A. J., 2008, MNRAS, 391, 383

Gleser L., Nusser A., Ciardi B., Desjacques V., 2006, MNRAS, 370, 1329

Gluscevic V., Barkana R., 2010, MNRAS, 408, 2373

Gnedin N. Y., Jaffe A. H., 2001, ApJ, 551, 3

Golap K., Shankar N. U., Sachdev S., Dodson R., Sastry C. V., 1998, Journal of Astrophysics and Astronomy, 19, 35

Gong Y., Cooray A., Silva M., Santos M. G., Bock J., Bradford C. M., Zemcov M., 2012, ApJ, 745, 49

Gong Y., Cooray A., Silva M. B., Santos M. G., Lubin P., 2011, ApJ, 728, L46

González-Serrano J. I., Carballo R., Vigotti M., Benn C. R., de Zotti G., Fanti R., Mack K. H., Holt J., 2005, Baltic Astronomy, 14, 374
Gorjian V., Wright E. L., Chary R. R., 2000, ApJ, 536, 550
Greenhill L. J., Bernardi G., 2012, ArXiv:1201.1700
Hales S. E. G., Baldwin J. E., Warner P. J., 1988, MNRAS, 234, 919
Harker G., Pritchard J., Burns J., Bowman J., 2012, in American Astronomical Society Meeting Abstracts, Vol. 219, American Astronomical Society Meeting Abstracts, p. 304.01
Harker G. et al., 2010, MNRAS, 405, 2492
Harker G. et al., 2009a, MNRAS, 397, 1138
Harker G. J. A. et al., 2009b, MNRAS, 393, 1449
Hauser M. G., Dwek E., 2001, ARA&A, 39, 249
Hewish A., 1951, Royal Society of London Proceedings Series A, 209, 81
Hewish A., 1952, Royal Society of London Proceedings Series A, 214, 494
Hirata C. M., 2006, MNRAS, 367, 259
Hui L., Haiman Z., 2003, ApJ, 596, 9
Ichikawa K., Barkana R., Iliev I. T., Mellema G., Shapiro P. R., 2010a, MNRAS, 406, 2521
Ichikawa K., Barkana R., Iliev I. T., Mellema G., Shapiro P. R., 2010b, MNRAS, 406, 2521
Iliev I. T., Mellema G., Pen U., Bond J. R., Shapiro P. R., 2008, MNRAS, 384, 863
Iliev I. T., Mellema G., Pen U.-L., Merz H., Shapiro P. R., Alvarez M. A., 2006, MNRAS, 369, 1625
Iliev I. T., Mellema G., Shapiro P. R., Pen U.-L., Mao Y., Koda J., Ahn K., 2012, MNRAS, 423, 2222
Iliev I. T., Pen U.-L., Bond J. R., Mellema G., Shapiro P. R., 2007, ApJ, 660, 933
Intema H. T., van der Tol S., Cotton W. D., Cohen A. S., van Bemmel I. M., Röttgering H. J. A., 2009, A&A, 501, 1185
Ioka K., Mészáros P., 2005, ApJ, 619, 684
Jackson C., 2005, Publications of the Astronomical Society of Australia, 22, 36
Jelić V. et al., 2010a, MNRAS, 402, 2279
Jelić V., Zaroubi S., Labropoulos P., Bernardi G., de Bruyn A. G., Koopmans L. V. E., 2010b, MNRAS, 409, 1647
Jelić V. et al., 2008, MNRAS, 389, 1319
Jensen H., Laursen P., Mellema G., Iliev I. T., Sommer-Larsen J., Shapiro P. R., 2013, MNRAS, 428, 1366
Jester S., Falcke H., 2009, New A Rev., 53, 1
Joudaki S., Doré O., Ferramacho L., Kaplinghat M., Santos M. G., 2011, Physical Review Letters, 107, 131304
Kashlinsky A., Arendt R. G., Ashby M. L. N., Fazio G. G., Mather J., Moseley S. H., 2012, ApJ, 753, 63
Kashlinsky A., Arendt R. G., Mather J., Moseley S. H., 2005, Nature, 438, 45
Kazemi S., Yatawatta S., Zaroubi S., Lampropoulos P., de Bruyn A. G., Koopmans L. V. E., Noordam J., 2011, MNRAS, 414, 1656
Khatri R., Wandelt B. D., 2007, Physical Review Letters, 98, 111301
Khatri R., Wandelt B. D., 2008, Physical Review Letters, 100, 091302
Knox L., 2006, Phys. Rev. D, 73, 023503
Koopmans L. V. E., 2010, ApJ, 718, 963
Labbé I. et al., 2010, ApJ, 716, L103
Laing R. A., Riley J. M., Longair M. S., 1983, MNRAS, 204, 151
Landecker T. L., Wielebinski R., 1970, Australian Journal of Physics Astrophysical Supplement, 16, 1
Laureijs R. et al., 2011, ArXiv:1110.3193
Lee K., 2009, ArXiv:0902.1530
Lidz A., Furlanetto S. R., Oh S. P., Aguirre J., Chang T.-C., Doré O., Pritchard J. R., 2011, ApJ, 741, 70
Lidz A., Zahn O., Furlanetto S. R., McQuinn M., Hernquist L., Zaldarriaga M., 2009, ApJ, 690, 252
Lidz A., Zahn O., McQuinn M., Zaldarriaga M., Hernquist L., 2008, ApJ, 680, 962
Loeb A., 2009, J. Cosmology Astropart. Phys., 3, 22
Loeb A., Zaldarriaga M., 2004, Physical Review Letters, 92, 211301
Lorenzoni S., Bunker A. J., Wilkins S. M., Stanway E. R., Jarvis M. J., Caruana J., 2011, MNRAS, 414, 1455
Mack K. J., Wesley D. H., 2008, ArXiv:0805.1531
Mack K. J., Wyithe J. S. B., 2012, MNRAS, 425, 2988
Madau P., Meiksin A., Rees M. J., 1997, ApJ, 475, 429
Madau P., Silk J., 2005, MNRAS, 359, L37
Maio U., Koopmans L. V. E., Ciardi B., 2011, MNRAS, 412, L40
Majumdar S., Bharadwaj S., Choudhury T. R., 2012, MNRAS, 426, 3178
Majumdar S., Bharadwaj S., Datta K. K., Choudhury T. R., 2011, MNRAS, 413, 1409
Mao X.-C., 2012, ApJ, 744, 29
Mao Y., Shapiro P. R., Mellema G., Iliev I. T., Koda J., Ahn K., 2012, MNRAS, 422, 926
Mao Y., Tegmark M., McQuinn M., Zaldarriaga M., Zahn O., 2008, Phys. Rev. D, 78, 023529
Mapelli M., Ferrara A., Pierpaoli E., 2006, MNRAS, 369, 1719
Matejek M. S., Morales M. F., 2009, ArXiv:0911.3942
Mather J. C. et al., 1990, ApJ, 354, L37
Matsumoto T. et al., 2000, in Lecture Notes in Physics, Berlin Springer Verlag, Vol. 548, ISO Survey of a Dusty Universe, Lemke D., Stickel M., Wilke K., eds., p. 96
Matsumoto T. et al., 2011, ApJ, 742, 124
McKinley B. et al., 2013, AJ, 145, 23
McQuinn M., Furlanetto S. R., Hernquist L., Zahn O., Zaldarriaga M., 2005, ApJ, 630, 643
McQuinn M., Hernquist L., Zaldarriaga M., Dutta S., 2007a, MNRAS, 381, 75
McQuinn M., Lidz A., Zahn O., Dutta S., Hernquist L., Zaldarriaga M., 2007b, MNRAS, 377, 1043
McQuinn M., O'Leary R. M., 2012, ApJ, 760, 3

McQuinn M., Zahn O., Zaldarriaga M., Hernquist L., Furlanetto S. R., 2006, ApJ, 653, 815
Meiksin A., 2011, MNRAS, 417, 1480
Mellema G., Iliev I. T., Pen U.-L., Shapiro P. R., 2006, MNRAS, 372, 679
Mesinger A., 2010, MNRAS, 407, 1328
Mesinger A., Furlanetto S., Cen R., 2011, MNRAS, 411, 955
Mesinger A., McQuinn M., Spergel D. N., 2012, MNRAS, 422, 1403
Morales M. F., Hewitt J., 2004, ApJ, 615, 7
Mortlock D. J. et al., 2011, Nature, 474, 616
Nusser A., 2005, MNRAS, 364, 743
Oesch P. A. et al., 2013, ArXiv:1301.6162
Offringa A. R., 2012, PhD thesis, Kapteyn Astronomical Institute, University of Groningen
Offringa A. R., de Bruyn A. G., Biehl M., Zaroubi S., Bernardi G., Pandey V. N., 2010, MNRAS, 405, 155
Offringa A. R. et al., 2013, A&A, 549, A11
Ord S. M. et al., 2010, PASP, 122, 1353
Ostriker J. P., Vishniac E. T., 1986, ApJ, 306, L51
Ouchi M. et al., 2010, ApJ, 723, 869
Paciga G. et al., 2013, ArXiv e-prints
Paciga G. et al., 2011, MNRAS, 413, 1174
Padmanabhan N., Finkbeiner D. P., 2005, Phys. Rev. D, 72, 023508
Pan T., Barkana R., 2012, ArXiv:1209.5751
Pandolfi S. et al., 2010, Phys. Rev. D, 82, 123527
Parsons A., Pober J., McQuinn M., Jacobs D., Aguirre J., 2012a, ApJ, 753, 81
Parsons A. R., Backer D. C., 2009, AJ, 138, 219
Parsons A. R. et al., 2010, AJ, 139, 1468
Parsons A. R., Pober J. C., Aguirre J. E., Carilli C. L., Jacobs D. C., Moore D. F., 2012b, ApJ, 756, 165
Pearson R., 2002, EDN, www.edn.com
Pen U.-L., Chang T.-C., Hirata C. M., Peterson J. B., Roy J., Gupta Y., Odegova J., Sigurdson K., 2009, MNRAS, 399, 181
Petrovic N., Oh S. P., 2011, MNRAS, 413, 2103
Pindor B., Wyithe J. S. B., Mitchell D. A., Ord S. M., Wayth R. B., Greenhill L. J., 2011, PASA, 28, 46
Pober J. C. et al., 2013, ArXiv:1301.7099
Prasad J., Chengalur J., 2012, Experimental Astronomy, 33, 157
Prasad P., Wijnholds S. J., 2012, ArXiv:1205.3056
Pritchard J. R., Furlanetto S. R., 2007, MNRAS, 376, 1680
Pritchard J. R., Loeb A., 2008, Phys. Rev. D, 78, 103511
Pritchard J. R., Loeb A., 2010, Phys. Rev. D, 82, 023006
Pritchard J. R., Loeb A., 2012, Reports on Progress in Physics, 75, 086901
Ratcliffe J. A., 1956, Reports on Progress in Physics, 19, 188
Ricotti M., Ostriker J. P., Mack K. J., 2008, ApJ, 680, 829
Rogers A. E. E., Bowman J. D., 2008, AJ, 136, 641
Roy J., Gupta Y., Pen U.-L., Peterson J. B., Kudale S., Kodilkar J., 2010, Experimental Astronomy, 28, 25
Salvaterra R., Ciardi B., Ferrara A., Baccigalupi C., 2005, MNRAS, 360, 1063
Salvaterra R., Ferrara A., 2003, MNRAS, 339, 973
Salvaterra R., Ferrara A., 2006, MNRAS, 367, L11
Santos M. G., Amblard A., Pritchard J., Trac H., Cen R., Cooray A., 2008, ApJ, 689, 1
Santos M. G., Cooray A., 2006, Phys. Rev. D, 74, 083517
Santos M. G., Cooray A., Haiman Z., Knox L., Ma C.-P., 2003, ApJ, 598, 756
Santos M. G., Cooray A., Knox L., 2005, ApJ, 625, 575
Santos M. G., Ferramacho L., Silva M. B., Amblard A., Cooray A., 2010, MNRAS, 406, 2421
Santos M. G., Silva M. B., Pritchard J. R., Cen R., Cooray A., 2011, A&A, 527, A93
Santos M. R., Bromm V., Kamionkowski M., 2002, MNRAS, 336, 1082
Schaffer K. K., et al., 2011, ApJ, 743, 90
Schmidt M., Schneider D. P., Gunn J. E., 1995, AJ, 110, 68
Semelin B., Combes F., Baek S., 2007, A&A, 474, 365
Shapiro P. R., Iliev I. T., Alvarez M. A., Scannapieco E., 2006, ApJ, 648, 922
Shapiro P. R. et al., 2012a, in American Institute of Physics Conference Series, Vol. 1480, American Institute of Physics Conference Series, Umemura M., Omukai K., eds., pp. 248–260
Shapiro P. R., Mao Y., Iliev I. T., Mellema G., Datta K. K., Ahn K., Koda J., 2012b, ArXiv e-prints
Shaver P. A., Windhorst R. A., Madau P., de Bruyn A. G., 1999, A&A, 345, 380
Shirokoff E. et al., 2011, ApJ, 736, 61
Slosar A., Cooray A., Silk J. I., 2007, MNRAS, 377, 168
Sun X. H., Reich W., 2009, A&A, 507, 1087
Sun X. H., Reich W., Waelkens A., Enßlin T. A., 2008, A&A, 477, 573
Sunyaev R. A., Zeldovich Y. B., 1970, Ap&SS, 7, 3
Tashiro H., Aghanim N., Langer M., Douspis M., Zaroubi S., 2008, MNRAS, 389, 469
Tashiro H., Aghanim N., Langer M., Douspis M., Zaroubi S., Jelić V., 2011, MNRAS, 414, 3424
Theuns T., Schaye J., Zaroubi S., Kim T., Tzanavaris P., Carswell B., 2002, ApJ, 567, L103
Thomas R. M. et al., 2009, MNRAS, 393, 32
Thompson A. R., Moran J. M., Swenson, Jr. G. W., 2001, Interferometry and Synthesis in Radio Astronomy, 2nd Edition

Thompson R. I., Eisenstein D., Fan X., Rieke M., Kennicutt R. C., 2007, ApJ, 657, 669
Tingay S. J. et al., 2013, PASA, 30, 7
Toma K., Sakamoto T., Mészáros P., 2011, ApJ, 731, 127
Tozzi P., Madau P., Meiksin A., Rees M. J., 2000, ApJ, 528, 597
Trac H. Y., Gnedin N. Y., 2011, Advanced Science Letters, 4, 228
Trott C. M., Wayth R. B., Tingay S. J., 2012, ApJ, 757, 101
Tseliakhovich D., Hirata C., 2010, Phys. Rev. D, 82, 083520
van Weeren R. J. et al., 2012, A&A, 543, A43
Visbal E., Barkana R., Fialkov A., Tseliakhovich D., Hirata C., 2012, Nature, 487, 70
Visbal E., Loeb A., 2010, J. Cosmology Astropart. Phys., 11, 16
Vishniac E. T., 1987, ApJ, 322, 597
Volonteri M., Gnedin N. Y., 2009, ApJ, 703, 2113
Vonlanthen P., Semelin B., Baek S., Revaz Y., 2011, A&A, 532, A97
Waelkens A., Jaffe T., Reinecke M., Kitaura F. S., Enßlin T. A., 2009, A&A, 495, 697
Wang X., Tegmark M., Santos M. G., Knox L., 2006, ApJ, 650, 529
Wiersma R. P. C. et al., 2012, ArXiv:1209.5727
Williams C. L. et al., 2012, ApJ, 755, 47
Willott C. J. et al., 2010, AJ, 139, 906
Wilman R. J. et al., 2008, MNRAS, 388, 1335
Wright E. L., Reese E. D., 2000, ApJ, 545, 43
Wyithe J. S. B., Loeb A., Barnes D. G., 2005, ApJ, 634, 715
Xu Y., Chen X., Fan Z., Trac H., Cen R., 2009, ApJ, 704, 1396
Xu Y., Ferrara A., Chen X., 2011, MNRAS, 410, 2025
Yatawatta S., 2010, ArXiv:1008.1892
Yatawatta S., 2011, ArXiv:1101.2830
Yatawatta S. et al., 2013, A&A, 550, A136
Yatawatta S., Zaroubi S., de Bruyn G., Koopmans L., Noordam J., 2008, ArXiv:0810.5751
Yu Q., 2005, ApJ, 623, 683
Yue B., Ferrara A., Salvaterra R., Chen X., 2013, MNRAS, 823
Zahn O., Lidz A., McQuinn M., Dutta S., Hernquist L., Zaldarriaga M., Furlanetto S. R., 2007, ApJ, 654, 12
Zahn O. et al., 2012, ApJ, 756, 65
Zahn O., Zaldarriaga M., Hernquist L., McQuinn M., 2005, ApJ, 630, 657
Zaldarriaga M., Furlanetto S. R., Hernquist L., 2004, ApJ, 608, 622
Zaroubi S. et al., 2012, MNRAS, 425, 2964
Zaroubi S., Thomas R. M., Sugiyama N., Silk J., 2007, MNRAS, 375, 1269
Zeldovich Y. B., Sunyaev R. A., 1969, Ap&SS, 4, 301
Zhang P., Pen U.-L., Trac H., 2004, MNRAS, 347, 1224